Characteristics of the Planetary Wave Packet Propagation During Boreal Winter as Revealed by Japanese Long-term Reanalysis Data

原田, やよい

Characteristics of the Planetary Wave Packet Propagation During Boreal Winter as Revealed by Japanese Long-term Reanalysis Data

HARADA Yayoi

Meteorological Research Institute, Tsukuba, Japan

January 2019

Contents

Abstract

In this study, three analyses on the characteristics of the planetary wave packet propagation during boreal winter are conducted by using the Japanses55-year reanalysis (JRA-55).

First, observational features of the winter 2013/2014 are investigated. This winter can be characterized by the continuous predominance of planetary waves of zonal wavenumber two (WN2) that did not cause major sudden stratospheric warming (SSW) events. It is found that the vertical component of the Eliassen-Palm flux of WN2 for the winter 2013/2014 is almost equal to the highest value of the winter 2008/2009. The longitudinal distribution of vertical components of Plumb wave activity flux for this winter shows marked downward propagation around 100°W and upward propagation around 60°E, both of which are the strongest of their type among the 56 winters since 1958/1959. The convergence of wave packets propagating from around 60°E contributes to the development and continuance of the quasi-barotropic Aleutian High, which is associated with the extension of negative extended refractive index (Ks) region. The extension of negative Ks region is related to the convergence or reflection of the wave packets emanating from tropospheric blocking highs developing in the North Pacific Ocean; the development and continuance of the quasi-barotropic Aleutian High is considered to be one of plausible reasons for the lack of major SSWs in the winter 2013/2014. In addition to these results, we revealed the significant contribution of smaller scale waves (with a zonal

wavenumber of three or more) to the structure of localized wave packet propagation in the stratosphere.

Second, time evolution and characteristic features of “wave amplification events” of upper-tropospheric WN2 during the boreal winter are investigated. We extracted strong WN2 amplification events that variance of meridional wind component at 250 hPa exceeds one standard deviation from all samples of 60 winters since 1958/1959, and further extracted four groups from these events based on the vertical component of Eliassen-Palm (EP) flux at 30 hPa for WN2 two days after a WN2 amplification peak in the upper troposphere. The results of our composite analysis show that, in the strong upward WN2 propagation group (SU_30EPFz), the remarkable development of the upper tropospheric ridge around Alaska and the negative surface temperature anomalies in North America, the quasi-stationary Rossby wave propagation along the sub-tropical jet that strengthen the ridge around Alaska, and La Niña-like conditions are statistically significant prior to the WN2 amplification peak. On the other hand, in the strong downward WN2 propagation group (SD_30EPFz), the development of the upper tropospheric ridge are observed over North Europe and the wide-ranged negative surface temperature anomalies from Europe to Central Asia are statistically significant prior to the WN2 amplification peak, but no significant relation to the tropical SST is found. As for the stratospheric circulation after the WN2 amplification peak in the upper troposphere, the polar night vortex splitting occurs in SU_30EPFz, while the development of the Aleutian high in SD_30EPFz is indicated.

Finally, Observational features of atmospheric fields during WN2 type major SSW

(MSSW) event that occurred in February 2018 (MSSW18) are analyzed by using a new three-dimensional wave activity flux. MSSW18 was characterized by a clear polar vortex split, continuance of easterlies with clear double peaks, clear planetary-wave propagation in the easterly region of the upper stratosphere and extraordinary upward propagation of WN2 planetary waves from the upper troposphere whose peak was comparable to that during an MSSW event that occurred in January 2009 (MSSW09), although MSSW18 showed relatively modest warming compared to those during MSSW09. Further analyses revealed that wave packets propagated upward simultaneously in both the Eastern and Western Hemispheres. Those observed in the Eastern Hemisphere converged strongly at the western edge of the Aleutian High and most of them did not propagate into the upper stratosphere. The wave packets observed in the Western Hemisphere locally propagated into the upper stratosphere over North America despite the fact that easterlies were predominant there in the mature stage of MSSW18. Furthermore, our results revealed that the regions and levels of wave-packet attenuation corresponded well to the area of weak eastward phase tilt or the quasi-barotropic condition of smaller-scale waves during MSSW18, whereas during MSSW09 the westward phase tilts of smaller-scale waves were clearly visible in the upper stratosphere.

1. Introduction

In the boreal winter stratosphere, zonal-mean zonal winds are generally westerly with maxima around 60°N and correspondently zonal-mean temperatures decrease towards the pole, which are referred to as the polar vortex. However, sometimes this situation is dramatically disrupted by upward propagation of planetary waves from the troposphere, leading to a rapid polar stratospheric warming and, on occasion, a reversal of zonal-mean winds. Such a phenomenon is referred to as a sudden stratospheric warming (SSW). The World Meteorological Organization (WMO) defines a "minor warming" as an identified polar warming of 25 K or more within a week at any stratosphere level; the classification is upgraded to a "major warming" if the zonal-mean zonal winds become easterlies north of 60°N at the 10-hPa level or below (WMO 1978, item 9.4, 35–36).

There are two types of major SSW (MSSW), i.e., displacement events in which the stratospheric polar vortex is displaced from the pole and split events in which the vortex splits into two or more vortices (Butler et al., 2017; Charlton & Polvani, 2007). In displacement events, planetary waves of zonal wavenumber one (WN1) plays a primary role, whereas in split events, the primary role is played by planetary waves of zonal wavenumber two (WN2). In most split events, WN1 also contributes to the SSW occurrence. Although it may be a rare case, there does exist a typical type of split events caused almost entirely by WN2, as reported by Krüger et al. (2005). In the present study, we term such an event a "WN2-type SSW event."

In the past several decades, some WN2-type major SSW events have been observed.

For example, Harada et al. (2010) analyzed a major SSW event of January 2009 and revealed that the event was characterized by an extraordinary predominance of WN2. Moreover, the total amount of the upward Eliassen-Palm (E-P) flux for WN2 in the winter of 2008/2009 was the strongest for the period since the winter of 1978/1979. They also compared observational features of this major SSW with those of major SSWs in February 1989 and December 1984; however, the period of their diagnoses was restricted after 1979 due to data limitations at that time. Because there were other winters with WN2 predominance and/or major WN2-type SSW occurrence prior to 1979, for example, in January 1963 (Finger & Teweles, 1964) and in the winter 1971/1972 (Labitzke, 1977, 1978), it is necessary to make use of a more homogeneous data set covering as long period as possible, thereby extending the analysis period.

In terms of the relationship between the SSW occurrence and tropospheric circulation, the importance of blocking phenomena in the troposphere has been pointed out by many authors (e.g., Labitzke, 1965; O'Neill & Taylor, 1979; Quiroz, 1986). Recently, it has been recognized that vortex splitting events are preceded by blocks in the Pacific Basin or in both the Atlantic and Pacific basins, whereas vortex displacement events are preceded by blocks over the Atlantic basin only (e.g., Mukougawa et al., 2005; Martius et al., 2009; Castanheira & Barriopedro, 2010; Harada et al., 2010; Nishii et al., 2011; Bancalá et al., 2012). In particular, Harada et al. (2010) analyzed the WN2-type MSSW09 and revealed that wave packets emanated from the upper-tropospheric ridge over Alaska played a crucial role in the initial development of MSSW09 using Plumb's WAF. This frequent development of

upper-tropospheric ridges is intimately associated with the persistence of a blocking system. However, it should be noted that most of strong blocks do not necessarily lead to SSWs; Martius et al. (2009) actually showed that only 52 blocks are followed by SSWs among 782 blocks during the boreal winters from 1957 to 2001.

On the other hand, the modulation of the SSW occurrence due to El Niño–Southern Oscillation (ENSO) has been pointed out by several authors but this issue is still controversial: It has been reported that SSWs occurring during El Niño events are likely to be preceded by amplification of WN1, whereas La Niña SSWs are predominantly associated to WN2 amplification (e.g., Calvo et al., 2010; Harada et al., 2010; Taguchi & Hartmann, 2006; Barriopedro & Calvo, 2014). In addition, numerical experiments (e.g., Calvo et al., 2010; Taguchi & Hartmann, 2006) and observations (e.g., Labitzke & van Loon, 1999) have revealed a tendency for SSWs to occur preferentially during El Niño winters. However, some studies have pointed out that SSWs occur with approximately equal frequency during El Niño and La Niña winters (Butler & Polvani, 2011; Barriopedro & Calvo, 2014).

To date, the wave activity flux (WAF) based on Plumb (1985) has been used for the three-dimensional (3D) analysis of stationary planetary scale waves during MSSW events. However, the application of Plumb's WAF is restricted to the region of westerly basic flows because such application is confined to stationary Rossby waves. Recently, Kinoshita and Sato (2013a, 2013b) developed a new 3D WAF, namely 3D-flux-W that can accurately describe the magnitude and direction of wave-packet propagation using the primitive

equations. 3D-flux-W can be applied to both inertia-gravity waves and Rossby waves and can be used not only in the westerly basic flow but also in the easterly basic flow. During MSSW events, we often observe stratospheric zonal wind fields changing rapidly from westerlies to easterlies, and 3D-flux-W allows us to analyze wave packets even when easterlies are predominant.

So far, numerous studies focusing on the SSW and its relationships with tropospheric conditions such as ENSO have been conducted as mentioned above. However, various unclarified issues concerning to the WN2 predominance in the stratosphere have still remained. Therefore, we aim to reveal the details and plausible mechanisms of the planetary wave packet propagation related to the occurrence of MSSWs during boreal winters focusing on the cases of the predominance of WN2.

The thesis is composed of the three main parts: In the first part, we examine the features and plausible mechanisms of the continuous predominance of WN2, which did not cause major SSWs in the winter 2013/2014. In the second part, we perform composite analysis and clarify the time evolution and characteristic features of "wave amplification events" of upper-tropospheric WN2 during boreal winters. Finally, we analyze stratospheric and tropospheric fields during MSSW18 comparing with those in previous WN2-type MSSW events using 3D-flux-W as a new analysis tool.

2. Theoretical Background

2.1. The TEM equations

We briefly review the Transformed Eulerian Mean (TEM) primitive equations described in Andrews et al. (1987). Using the "log-pressure" coordinate $z \equiv -H \ln(p/p_s)$ and spherical coordinate in the horizontal, the primitive equations take the following form (Holton 1975):

$$\frac{Du}{Dt} - \left(f + \frac{u \tan \emptyset}{a}\right) v + \frac{\Phi_\lambda}{a \cos \phi} = \boldsymbol{X}, \quad (2.1.1)$$

$$\frac{Dv}{Dt} + \left(f + \frac{u \tan \emptyset}{a}\right) u + \frac{\Phi_\emptyset}{a} = \boldsymbol{Y}, \quad (2.1.2)$$

$$\Phi_z = H^{-1} R \theta e^{-\kappa z/H}, \ \kappa \equiv R/C_p \quad (2.1.3)$$

$$\frac{[u_\lambda + (v \cos \emptyset)_\emptyset]}{a \cos \emptyset} + \frac{(\rho_0 w)_z}{\rho_0} = 0, \quad (2.1.4)$$

$$\frac{D\theta}{Dt} = Q, \quad (2.1.5)$$

where ρ, a, λ, ϕ, u, v, w, θ, f, H, R, C_p and Q are density, radius of the earth, longitude, latitude, zonal wind, meridional wind, vertical wind, potential temperature, Coriolis parameter, scale height, gas constant, specific heat at constant pressure, and diabatic heating, respectively. X and Y are unspecified horizontal components of friction, or other non-conservative mechanical forcings, and Q is diabatic heating term.

Separating each variable into a zonal-mean part and a disturbance part, substituting into the primitive equations (2.1.1)-(2.1.5), and taking the zonal average, we obtain a set of

primitive equations for Eulerian-mean flow.

A residual mean circulation $\left(0, \overline{v}^*, \overline{w}^*\right)$ is defined as follows:

$$\overline{v}^* \equiv \overline{v} - \rho_0{}^{-1}\left(\frac{\rho_0 \overline{v'\theta'}}{\overline{\theta}_z}\right)_z , \qquad (2.1.6)$$

$$\overline{w}^* \equiv \overline{w} + (a\cos\emptyset)^{-1}\left(\frac{\cos\emptyset\,\overline{v'\theta'}}{\overline{\theta}_z}\right)_\emptyset , \qquad (2.1.7)$$

where over bar and prime mean zonal mean and the departure from the zonal mean, respectively. On substituting for $\left(\overline{v}\ , \overline{w}\ \right)$ in the zonal averaged primitive equations for Eulerian-mean flow as mentioned above, the following TEM set is obtained:

$$\overline{u}_t + \overline{v}^*[(a\cos\emptyset)^{-1}(\overline{u}\cos\emptyset)_\emptyset - f] + \overline{w}^*\overline{u}_z - \overline{\boldsymbol{X}}$$

$$= (\rho_0\cos\emptyset)^{-1}\nabla\cdot\boldsymbol{F}, \qquad (2.1.8)$$

$$\overline{u}(f + \overline{u}a^{-1}\tan\emptyset) + a^{-1}\overline{\Phi}_\phi = \boldsymbol{G}, \qquad (2.1.9)$$

$$\overline{\Phi}_z - H^{-1}R\overline{\theta}e^{-\frac{\kappa z}{H}} = 0, \qquad (2.1.10)$$

$$(a\cos\emptyset)^{-1}\left(\overline{v}^*\cos\emptyset\right)_\emptyset + \rho_0{}^{-1}\left(\rho_0\overline{w}^*\right)_z = 0, \qquad (2.1.11)$$

$$\overline{\theta}_t + a^{-1}\overline{v}^*\overline{\theta}_\emptyset + \overline{w}^*\overline{\theta}_z - \overline{Q} = -\rho_0{}^{-1}\left[\rho_0\left(\overline{v'\theta'}\frac{\overline{\theta}_\emptyset}{a\overline{\theta}_z} + \overline{w'\theta'}\right)\right]_z . \qquad (2.1.12)$$

The vector $\boldsymbol{F} \equiv \left(0, F^{(\emptyset)}, F^{(z)}\right)$ is known as the primitive version of Eliassen-Palm (EP) flux and is represented as follows:

$$F^{(\emptyset)} \equiv \rho_0 a\cos\emptyset\left(\overline{u}_z\overline{v'\theta'}/\overline{\theta}_z - \overline{v'u'}\right), \qquad (2.1.13)$$

$$F^{(z)} \equiv \rho_0 a\cos\emptyset\left\{[f - (a\cos\emptyset)^{-1}(\overline{u}\cos\emptyset)_\emptyset]\overline{v'\theta'}/\overline{\theta}_z - \overline{w'u'}\right\}, \qquad (2.1.14)$$

A prime denotes small perturbations to a zonal mean field. G represents all the terms that lead to a departure from gradient-wind balance between $\overline{u}$ and $\overline{\Phi}$.

In the zonal mean circulation (the meridional plane), the TEM primitive equations are suitable for diagnosing eddy forcing (e.g., Andrews et al., 1987; Andrews & Mclntyre, 1976). Vectors of the EP flux represent the direction of easterly angular momentum propagation associated with waves in the meridional plane, and the total eddy forcing of zonal mean zonal winds can be represented by the divergence (westerly acceleration) and convergence (westerly deceleration) of EP flux in the stratosphere. Moreover, the total forcing to the time tendency of the zonal mean zonal wind can be estimated by the sum of advection, Coriolis forcing, and EP flux divergence, approximately.

2.2. Plumb's wave activity flux

In this study, a wave activity flux (WAF) that indicates propagating packets of planetary waves in three-dimensional space is calculated following Plumb (1985). It is useful to analyze passages in three-dimensional space where planetary waves propagate from the troposphere to the stratosphere. From Plumb (1985), the definition of the Plumb's WAF *Fs* on the sphere is represented in log-pressure coordinates as follows:

$$F_s = p\cos\phi \begin{pmatrix} \frac{1}{2a^2\cos^2\phi}\left[\left(\frac{\partial\psi'}{\partial\lambda}\right)^2 - \psi'\frac{\partial^2\psi'}{\partial\lambda^2}\right] \\ \frac{1}{2a^2\cos\phi}\left[\frac{\partial\psi'}{\partial\lambda}\frac{\partial\psi'}{\partial\phi} - \psi'\frac{\partial^2\psi'}{\partial\lambda\partial\phi}\right] \\ \frac{2\Omega^2\sin^2\phi}{N^2 a\cos\phi}\left[\frac{\partial\psi'}{\partial\lambda}\frac{\partial\psi'}{\partial z} - \psi'\frac{\partial^2\psi'}{\partial\lambda\partial z}\right] \end{pmatrix} \qquad (2.2.1)$$

where p is normalized pressure (hPa)/1,000 hPa, and ϕ and λ are latitude and longitude, respectively. A prime denotes small perturbations to zonal mean fields. The stream function, Earth's rotation rate, radius of the Earth, and buoyancy frequency are denoted by ψ, Ω, a, and N, respectively. Three-day mean daily pressure level data from JRA-55 are used for the calculation of WAF.

2.3. Extended refractive index

In this study, the extended refractive index (Ks) for three-dimensional space (Karoly, 1983; Nishii & Nakamura, 2004) is used to assess the behavior of wave packets, which tend to be refracted toward high index values. A band of maximum Ks represents a localized waveguide of a wave packet if the band is associated with a westerly jet. Karoly's definition of Ks is expressed in log-pressure coordinates as follows:

$$Ks^2 = \frac{|\nabla_H Q|}{|U|} - \frac{f_0^2}{4N^2H_0^2}\left(1 - 4H_0N\frac{dN^{-1}}{dz} + 4H_0^2N\frac{d^2N^{-1}}{dz^2}\right) \qquad (2.3.1)$$

where $\boldsymbol{U} = (U, V)$ denotes a horizontal basic flow, f0 is the Coriolis parameter, N is buoyancy frequency, H_0 is scale height in a basic flow, Q signifies quasi-geostrophic potential vorticity of the basic flow, and ∇H is the horizontal gradient operator.

2.4. A new three-dimensional wave activity flux

We briefly describe a 3D-flux-W (Kinoshita and Sato 2013b) used in the final part of this study. It is based on the primitive equations and can accurately describe the magnitude and direction of wave-packet propagation. In addition, it can be applied to both inertia-gravity waves and Rossby waves and can be used not only in the westerly basic flow but also in the easterly basic flow. We also add the pseudo-momentum multiplied by the basic flow to the zonal component of 3D-flux-W (Harada et al. under revision). The pseudo-momentum is derived based on Aiki et al. (2015). 3D-flux-W is described as follows:

$$Fw11 = \rho_0\left(\overline{u'^2} - \bar{S}\right) + \overline{U}\,\overline{W} \quad (2.4.1)$$

$$Fw12 = \rho_0(\overline{u'v'}), \quad (2.4.2)$$

$$Fw13 = \rho_0(\overline{u'w'}) - f\frac{\overline{v'\Phi'_z}}{N^2}, \quad (2.4.3)$$

$\overline{W}$: pseudo momentum, $\overline{U}$: basic flow

$$\bar{S} \equiv \frac{1}{2}\left(\overline{u'^2} + \overline{v'^2} - \frac{\overline{\Phi'_z}}{N^2}\right) \quad (2.4.5)$$

In addition, we apply an extended Hilbert transform based on Sato et al. (2013) to the perturbation field to eliminate its phase dependency. An extended Hilbert transform $H[a(\boldsymbol{x}, t)]$ of a particular fluctuation field $a(\boldsymbol{x}, t)$ is defined as an arbitrary fluctuation field composed of Fourier components of $a(\boldsymbol{x}, t)$ whose phases are shifted by $-\pi/2$ radians:

$$a(\boldsymbol{x},t) = \sum_{\boldsymbol{k},\omega} \sin\left(\boldsymbol{k}\cdot\boldsymbol{x} - \omega t + \varphi_{\boldsymbol{k},\omega}\right), \quad (2.4.6)$$

$$H[a(\boldsymbol{x},t)] = -\sum_{\boldsymbol{k},\omega} \cos\left(\boldsymbol{k}\cdot\boldsymbol{x} - \omega t + \varphi_{\boldsymbol{k},\omega}\right), (2.4.7)$$

where $k \equiv (k,l,m)$ is a wavenumber vector; *k, l, m* are zonal, meridional, and vertical wavenumbers, respectively; and $\varphi_{\boldsymbol{k},\omega}$ is an arbitrary phase. An analytic representation of the real function $a(\boldsymbol{x}, t)$ is defined as a complex function $A(\boldsymbol{x},t)\{\equiv a(\boldsymbol{x},t) + iH[a(\boldsymbol{x},t)]\}$. The envelope function $A_{env}(\boldsymbol{x}, t)$ of $a(\boldsymbol{x}, t)$ is obtained by using $A(\boldsymbol{x}, t)$:

$$\frac{1}{2}A_{env}(\boldsymbol{x}, t)^2 = \quad \frac{1}{2}A(\boldsymbol{x},t)\,A*(\boldsymbol{x},t). \quad (2.4.8)$$

The derivation is given in detail as the follows. The zonal-mean field of the three-day mean daily pressure level from JRA-55 is used as the basic field for calculating 3D-flux-W, and perturbations are defined as deviations of the six-hourly instantaneous analysis field from this basic field.

3. Data and Analysis Methods

3.1 Long-term reanalysis data

JRA-55 covers the 55 years from 1958 to 2012 as of their originally produced time in 2013 and is the first reanalysis to apply four-dimensional variational analysis to this period (Kobayashi et al., 2015). As of December 2009, the forecast model used for JRA-55 is based on the TL319 spectral resolution version of the Japan Meteorological Agency (JMA) global spectral model. The TL319 spectral resolution is equivalent to a horizontal grid size of around 55 km. The model has 60 layers (from 1 to 1.2 km vertical grid spacing in the lower stratosphere), with the top level at 0.1 hPa. In addition, because JRA-55 has operated on a near-real-time basis, its products are available for the period after 2013. Therefore, its products are available for the period after 2013, which covers 60 boreal winters (from 1958/1959 to 2017/2018).

We also use the Centennial in situ Observation-Based Estimates of variability of sea surface temperature (SST) and marine meteorological variables (COBE) dataset analyzed globally on the basis of an optimum interpolation technique with longitude and latitude resolutions of 1 x 1 degree (Ishii et al. 2005).

3.2 Lanczos filtering

We briefly describe a Lanczos filter (Duchon, 1979). Digital filtering involves transforming an input data sequence x_t, where t is time, into an output data sequence y_t using linear relationship

$$y_t = a_0 + \sum_{n=1}^{\infty} w_k x_{t-k}, \qquad (3.2.1)$$

in which the w_k are suitably chosen weights. For example, weights for high pass filter are represented as follows:

$$w_k = \frac{\sin(2\pi f_c k)}{\pi k} \frac{\sin(\pi k/n)}{\pi k/n}, k = -n, \cdots, 0, \cdots, n, \qquad (3.2.2)$$

where f_c and $2n+1$ are cutoff frequency and sample size for filtering, respectively. Weights for Low pass filter can be obtained by subtracting those for high pass filter from one. Moreover, we can obtain weights for band pass filter using weights for two low pass filters with different cutoff frequencies.

The filtered atmospheric variables, such as zonal wind, meridional wind, temperature, and geopotential height, are used for the calculation of Plumb's WAF, 3D-flux-W as described above. Spatial low-pass filters with eight kinds of settings are used for the calculation of Plumb's WAF: WN<=2, WN<=3,..., and WN<=9.

In the case of 3D-flux-W, we applied spatial band pass filter to the six-hourly perturbation components of the atmospheric variables, and extracted each WN component from WN=1 to WN=20, which are used in an extended Hilbert transform prior to the calculation of 3D-flux-W.

In addition, we also apply bandpass (WN=1 and WN=2) and high-pass filters (WN>=3 and WN>=5) to the meridional wind component and visualize the vertical phase tilts of various scale waves

4. Extraordinary Features of the Planetary Wave Propagation During the Boreal Winter 2013/2014

4.1 Overall features of the boreal winter 2013/2014

The boreal winter 2013/2014 can be characterized by frequent upward propagation of planetary wave packets from the troposphere to the stratosphere and by the continuous activity of planetary waves of zonal wavenumber two (WN2) in the stratosphere throughout almost the entire season. However, no major sudden stratospheric warmings (SSWs) developed during this winter, although a minor SSW did occur in early February 2014. On the other hand, in the troposphere, persistent negative height anomalies extended widely over North America–North Atlantic high latitudes at the 500 hPa level, and average temperatures in North America were the second coldest of the period 1960–2014 (Yu & Zhang, 2015).

4.2 Features of planetary wave propagation

Figure 4-1 shows the overall features of the winter 2013/2014, that is, the winter (December through February) averaged geopotential height distribution at 10 hPa in the Northern Hemisphere in Figure 4-1a, along with time-height sections of zonal mean temperatures averaged over 75°–90°N (Figure 4-1b) and zonal winds at 60°N for the period from November 2013 to March 2014 (Figure 4-1c). The predominance of WN2 in the winter 2013/2014 can be recognized in the geopotential height distribution of the stratosphere (Figure 4-1a). During early to middle December 2013, stratospheric

temperatures to the north of 75°N became colder (Figure 4-1b) and westerlies at 60°N became stronger (Figure 4-1c); this was accompanied by the strengthening of the polar night vortex. At the end of the month, temperatures began to rise gradually in association with an increase in the upward propagation of WN2, leading to a minor SSW in early February 2014 (although westerlies weakened during the minor SSW and easterlies appeared only around 3 hPa and above).

We next investigate the inter-annual variability of the vertical propagation of planetary waves using JRA-55. Line plots in Figure 4-2 show the time series of the vertical component of the EP flux (EPFz) for WN1, WN2, and all wavenumbers averaged over 30°–90°N at 100 hPa during the 56 boreal winters since 1958/1959. The EPFz of WN2 for the winter 2013/2014 is almost equal to the highest value of EPFz in the winter 2008/2009 when, in contrast to the winter 2013/2014, a major SSW occurred (blue line in Figure 4-2). In addition, the ratio of the WN2 contribution to the sum of WN1 and WN2 for the winter 2013/2014 reaches almost 0.8 (in Figure 4-2b), revealing the predominance of WN2 in the winter 2013/2014. We also identify six winters during the analysis period (1961/1962, 1962/1963, 1971/1972, 1984/1985, 1988/1989, and 2008/2009) based on a critical ratio of 0.6 for the WN2 contribution to the sum of WN1 and WN2. These winters are defined as "WN2 winters" and are compared with the winter 2013/2014 in this study. WN2 winters are also classified into two categories as pink and light blue stars shown in Figure 4-2a. One is that a major SSW occurred during the winter (WN2_MSSW winters), and the other is that no major SSW occurred during the winter (WN2_noMSSW winters). In general, total

EPFz (gray bars in Figure 4-2a) in WN2_MSSW winters tend to be more than those in WN2_noMSSW winters. However, note that EPFz in the winter 2013/2014 exceeds those in the winter 1988/1989. This indicates that the occurrence of a major SSW cannot be judged only by total EPFz from the troposphere to the stratosphere, although it is one of the important indicators. It is noted that the winter 1978/1979 is not included in the WN2 winters. The winter has relatively low ratio of WN2 to the sum of WN1 and WN2 in spite of the occurrence of WN2-type major SSW in February 1979, because a WN1-type minor SSW occurred in the second half of January 1979 and the predominance of WN2 is not clearly observed throughout the season (not shown).

Figure 4-3 plots the time evolution of EPFz for each wavenumber (lines) and all wavenumbers (gray shadings) averaged over 30°–90°N at 100 hPa for WN2 winters. The EPFz of WN2 in the winter 2013/2014 clearly shows frequent and continuous upward propagation of WN2 from the troposphere to the stratosphere throughout the winter (blue lines represent the vertical propagation of WN2). Compared with the other WN2 winters, the EPFz in mid-January of the winter 2008/2009 is extraordinarily strong (Figure 4-3b) and its peak has the highest value among the WN2 winters; peak values of the EPFz of WN2 in the other WN2 winters are not very strong compared with the winter 2008/2009. Although these WN2 peaks are present around 1.5×10^5 kg s^{-2}, the sharp peaks of total EPFz (gray shadings) reach almost 3.0×10^5 kg^2 s^{-2} for the major SSW cases in mid-February 1989 (Figure 4-3c) and mid-January 1963 (Figure 4-3f). In the case of mid-February 1989, both EPFz of WN1 and WN3 contribute to increase the total EPFz; on

the other hand, in the case of mid-January 1963, contribution of EPFz of WN3 surpasses that of WN1. From this point of view, the case of mid-January 2009 is quite singular because the total EPFz is larger than EPFz of WN2 without the contribution of EPFz of WN1 nor WN3. In the major SSW case of the second half of December 1984 (Figure 4-3d), the total EPFz is continuously observed around 2.0×10^5 kg s^{-2} for more than 10 days.

On the other hand, neither extremely strong upward propagation of total EPFz with a sharp peak nor continuous upward propagation is seen for the winters 2013/2014, 1971/1972, and 1961/1962, which had no major SSW cases (Figures 4-3a, 4-3e, and 4-3g). These results imply that smaller scale waves with wavenumbers larger than two contribute to the occurrence of WN2-type major SSWs in some cases.

Harada et al. (2010) showed that localized upward propagation of wave packets corresponding to the development of the upper tropospheric ridge occurred over Alaska in the case of the major SSW in January 2009. They also discussed the importance of the localized wave packets and smaller scale waves. Focusing on the longitudinal distribution, we compare the time evolution of the vertical propagations of wave packets during WN2 winters. Figure 4-4 illustrates longitude-time cross sections of vertical components of Plumb wave activity flux (WAFz) for each WN2 winter. As shown in Figure 7 of Harada et al. (2010), extraordinarily strong and localized upward propagation in the region east of 180° is seen in mid-January 2009 (Figure 4-4b), and a similar feature can be seen in the second half of January 1963 (Figure 4-4f). Moreover, in the cases of the winters 1984/1985 and 1988/1989, upward propagation is also seen in the same longitudinal band prior to the

major SSWs. We also compare the longitudinal distribution of the winter mean vertical component of the wave activity flux (WAFz) averaged over 30°–90°N at 100 hPa (Figure 4-5a). The WAFz values for WN2 winters in which major SSWs commonly occurred exceed the climatological means of WAFz (black dotted line in Figure 4-5a) in the region from 180° to 60°W.

In contrast, in middle to late January of the winter 2013/2014 (Figure 4-4a), although localized upward propagation is still seen around 150°W, strong downward propagation is observed just to the east of this point. Moreover, in February, the downward propagation was extended to the region from 180° to 60°W, which is significantly stronger than that of the other WN2 winters. In addition, the downward propagation of the wave packets is continuously seen throughout the winter, which is similar to the winter 1971/1972 (Figure 4-4e) during which no major SSW occurred. Comparing the longitudinal distributions of the winter mean WAFz values averaged over 30°–90°N at 100 hPa (Figure 4-5a), the WAFz for the winter 2013/2014 (thick blue line in Figure 4-5a) is characterized by remarkable downward propagation around 100°W and upward propagation around 60°E, both of which are the strongest of their type among the 56 winters since 1958/1959. Similar features are also observed in WAFz of the winter 1971/1972 (light blue line in Figures 4-5a), although they are modest compared with those of the winter 2013/2014.

We also find that the winter 2013/2014 upward wave packet propagation around 60°E significantly shifts southward compared with the other winters (Figure 4-5b). Such events were clearly observed at the end of December 2013 and in the first half of February 2014

(not shown). Potential effects of the southward shift will be discussed later. It is also noted that the remarkable downward propagation around 100°W in the winter 2013/2014 does not shift from the climatological location (Figure 4-5c).

We further conduct comparisons between the longitudinal distributions of WAFz for the WN2 winters and those for the WN1 winters (Figure 4-6). The WN2 winters are classified into WN2_MSSW winters (red line in Figure 4-6) and WN2_noMSSW winters (blue line in Figure 4-6) as in Figure 4-2. The gray shading and the black dotted line represent, respectively, the ranges of the standard deviations and averages of WAFz for the WN1 winters. There are evident differences in WAFz distribution between the WN2_MSSW winters and WN2_noMSSW winters; moreover, they also differ from the WN1 winters. Upward propagation of wave packets for WN2_MSSW (red line in Figure 4-6) tends to be larger than the average of those for WN1 winters at longitudes from the east of 120°E to the Western Hemisphere; in particular, it exceeds the standard deviation range of WN1 winters around 165°W and 100°W. On the other hand, it tends to be lower than the averages of those for the WN1 winters in the region from 0° to 60°E. Interestingly, the WAFz for WN2_noMSSW (blue line in Figure 4-6) shows features that are the opposite of those for WN2_MSSW; that is, upward propagation largely exceeds the standard deviation range of the WAFz for WN1 winters from 30°E to 60°E, whereas downward propagation is much larger than that for the WN1 winters from 150°W to 90°W. In addition, as shown in Figure 4-5a, upward wave packet propagation around 150°W in the winter 2013/2014 largely exceeds the climatological average. The winter 2013/2014 is similar to the WN2_MSSW

winters (Figure 4-6) in this regard, despite a lack of major SSW occurrence in the winter 2013/2014.

4.3 Influence of upward wave packet propagation on stratospheric circulation

As described in the previous section, the upward wave packet propagation around 60°E in the winter 2013/2014 is the strongest among the 56 winters since 1958/1959. In this section, we investigate the effect of the upward wave packet propagation on stratospheric circulation.

Figure 4-7 illustrates longitude-height cross sections of geopotential height deviations from the zonal mean values, along with Plumb WAF vectors averaged over 45°–65°N based on successive 3 day means. At the end of December 2013 (Figures 4-7a), the upward propagating portion of the wave packets emanating from the upper tropospheric ridge around 60°E converges at the western edge of the Aleutian High around 150°E (Figure 4-7b), which seems to cause the development of the Aleutian High. Although such upward propagation ceased at the beginning of January (Figure 4-7c), the upward propagation of wave packets strengthens again and converges at the western edge of the Aleutian High, leading to the evolution of its quasi-barotropic structure (Figures 4-7d – 4-7f). Such convergence is often observed not only in early January 2014 but also, repeatedly, in the middle and late of the month (not shown), which seems to contribute to the development and continuance of the quasi-barotropic Aleutian High. It should be noted that the development of the Aleutian High in early January 2014 occurred under the circumstance

of no clear propagation of WN1 from the troposphere (Figure 4-3a) and the change to the quasi-barotropic structure is important for the downward propagation around 100°W, as shown later.

The localized wave packet convergence directly causes the deceleration of the westerly winds in the corresponding region. Figure 4-8a shows the longitudinal distributions of 31 day mean zonal winds averaged over 45°–65°N at 5 hPa, the level of the greatest wind deceleration. Persistent zonal wind decelerations centered at around 180° are evident from the end of December 2013 to mid-January 2014 and are accompanied by the development of the Aleutian High. Moreover, we compare the tendencies of lower frequency (or slowly varying) zonal winds from late December 2013 to mid-January 2014 with those in the other winters (Figure 4-8b). Figure 4-8b plots the tendencies of 31-day mean zonal winds during the period from late December to mid-January for each winter since the winter 1958/1959. The zonal wind deceleration in the winter 2013/2014 is found to be remarkable in the region corresponding to the Aleutian High. We also investigate the strength of the Aleutian High using the maximum values of 5 hPa geopotential height deviations from its zonal mean as an indicator. In this regard, we find that the Aleutian High in mid-January 2014 is one of the strongest since the winter 1958/1959 (not shown). Hence, it is considered that the development of the quasi-barotropic Aleutian High during the period from late December 2013 to mid-January 2014 was extraordinary.

Here the influence of the extraordinary development of the quasi-barotropic Aleutian High on wave packet propagation is examined. We have utilized Plumb WAF for depicting

wave packet propagation, in which zonal mean field is defined as a basic field. However, in actual atmospheric field, wave packets contain various scale waves, not only planetary scale waves but also smaller scale waves, even in the stratosphere as shown in our results. Because such smaller scale waves feel a zonally varying field due to planetary waves equivalently as a zonal uniform field, we consider properties of wave packet propagation in a zonally varying basic field. Figures 4-9d – 4-9f illustrate Ks for the three 31 day mean fields selected in the winter 2013/2014, along with the climatological mean field in Figures 4-9a – 4-9c. This figure shows that a negative Ks region, which prohibits Rossby wave penetration, continuously exists around 180° in association with the extension of the quasi-barotropic Aleutian High. The negative Ks region becomes broader than the climatological condition (Figures 4-9a – 4-9c). It can be said that the remarkable zonal wind deceleration accompanied by the development of the Aleutian High contributes to the further convergence of the wave packets propagating to the west of the Aleutian High and to the continuation of the quasi-barotropic Aleutian High itself. In addition to this, the extraordinary development of the quasi-barotropic Aleutian High and the related negative Ks region seems to have a further important influence on the wave packet propagation in the stratosphere. Extension of the negative Ks region associated with the extraordinary development of the quasi-barotropic Aleutian High does not allow wave packets to propagate upward from the region around the date line (Figures 4-9c and 4-9f). Actually, from late-January 2014 to mid-February 2014, tropospheric blocking highs developed frequently in the North Pacific Ocean but the wave packets emanating from those blocking

highs converged or reflected in the lower edge of the negative Ks region (not shown).

We can also note the influence of the smaller scale waves (relative to planetary waves) for the case in which the wave packet propagation is clearly localized around this region. We present a typical example in Figure 4-10, where Figure 4-10a depicts the wave packet propagation observed during 23–25 January 2014. In the lower stratosphere, both upward propagation to the west of the Aleutian High and downward propagation to the east are clearly observed. However, the vertical phase tilts of WN1 and WN2 present as almost barotropic (Figures 4-10b and 4-10c) and so are not able to explain the vertical wave propagation feature. On the other hand, westward and eastward phase tilts of zonal wavenumbers three or more are very clear on both sides of the Aleutian High, corresponding to upward and downward wave packet propagation, respectively (Figure 4-10d). Similar features repeatedly appeared during the winter 2013/2014. In addition, similar examples were observed during 23–25 February 1972, 5–7 February 1962, etc., in the other WN2 winters with no major SSWs (not shown).

4.4 Discussion of the importance of longitudinal distribution of wave packet propagation

We have examined the features and plausible mechanisms of the continuous predominance of WN2, which did not cause major SSWs in the winter 2013/2014, and found that the upward propagation brings about remarkable zonal wind deceleration accompanied by the extraordinary development of the quasi-barotropic Aleutian High, to

which the wave packet convergence to the west contributes. The wave packet convergence occurred continuously during the winter, leading to the further development and continuance of the quasi-barotropic Aleutian High. The extension of the negative Ks region associated with the extraordinary development of the quasi-barotropic Aleutian High prevents wave packets from propagating upward in the region around the date line. Hence, it is considered that the extraordinary development and continuance of the Aleutian High with quasi-barotropic structure prevent the occurrence of a major SSW. In fact, the development of the quasi-barotropic Aleutian High is also seen in January 1972 (see Figure 4 in Labitzke, 1978), although they do not mention the Aleutian High, only the development of WN2 in the troposphere and the stratosphere. These results strongly indicate the importance of longitudinal distribution of wave packet propagation containing WN2 from the troposphere to the stratosphere for considering the occurrence of a WN2-type major SSW.

In addition, the upward wave packet propagation around 60°E is found to be significantly shifted southward as compared with the other winters. Mitchell et al. (2013) and Davini et al. (2014) showed that SSW events are associated with increasing high-latitude blocking. Colucci and Kelleher (2015) showed that the tropospheric blocking events over the Northern Hemisphere that led to SSWs were associated with a significantly northward shifted distribution of eddy heat fluxes, and hence EPFz, in the upper troposphere near the block onset time (as compared with those in blocking events not leading to SSWs). They also revealed that the heat fluxes in the SSW-blocking composites

were concentrated inside the stratospheric polar vortex. As upward planetary wave propagation is closely related to heat fluxes, it can be assumed that such southward shifting of the wave packet propagation is one of the reasons for the lack of major SSW occurrence in the winter 2013/2014. However, the peak latitudes of the winters 1961/1962 and 1971/1972, which are WN2_noMSSW winters, do not shift southward. We need further investigation on this issue.

Furthermore, we have shown the coincidence of the propagation features of WAF and the vertical phase tilts of smaller scale waves (with a zonal wavenumber of three or more) in the stratosphere. Here we quantitatively discuss the contribution of smaller scale waves to the structure of wave packet propagation. Figure 4-11 plots the longitudinal distribution of WAFz for various zonal number ranges for three pressure levels. These are calculated using the 3-day mean field and averaged for the winter 2013/2014. At the 30-hPa level, the longitudinal features of the WAFz in the Western Hemisphere can be represented only by planetary wave components, that is, in the case considering only the components of zonal wavenumber two or less, whereas the contributions of larger zonal wavenumber components must be taken into account to reproduce the longitudinal features of the WAFz at 100 and 50 hPa: The downward propagation around 110°W (over northern Canada) is estimated to be only one third of the value obtained when using all zonal wavenumbers. When including larger zonal wavenumbers (in other words, smaller scale waves), the presentation of localized wave packet propagation becomes close to that found when using all zonal wavenumbers. Furthermore, similar situations are found in the other WN2 winters

(not shown). Therefore, we can conclude that it is important to consider smaller scale waves for the presentation of the localized wave packet propagation, not only in the troposphere but also in the stratosphere. That is to say, we need to analyze three-dimensional wave packet propagation to fully understand the mechanism of major SSW.

In this analysis, we have focused on the influence of the southward shifted wave packet propagation from the upper troposphere to the stratosphere, but we have not described why extraordinary WN2 propagation from the troposphere occurred. Barriopedro & Calvo (2014) revealed that the Pacific blocking frequency is significantly increased before La Niña SSWs. Using identical numerical experiments, Taguchi & Hartmann (2006) showed that WN2 events occur more frequently during the cold phase of ENSO, that is, in La Niña-like conditions. These studies indicate that the North Pacific blockings during La Niña periods tend to excite WN2 in the upper troposphere and are closely related to the WN2-type SSW. The tropical SST condition in the winter 2013/2014 seems to be a La Niña-like condition, and it is both similar to other WN2 winters and consistent with previous studies (not shown). Furthermore, it is not also clear why wave packets propagated significantly upward from around 60°E. Hence, further studies are required to clarify the dynamical relationship between the blocking activity in the North Pacific basin, the La Niña-like condition in the equatorial Pacific Ocean, and extraordinary WN2 propagation from the troposphere.

5. Time Evolution of Wave Amplification Events of the Upper-tropospheric Zonal Wavenumber Two and Its Influence on the Stratospheric Circulation During the Boreal Winter

5.1 Defining “wave amplification events” and composite analysis

Here we perform composite analysis and clarify the time evolution and characteristic features of “wave amplification events” of upper-tropospheric WN2 during the boreal winter using JRA-55.

First, we extract WN2 components from the daily-mean meridional wind field at 250 hPa ($250V_{WN2}$) and calculate five-day summation of variance of $250V_{WN2}$ regional averaged over the northern extra-tropical region (30°–90°N, 0°–360°E), which we refer as $250VVAR_{WN2}$. We then calculate normalized $250VVAR_{WN2}$ anomalies and extract specific events larger than one standard deviation (SD) cases from all samples of 60 winters since 1958/1959, which we refer to as WN2 amplification events in the upper troposphere (WN2AUT).

Next, we calculate five-day summation of daily-mean EPFz of WN1, WN2 at 5, 10, 30 and 100 ($EPFz_{WN1}$, $EPFz_{WN2}$, and $EPFz_{ALLWN}$). We also calculate $250VVAR_{WN1}$, $250VVAR_{ALLWN}$ and compare lag correlations between 250VVAR and EPFz at various levels with various time lags (Table 5-1). Because we find that the correlation between $250VVAR_{WN2}$ and two days after $30EPFz_{WN2}$ is the highest in the stratosphere higher than 100 hPa. Therefore, we define $30EPFz_{WN2}$ as the reference value of WN2

propagation in the lower stratosphere. We also find that 250VVAR_$_{WN2}$ has stronger correlation with EPFz_$_{WN2}$ in the stratosphere compared to those for WN1 and all wavenumbers. This result indicates the effectiveness to investigate the relationships between WN2AUT events and WN2 propagation in the stratosphere.

For composite analysis, we further classify WN2AUT events into the groups followed by whether WN2 propagates upward or downward in the lower stratosphere using two days lagged 30EPFz_$_{WN2}$. Note that if the extracted days are within 25 days, we consider those are the same event and we finally select one single peak day of 250VVAR_$_{WN2}$ from one event. Consequently, we can extract four groups from these events as follows (see also Table 5-2 and Figure 5-1):

- SU_30EPFz: Strong upward WN2 propagation events (normalized 30EPFz_$_{WN2}$ anomaly > 2.8 SD) observed in the lower stratosphere two days after the peaks of WN2AUT (normalized 250VVAR_$_{WN2}$ anomaly > 1.0 SD).
- WU_30EPFz: Moderate or weak upward WN2 propagation events (normalized 30EPFz_$_{WN2}$ anomaly <= 1.0 SD) observed in the lower stratosphere two days after the peaks of strong WN2AUT (normalized 250VVAR_$_{WN2}$ anomaly > 2.5 SD).
- WD_30EPFz: Moderate or weak downward WN2 propagation events (normalized 30EPFz_$_{WN2}$ anomaly are between -0.83 SD and -0.35 SD) observed in the lower stratosphere two days after the peaks of strong WN2AUT (normalized 250VVAR_$_{WN2}$ anomaly > 2.0 SD).

- SD_30EPFz: Strong downward WN2 propagation events (normalized $30EPFz_{WN2}$ anomaly < -0.87 SD) observed in the lower stratosphere two days after the peaks of WN2AUT (normalized $250VVAR_{WN2}$ anomaly > 1.0 SD).

Statistical significance is calculated using a Student's t test. The 90% and 95% confidence levels are used to indicate statistically significance values.

5.2 Surface conditions prior to the WN2AUT peak

We investigated surface conditions prior to the occurrence of WN2AUT peak, including SST, surface temperature and sea level pressure. Figure 5-2 shows lag composite maps of seven-day-mean SST anomalies during the periods 23–17 and 10–4 days before the WN2AUT peak for the four groups as described in Section 5.1. In the eastern part of the extratropical North Pacific, positive SST anomalies around 150°W are statistically significant 10–4 days before the WN2AUT peak (right panels of Figure 5-2) except WD_30EPFz (Figure 5-2f). However, the positive anomalies are weak and not significant 23–17 days before the WN2AUT peak (left panels of Figure 2) in SU_30EPFz, WU_30EPFz and SD_30EPFz (Figures 5-2a, 2c and 5-2g). In fact, these anomalies were strengthened simultaneously with the development of surface low pressure systems in the region (not shown). Therefore, it might be the results of the forcing from the atmosphere to the ocean. In addition, in WD_30EPFz, the positive SST anomalies more than 0.5 K are continuously observed in the Kuroshio-Oyashio extension region prior to the WN2AUT

peak (Figures 5-2e and 5-2f).

In the tropics, oceanographic conditions are characterized by La Niña-like condition except that in SD_30EPFz. However, only in SU_30EPFz, negative SST anomalies lower than -0.5 K in the equatorial Pacific persist throughout the period (Figures 5-2a and 5-2b), while, in WU_30EPFz and WD_30EPFz, the negative SST anomalies in the eastern equatorial Pacific fluctuate with a sub-seasonal time scale, which might be affected by the eastward propagation of the Madden-Julian Oscillation with the same time scale. Only SD_30EPFz shows no significant SST anomalies in the tropics. Therefore, it can be said that SU_30EPFz only indicates clear features of the La Niña like condition. Actually, 13 events among SU_30EPFz showed negative SST anomalies in the central or eastern equatorial Pacific in monthly time scale (not shown). We discuss the influence of these oceanographic conditions later in Section 5.

Left panels of Figure 5-3 show lag composite maps of seven-day-mean sea level pressure (SLP) anomalies during the period 10–4 days before the WN2AUT peak during the four groups. In SU_30EPFz (Figure 5-3a), the positive SLP anomalies larger than 9 hPa in relation to the development of the upper tropospheric ridge high around Alaska are statistically significant. Such positive SLP anomalies are also seen in WU_30EPFz (Figure 5-3c), but they are further weaker than those in SU_30EPFz. In WD_30EPFz and SD_30EPFz (Figures 5-3e and 5-3g), SLP anomalies around Alaska are still positive, but much weaker compared with those in SU_30EPFz. On the contrary, in SD_30EPFz (Figure 5-3g), the positive SLP anomalies larger than 7 hPa are observed over the region from

Northern Europe to Western Russia and are statistically significant. This suggests the development of the upper tropospheric ridge in this region. The positive SLP anomalies around Northern Europe are also seen in WD_30EPFz (Figure 5-3e), but are tiny and weaker than those in SD_30EPFz.

Right panels of Figure 5-3 show lag composite maps of seven-day-mean surface temperature anomalies during the period 7–1 days before the WN2AUT peak for the four groups. In relation to the development of the high-pressure system around Alaska, the negative surface temperature anomalies lower than -4.5 K are observed in North America and are statistically significant both in SU_30EPFz and in WU_30EPFz (Figures 5-3b and 5-3d). On the other hand, in WD_30EPFz and SD_30EPFz (Figures 5-3f and 5-3h), the wide-ranged negative surface temperature anomalies over the region from Europe to Central Asia are statistically significant.

Although all of the four groups were simply extracted from the WN2AUT events, we found out that the horizontal distributions of those surface conditions prior to the WN2AUT peak are different from each other. In particular, differences were clear between the upward groups (SU_30EPFz and WU_30EPFz) and downward group (SD_30EPFz and WD_30EPFz).

5.3 Time evolution of the wave-packet propagation in the upper troposphere

In this section, we examine the time evolution of the wave-packet propagation in the upper troposphere related to the WN2AUT events. Figure 5-4 shows lag composite maps of

Plumb's WAF and geopotential height deviations from the zonal mean for each day from six days before to two days after the WN2AUT peak in SU_30EPFz. For the period from the six days to four days before the WN2AUT peak (Figures 5-4a – 5-4c), wave packets corresponding to the quasi-stationary Rossby wave propagation along the sub-tropical jet are statistically significant over the North Pacific, and wave packets to the east of the Date Line indicate that waves are remarkably amplified in the region. For the period from four days to one day before (Figures 5-4c – 5-4f), a part of the wave packets propagate north-eastward and strengthen the ridge around Alaska. Furthermore, the upward propagation of the wave packets emanating from the ridge around Alaska begins to strengthen anomalies over North America and the northern part of the North Atlantic (Figures 5-5a and 5-5b). From one day before and the day of the WN2AUT peak (Figures 5-4f and 5-4g), northern part of wave packets emanating from the ridge around Alaska propagate eastward and upward (see also Figure 5-5c). After the WN2AUT peak (Figures 5-4h and 5-4i), those propagate eastward and upward into the higher levels (see also Figures 5-5d) and the upward propagation in the region persists several days (Figures 5-5e and 5-5f).

One of the important points is that the development of the upper tropospheric ridge around Alaska precedes that of the ridge around North Europe in SU_30EPFz. In addition, the development of the ridge around Alaska is mainly caused by the amplification of the quasi-stationary Rossby wave packets that propagate along the sub-tropical jet over the North Pacific. As for WU_30EPFz, the quasi-stationary Rossby wave propagation along the

sub-tropical jet is not statistically significant and the amplification of the wave is somewhat weaker than those in SU_30EPFz (not shown), although the preceding developments of the upper tropospheric ridge around Alaska are commonly seen.

Next, we consider the time evolution of wave-packet propagation in SD_30EPFz (Figure 5-6). In contrast to SU_30EPFz, the development of the upper tropospheric ridge around North Europe precedes that of the ridge around Alaska (Figures 5-6a and 5-6b). The wave packets emanating from the ridge around North Europe propagate eastward and upward over Siberia (Figures 5-6c – 5-6e, Figures 5-7a and 5-7b) and reach the ridge around Alaska three days before the WN2AUT peak (Figure 5-6f). For the period from three days to one day before the WN2AUT peak (Figures 5-6f – 5-6h), wave packets propagating from Siberia strengthen the ridge around Alaska and arrive over North America. However, in fact, these packets propagate downward in the region (Figure 5-7c), different from those in SU_30EPFz. The downward propagation takes a maximum value at the day of the WN2AUT peak (Figure 5-7d) and strengthen the upper tropospheric trough over North America and the negative surface temperature anomalies around -4.5 K prevail over North America (not shown).

Furthermore, in SD_30EPFz, the northward wave-packet propagation from the sub-tropical jet is not seen in contrast to those in SU_30EPFz but the wave-packet propagation over Siberia is more conspicuous. It should be noted that the WN2AUT peak is brought by the downward propagation from the lower stratosphere. In other words, it can be said that this is one of the examples of the influences of the stratosphere on the troposphere

during boreal winters. Actually, in the winter 2013/2014, averaged temperatures in North America were the second coldest of the period 1960–2014 (Yu & Zhang 2015), and downward propagation around 100°W and upward propagation around 60°E at the 100 hPa level were the strongest among the 56 winters since 1958/1959 (Harada & Hirooka 2017).

5.4 Time evolution of the wave-packet propagation from the upper troposphere to the stratosphere

We have shown the horizontal distribution of wave packet propagation. Here we show the features of the vertical wave-packet propagation before and after the WN2AUT peak during the four groups, namely, SU_30EPFz, WU_30EPFz, WD_30EPFz and SD_30EPFz. Left and right panels of Figure 5-8 show lag composite longitude–pressure cross sections of geopotential height deviations from the zonal-mean and Plumb's WAF before and after the WN2AUT peak during SU_30EPFz and SD_30EPFz, respectively.

As mentioned in the previous section, in SU_30EPFz, the wave packets emanating from the upper tropospheric ridge around Alaska propagate upward preceding the WN2AUT peak (Figures 5-8a and 5-8c) and most of geopotential height anomalies from the upper troposphere to the whole stratosphere become statistically significant after the WN2AUT event and vertical phase tilt is clearly westward with height (Figures 5-8e and 5-8g).

On the contrary, in SD_30EPFz, upward wave-packet propagation to the west of the Aleutian High precede the WN2AUT peak, and on the eastern edge of the Aleutian High, most of the wave packets propagate downward and strengthen the tropospheric trough over

North America (Figures 5-8d, 5-8f and 5-8h). Although a part of those wave packets seems to propagate into the upper stratosphere (Figures 5-8d and 5-8f), further propagation is unclear and geopotential height anomalies are not statistically significant in the Eastern Hemisphere of the upper stratosphere. It is worth noting that the center positions of the Aleutian High in SU_30EPFz and SD_30EPFz are different each other before the WN2AUT peak; that is, it is at the west of the Date Line in SU_30EPFz, while it is at the east of the Date Line in SD_30EPFz. The Aleutian High is more barotropic in the latter.

Furthermore, we compare the features in SU_30EPFz (left panels of Figure 5-8) with those in WU_30EPFz (left panels of Figure 5-9). In WU_30EPFz, the center position of the Aleutian High is shifted eastwards compared to that in SU_30EPFz before the WN2AUT peak (compare Figures 5-9a, 5-9c with Figures 5-8a, 5-8c) and statistically significant areas of geopotential anomalies are confined below the lower stratosphere, although the development of the ridge around Alaska is comparable to that in SU_30EPFz. Therefore, it can be said that the center position and vertical phase tilt of the Aleutian High are important in addition to the development of the ridge around Alaska for the realization of the strong upward propagation of WN2 in the stratosphere.

In WD_30EPFz, the upward wave-packet propagation to the west of the Aleutian High precedes the WN2AUT peak as shown in SD_30EPFz. Interestingly, the center position of the Aleutian High shifts eastward and the Aleutian High becomes quasi-barotropic after the WN2AUT. Our results are consistent with those in Harada & Hirooka (2017) which pointed out that the upward propagating portion of the wave packets emanating from the upper

tropospheric ridge around North Europe converges at the western edge of the Aleutian High and caused the development of the quasi-barotropic Aleutian High in the boreal winter 2013/2014.

5.5 Stratospheric circulation after WN2AUT peak

Left panels of Figure 5-10 exhibit lag composite maps of geopotential height anomalies at 30 hPa two days after the WN2AUT peak. In SU_30EPFz and WU_30EPFz (Figures 5-10a and 5-10c), the WN2 amplification in the lower stratosphere prevail, although the negative height anomalies related to the trough over North America are much stronger than those related to the other trough and ridges. On the other hand, in WD_30EPFz and SD_30EPFz (Figures 5-10e and 5-10g), the WN2 amplification is not identified. In particular, in SD_30EPFz (Figure 5-10g), the WN1-like anomaly pattern, which indicates the development of the Aleutian High is distributed despite the WN2 amplification in the upper troposphere. Moreover, in SU_30EPFz, the upper stratospheric circulation four days after the WN2AUT peak indicates the complete polar vortex splitting (Figure 5-10b). Even in WU_30EPFz, the elongation of the polar vortex is clearly seen (Figure 5-10d). On the other hand, in WD_30EPFz and SD_30EPFz (Figures 5-10f and 5-10h), both negative height anomalies within the polar vortex and positive height anomalies in the lower latitudes are statistically significant. This indicates the deepening of the polar vortex and the acceleration of the polar night jet. Anyhow, there are large differences of the stratospheric circulation after the WN2AUT peak in the upper troposphere among the four groups.

5.6 Discussion of the role of the La Niña-like oceanographic condition

We have shown the results of composite analysis and found that the tropical oceanographic conditions are characterized by La Niña-like condition prior to the WN2AUT peak except SD_30EPFz. In addition, the development of the upper tropospheric ridge around Alaska is also one of common features in SU_30EPFz and WU_30EPFz. In particular, we found that in SU_30EPFz, the quasi-stationary Rossby wave propagation along the sub-tropical jet are statistically significant over the North Pacific and the wave packets are amplified to the east of the Date Line prior to the WN2AUT peak. We also have shown the amplified wave-packets play an important role in the development of the upper tropospheric ridge around Alaska. Barriopedro & Calvo (2014) pointed out that the eastern Pacific Blocks are more frequent during La Niña, which are consistent with our results. However, specific mechanisms that La Niña condition effects on the frequency of the eastern Pacific Blocks were not described in their study. Therefore, here we discuss plausible amplification mechanisms of the wave packet around the east of the Date Line and the contribution of the La Niña-like oceanographic condition.

Figure 5-11 shows composite maps of 31-day-mean zonal winds and anomalies at 250hPa during La Niña winters for the current analysis period. In the eastern part of the North Pacific, the negative (easterly) anomalies around the east of the Date Line are statistically significant. These anomalies are located in the subtropical jet exit region and indicating the strong zonal wind deceleration there and the formation of the sharp sub-tropical jet exit region in the North Pacific. The previous studies have shown that the

Rossby waves become frequently stagnant and are amplified in this jet exit region (Naoe et al. 1997; Hitchman & Huesmann 2007). Hence, it can be considered that such a condition during La Niña winters is more favorable for the amplification of Rossby waves compared to that during El Niño winters, which leads to positive (westerly) anomalies around the east of the Date Line and the eastward extension of the subtropical jet exit region (not shown).

Furthermore, to confirm the features of the Rossby wave propagation in the North Pacific during ENSO winters, we investigated normalized frequency of meridional components of Plumb's WAF (WAFy) at 250 hPa in the northern part of the sub-tropical jet exit region during ENSO winters to clarify differences between El Niño and La Niña winters (Figure 5-12). During La Niña winters (blue bars in Figures 5-12a and 5-12b), frequency of extremely northward and southward propagation of Rossby waves (absolute values of WAFy are found to be more than 35) greatly increase compared to those during El Niño winters (red bars in Figures 5-12a and 5-12b). This tendency becomes more evident in the case of stronger ENSO (compare Figures 5-12a and 5-12b). On the other hand, during El Niño winters, frequency of weak meridional propagation apparently increases compared to those during La Niña winters. It corresponds to the eastward extension of the subtropical jet exit region during El Niño winters. In fact, no significant difference between ENSO winters in composite of seasonal averaged WAFy in the eastern part of the North Pacific (not shown). However, the evident increase of frequency of extremely northward propagation in the northern part of the sub-tropical jet exit region is further important to the development of the upper tropospheric ridge around Alaska.

6. Diagnostics of a WN2-type Major Sudden Stratospheric Warming Event in February 2018 using a new Three-Dimensional Wave Activity Flux

6.1 Overall features of MSSW18 and comparisons with the previous WN2-type MSSW events

A WN2 type MSSW event occurred in February 2018 (MSSW18). An evident splitting of the polar vortex was observed from 11 to 12 February 2018 as shown in Figure 6-1. This is the first vortex-splitting event in nine years since the MSSW event that occurred in the second half of January 2009 (MSSW09; Harada et al. 2010).

As described in Introduction, the World Meteorological Organization (WMO) defines "major warming" as the zonal-mean zonal winds become easterly north of 60°N at 10 hPa or below (WMO 1978, item 9.4, 35–36). Recently, Butler et al. (2015) discussed the definitions of sudden stratospheric warming (SSW) and proposed usage of a latitudinal average of zonal wind rather than at a particular latitude, or usage of 65°N instead of 60°N, which may decrease the sensitivity to changes in the polar-vortex edge. Hence, we adopt the zonal-mean zonal wind at 65°N for our analysis shown herein.

Figures 6-2a and 6-2b show time–pressure cross sections of zonal-mean temperatures averaged over 80°–82.5°N and zonal-mean zonal wind at 65°N during the winter of 2017/2018. In the first half of January 2018, temperatures in the lower stratosphere are lower than 195 K and the westerly winds are 60 m s^{-1} or more in the upper stratosphere, thereby indicating that the polar vortex has been undisturbed in that period. From

mid-January 2018 to early February 2018, several weak warmings and zonal-wind decelerations are observed in the stratosphere because of several upward propagations of planetary waves including both WN1 and WN2 from the upper troposphere in terms of time changes of EPFz averaged over 30°–90°N at 100 hPa (Figure 6-3a); the consequence is weakening of the polar night jet (PNJ). In mid-February, clear pronounced warming occurs in both the upper and lower stratosphere, and the area of temperature with more than 240 K extensively appears and reaches roughly the 50-hPa level (Figure 6-2a). Zonal winds decelerate almost simultaneously throughout the entire stratosphere, and easterlies become predominant and persist until the end of the month (Figure 6-2b). These features qualify the definition of MSSW. However, compared with the previous events, MSSW18 exhibits relatively modest temperature warming. In this regard, it is similar to that in MSSW89 (Figure 6-2e) but different from MSSW09 (Figure 6-2c), the latter exhibiting a sharp warming and zonal-wind deceleration.

On the other hand, the stratospheric easterly wind during MSSW18 exhibits clear double peaks, both of which exceed 25 m s^{-1}, and are stronger than that in MSSW89 (weaker than the strong single peak during MSSW84). This is one of the remarkable features of MSSW18. Figure 6-4 shows latitude-time cross sections of the 10-hPa zonal-mean zonal winds. The double peaks of the easterlies during MSSW18 are evident at the 10-hPa pressure level (Figure 6-4a), and the period during which the extension of easterlies to the south of 60°N persists is longer than those in the other WN2-type MSSW events (Figures 6-4c – 6-4e) except for MSSW09 (Figure 6-4b).

Here, we focus on the time-evolution of planetary-wave propagation during MSSW18 (Figure 6-3a). In February 2018, there are surges of upward planetary-wave propagation at the 100-hPa level, with clear double peaks around 10 and 20 February 2018 that correspond to the aforementioned easterly double peaks. In this regard, the extraordinary upward planetary-wave propagation from the upper troposphere played an important role in the occurrence of MSSW18.

Furthermore, at the 100-hPa level, the peak value of EPFz is comparable to that in January 2009 (Figure 6-3c) and much stronger than those in other MSSW winters (Figures 6-3e, 6-3g and 6-3i). However, the peak value of EPFz at the 5-hPa level (Figure 6-3b) is evidently lower than those during MSSW09 (Figure 6-3d) and MSSW84 (Figure 6-3h), and is instead comparable with that during MSSW89 (Figure 6-3f). These suggest that during MSSW18 substantial amount of the wave packets that propagated from the upper troposphere were either absorbed or reflected in the lower stratosphere. This could be one reason why the stratospheric temperature warming was relatively modest despite the extraordinary upward EPFz from the upper troposphere. In Section 6.2, we show further details of the wave-packet propagation, focusing on both latitudinal and longitudinal distributions.

6.2 Daily wave-packet propagation during MSSW18

We now show the details of the wave-packet propagation in the stratosphere during MSSW18 and compare them with those during MSSW09 and the other previous WN2-type

MSSW events. Figure 6-5 illustrates meridional cross sections of zonal-mean zonal wind, EP fluxes and EP flux divergence for the daily-mean field in the Northern Hemisphere during MSSW18. On 8 February 2018 (Figure 6-5a), there is clear upward-wave-packet propagation from the upper troposphere. Although westerlies are predominant in the entire stratosphere, most wave packets do not attain the upper stratosphere and the EP flux convergence is confined to the lower stratosphere. From 10 to 11 February 2018 (Figures 6-5c and 6-5d), the wave packets reach the upper stratosphere and the strengthened EP flux convergence causes large zonal-wind deceleration in that region. After 12 February 2018 (Figures 6-5e – 6-5g), upward wave-packet propagation continues in the upper stratosphere despite the fact that easterlies become predominant at higher latitudes in the stratosphere.

Next, we compare the daily wave-packet propagation during MSSW18 with that during MSSW09. Figure 6-6 shows meridional cross sections of zonal-mean zonal winds, EP fluxes and their divergence for the peak period of upward wave-packet propagation during MSSW09. Unlike during MSSW18, wave packets obviously reach above the 3-hPa level and remarkable EP flux convergence is distributed widely in the region from the upper stratosphere up to the lower mesosphere. During MSSW09, the PNJ with a core speed of over 70 m s^{-1} is much stronger than that during MSSW18. Wave packets propagate continuously in the westerly region and converged to the southern flank of the core of PNJ. After 20 January 2009, although easterlies prevail in the upper stratosphere and above, upward wave-packet propagation and strong EP flux convergence persists in the region from the upper stratosphere to the lower mesosphere.

The results show that the regions of EP flux convergence during MSSW18 are lower than those during MSSW09. At the beginning of MSSW18, westerlies are predominant in the entire stratosphere of the Northern Hemisphere but upward wave-packet propagation is nevertheless confined to the lower stratosphere. However, note that the extent to which we can explain the behavior of wave packets in the atmosphere using the zonal mean field is limited despite the fact that its usage is highly advantageous and beneficial for diagnosing of MSSW events. Hence, we calculate 3D-flux-W during MSSW18 and examine the time evolution of wave-packet propagation. Figure 6-7 shows horizontal distributions of vertical 3D-flux-W components (3D-flux-Wz) averaged over successive three days at 5 hPa for the period from early to mid-February 2018, along with geopotential height deviations from the zonal averages. In early February (Figure 6-7a), the Aleutian High is stronger than another high over the North Atlantic, though the upward propagation of WN2 planetary waves from the upper troposphere is conspicuous (see also Figure 6-3a). During this period, there exists weak upward propagation of wave-packets over Eurasia in the Eastern Hemisphere and downward propagation in the Western Hemisphere, which seem to be almost canceled out each other. The upward propagation in the Eastern Hemisphere is attenuated afterwards. Meanwhile, in the Western Hemisphere, evident and localized upward propagation of wave packets appear over North America (Figures 6-7b and 6-7c). During 16–18 February (Figure 6-7d), wave packets over North America is also attenuated, as MSSW18 ceased. Here, we find the clear localization of upward wave-packet propagation even in the upper stratosphere. These results suggest the contribution of smaller-scale waves to form localized

wave packets, as will be discussed later in Section 5.

Next, we show vertical and longitudinal distributions of wave-packet propagation using 3D-flux-W. Figure 6-8 illustrates the time evolution of daily wave-packet propagation in the longitude–pressure plane. At the beginning of February 2018, there is clear downward propagation of wave-packets in the Western Hemisphere (Figures 6-8a and 6-8b), which is related to the temporal zonal-wind acceleration in the lower stratosphere (Figure 6-2b). An upper-tropospheric ridge then begins to develop around Alaska (around 150°W), and wave packets that are emanated from that ridge begin to propagate upward (Figures 6-8c and 6-8d) and nearly reach the stratopause (Figure 6-8e). Consequently, the upward wave-packet propagation stemming from the ridge around Alaska persists until late that month (Figures 6-8f – 6-8h). In addition, there is another upward propagation in the Eastern Hemisphere at the same time. The simultaneous upward propagation of wave packets in both Hemispheres may explain the remarkable peak of EPFz at the 100-hPa level as shown in Figure 6-3a. However, the wave packets in the Eastern Hemisphere converge strongly at the western edge of the Aleutian High (90°–150°E) and most of them do not propagate into the upper stratosphere (Figures 6-8b – 6-8d; see also Figures 6-5a and 6-7a).

Harada & Hirooka (2017) conducted a case study on observational features of the boreal winter of 2013/2014 which was characterized by a continuous predominance of WN2 that did not cause MSSW, and pointed out that the importance of the longitudinal distribution of wave-packet propagation in the case of WN2 predominance. Wave packets propagating toward the Aleutian High converged repeatedly at the western edge of the

quasi-barotropic Aleutian High, and most of them did not propagate into the upper stratosphere. It is noteworthy that the strong convergence of upward wave packets in the Eastern Hemisphere at the beginning of MSSW18 is consistent with the results obtained by Harada & Hirooka (2017). In fact, there were several upward propagations of planetary waves, including both WN1 and WN2 from the upper troposphere from mid-January 2018 to early February 2018 as described in Section 4.1, in the Eastern Hemisphere (not shown) and those not only weakened the PNJ but also developed the Aleutian High.

Figure 6-9 compares the vertical and longitudinal distributions of upward wave-packet propagation at each peak of upward planetary-wave propagation during the previous WN2-type MSSW events. Localized upward propagation of wave packets is commonly observed in the Western Hemisphere in all of the events, which is consistent with the features of MSSW18. Furthermore, wave packets emanate from the upper-tropospheric ridge around Alaska (120°–150°W) in all the previous events except MSSW84. During MSSW84, the upward propagation of wave packets seems to spread longitudinally instead.

Therefore, we further investigate the relationship between the time evolution of the upper-tropospheric ridge around Alaska and that of upward wave-packet propagation from the troposphere to the stratosphere (Figure 6-10). It is apparent that remarkable upward propagation of wave packets occurs in association with the development of the upper-tropospheric ridges around Alaska and as located to the east of the ridges during MSSW18 (Figure 6-10a). Moreover, MSSW18 exhibits evident double peaks of upward wave-packet propagation around both 10 and 18 February 2018 that are closely related to

the appearance of the easterly double peaks at the upper stratosphere (Figures 6-2b and 6-4a). This simultaneous occurrence of the upper-tropospheric ridge around Alaska and strong upward propagation are also observed during the previous WN2-type MSSW events except for MSSW84. In particular, the event in the second half of January 1963 (Figure 6-10e) shows extraordinary upward propagation similar to that during MSSW18. From these results, we argue that the persistence of the upper-tropospheric ridge around Alaska plays an important role in the formation of WN2-type MSSW events. Our results are consistent with those of previous studies that have shown that vortex splits are preceded by blocks in the Pacific Basin or in both the Atlantic and Pacific basins, whereas vortex displacements are preceded by blocking over the Atlantic basin only (e.g., Mukougawa et al. 2005; Martius et al. 2009; Castanheira & Barriopedro 2010; Harada et al. 2010; Nishii et al. 2011; Bancalá et al. 2012). Moreover, Barriopedro & Calvo (2014) pointed out that SSW events during La Niña conditions are associated predominantly with WN2 amplification. Indeed, note that the oceanographic conditions in the tropics during the winter of 2017/2018 were those of La Niña (not shown).

6.3 Discussion of the cause of the suppression of the upward wave-packet propagation during MSSW18

We have shown that planetary-wave propagation in the upper stratosphere during MSSW18 was much weaker than that during MSSW09 despite the fact that the remarkable planetary-wave propagation from the upper troposphere during MSSW18 was comparable

to that during MSSW09. Here we discuss the cause of the suppression of the upward wave-packet propagation during MSSW18.

Figure 6-11 compares the longitudinal distributions of 3D-flux-Wz for various zonal wavenumber ranges for 10–12 February 2018 (left panels) and 18–20 January 2009 (right panels). It is evident that smaller-scale waves (WN5 or more) should be taken into account even in the upper stratosphere to represent the longitudinal distribution of upward wave-packet propagation accurately, particularly its strong peak. We also show the filtered meridional wind for various zonal wavenumber ranges in longitude–pressure sections to detect vertical phase tilts of WN1 planetary waves (Figures 6-12a and 6-12b), WN2 ones (Figures 6-12c and 6-12d), and smaller-scale waves (Figures 6-12e – 6-12h) during the two periods as shown in Figure 6-11. Although the westward phase tilt of WN2 is clear in both cases (Figures 6-12c and 6-12d), it is zonally uniform and cannot explain the localized feature of 3D-flux-Wz as shown in Figure 6-11.

We now compare the details of upward wave-packet propagation with the distribution of vertical phase tilts of smaller-scale waves. First, we focus on the region around 120°W in the lower stratosphere during 10–12 February 2018 (Figures 6-11e and 6-11g). At the 50-hPa level (Figure 6-11g), the maximum value of 3D-flux-Wz was over 30×10^{-2} kg m^{-1} s^{-2} but it decreases to 25×10^{-2} kg m^{-1} s^{-2} at the 30-hPa level (Figure 6-11e). Weak eastward phase tilts of smaller-scale waves are also evident in the same region (Figures 6-12e and 12g). Moreover, in the upper stratosphere (Figures 6-11a and 6-11c), there is clear attenuation of 3D-flux-Wz around 60°W. In that region, the vertical phase tilts are

very weak and the smaller-scale waves seem to have been quasi-barotropic (Figures 6-12e and 6-12g). Consequently, at the 5-hPa level absolute values of 3D-flux-Wz during MSSW18 (Figure 6-11a) are only roughly half of those during MSSW09 (Figure 6-11b). Meanwhile, during MSSW09 (Figures 6-12f and 6-12h), westward phase tilts of smaller-scale waves are evident in the upper stratosphere, particularly around 60°W and from 60° to 120°E.

Moreover, we note that, during 13–15 February 2018, the decrease of 3D-flux-Wz in the upper stratosphere is much less than that during 10–12 February 2018 and there is evident westward tilts of smaller-scale waves in the upper stratosphere (not shown), although easterlies become predominant in the upper stratosphere during the period as mentioned in Section 6.2.

The smaller-scale waves described herein have been referred to as medium-scale waves (WN4–7) since the 1970s, and numerous studies have been conducted using satellite observation data focused on the Southern Hemisphere (e.g., Kao et al. 1970; Randel & Stanford 1985; Miles & Grose 1986). The existence of such waves in the Northern Hemisphere has been pointed out, and analytical studies have been conducted (e.g., Hirooka et al. 1988; Sato et al. 2000). In addition, the results of the spectral analysis conducted by Tomikawa & Sato (2003) suggest that such waves also exist in the boreal-winter Northern Hemisphere stratosphere, although the role of the smaller-scale waves in the occurrence of MSSW in the Northern Hemisphere had not been focused so far. However, the results described above suggest that smaller-scale waves (WN5 or more) play

an important role in representing the distribution of upward wave-packet propagation, and the contribution of smaller-scale waves could be one reason why planetary-wave propagation in the upper stratosphere during MSSW18 was weaker than that during MSSW09.

Moreover, a plausible mechanism for the generation of smaller-scale waves might be planetary-wave breaking (e.g., Matsuno & Hirota 1966) and/or instability in the stratosphere (e.g., Phister 1979; Mukougawa et al. 2017). In particular, the recent study by Mukougawa et al. (2017) calculated unstable modes to the observed basic flow in the upper stratosphere for the SSW event in 2007. They showed that the barotropic instability inherent to the upper-stratospheric circulation brought about the highly distorted polar vortex due to the contribution of smaller-scale waves. A similar mechanism might occur during MSSW09, contributing to the behavior of wave-packets in the stratosphere. However, the appearance of the instability associated with the polar vortex evolution is still unclear and further studies would be needed.

7. Summary and Conclusions

In this study, three analyses on the characteristics of the planetary wave packet propagation during boreal winter are conducted by using JRA-55.

First, we have examined observational features of the winter 2013/2014 using JRA-55 data and found that the EPFz of WN2 for the winter 2013/2014 is almost equal to the highest value of the winter 2008/2009 (when an intensive major SSW occurred). Comparing the longitudinal distribution of the WAFz among the WN2 winters, the WAFz for the winter 2013/2014 is characterized by remarkable downward propagation around 100°W and upward propagation around 60°E, both of which are the strongest of their type among the 56 winters since 1958/1959. In contrast, strong and localized upward propagation in the region east of 180° is commonly seen prior to the WN2-type major SSWs. We also found that longitudinal distributions of the WAFz for both the WN2_noMSSW (winters without the WN2-type SSW occurrence) and the WN2_MSSW (winters with the WN2-type SSW occurrence) differ from those for WN1 winters; that is, upward propagation of wave packets for the WN2_noMSSW largely exceeds the standard deviation range of WAFz for WN1 winters from 30°E to 60°E, whereas downward propagation is much larger than that for the WN1 winters from 150°W to 90°W. In addition, upward propagation of the wave packet for the WN2_MSSW exceeds the standard deviation range of the WN1 winters around 165°W.

Next, we have investigated the influence of upward wave packet propagation on stratospheric circulation. The convergence of wave packets propagating from around 60°E

contributed to the development and continuance of the quasi-barotropic Aleutian High. In particular, the development of the quasi-barotropic Aleutian High during the period from late December 2013 to mid-January 2014 was extraordinary. The remarkable zonal wind deceleration, accompanied by the development of the Aleutian High, contributed to the further convergence of the wave packets propagating to the west of the Aleutian High and to the continuation of the quasi-barotropic Aleutian High itself. Accordingly, the wave packets emanating from the tropospheric blocking highs developing in the North Pacific Ocean converged or reflected in the lower edge of the extended negative refractive index (Ks) region related to the extraordinary development of the quasi-barotropic Aleutian High, which is one of the reasons for a lack of major SSW occurrence in the winter 2013/2014.

Our analysis also revealed the significant contribution of smaller scale waves (with WN3 or more) to the presentation of localized wave packet propagation not only in the troposphere but also in the lower stratosphere. We have exhibited the case in which upward (downward) wave packet propagation was clearly observed to the west (east) of the quasi-barotropic Aleutian High: Vertical phase tilts of WN3 or more are distinct and consistent with the vertical propagation of wave packets (in contrast to those of WN1 and WN2, which present as almost barotropic). Moreover, when including only the WN1 and WN2 components, at the 100 and 50 hPa levels, the estimation of WAFz is just one third of that estimated for the downward propagation around 110°W when all wavenumbers are used for the winter 2013/2014. These results confirm the importance of smaller scale waves in the presentation of localized wave packet propagation in the stratosphere.

Future studies should clarify the details of localized wave packet propagation, focusing on the role of smaller scale waves in the stratosphere as well as the dynamical relationship between the blocking activity in the North Pacific basin, the La Niña-like conditions, the tropospheric conditions from the Atlantic to Europe, and the extraordinary WN2 propagation from the troposphere.

Second, we have performed composite analysis and shown the time evolution and characteristic features of "wave amplification events" of upper-tropospheric WN2 during the boreal winter using JRA-55. First we extracted strong WN2 amplification events that 250VVAR_WN2 exceeds one SD from all samples of 60 winters since 1958/1959 (WN2AUT), and further extracted the four groups from these events on the basis of values of 30EPFz_WN2 two days after WN2AUT peaks, i.e., strong upward WN2 propagation group (SU_30EPFz), weak upward WN2 propagation group (WU_30EPFz), weak downward WN2 propagation group (WD_30EPFz), and strong downward WN2 propagation group (SD_30EPFz). The results of our composite analysis are summarized as follows:

1) Tropical oceanographic conditions prior to the WN2AUT peak are characterized by La Niña-like conditions except that in SD_30EPFz. In particular, the persistence of negative SST anomalies less than 0.5 K in the central and eastern equatorial Pacific is observed only in SU_30EPFz. On the hand, SD_30EPFz shows no significant SST anomalies in the tropics. As for the extra-tropical oceanographic conditions, in WD_30EPFz, the positive SST anomalies more than 0.5 K are continuously observed

in the Kuroshio-Oyashio extension region prior to the WN2AUT peak.

2) In SU_30EPFz and WU_30EPFz, surface conditions prior to the WN2AUT peak are characterized by the high pressure anomalies around Alaska and the negative surface temperature anomalies over North America in relation to the development of the upper tropospheric ridge in the region. The high pressure anomalies around Alaska in SU_30EPFz are much stronger than those in WU_30EPFz. On the contrary, in SD_30EPFz and WD_30EPFz, those are characterized by the high pressure anomalies around Northern Europe and the negative surface temperature anomalies from Europe to Central Asia. The high pressure anomalies around Northern Europe in SD_30EPFz are much stronger than those in WD_30EPFz.

3) The time evolution of the wave-packet propagation in the upper troposphere prior to the WN2AUT peak in SU_30EPFz is characterized by the significant quasi-stationary Rossby wave propagation along the sub-tropical jet and the wave packets around the east of the Date line are clearly amplified, which propagate north-eastward, and then strengthen the upper tropospheric ridge around Alaska at the WN2AUT peak. The wave packets emanating from the ridge around Alaska propagate upward into the stratosphere. On the contrary, in SD_30EPFz, the development of the upper tropospheric ridge around North Europe precedes that of the ridge around Alaska, and the wave packets emanating from the ridge around North Europe propagate eastward

and upward into the lower stratosphere over Siberia. Consequently, these wave packets propagate downward and strengthen the trough in North America in the troposphere.

4) Comparison of the time evolution of the wave-packet propagation from the upper troposphere to the stratosphere around the WN2AUT peak indicates the importance of the center position and vertical phase tilt of the Aleutian High. The center of the Aleutian High located to the west of the Date Line is favorable to the strong upward propagation of wave packets throughout the stratosphere (SU_30EPFz). In the case that the center of the Aleutian High is located to the east of the Date Line, the strong upward wave-packet propagation is confined to the lower stratosphere (WU_30EPFz). The wave-packet propagation from the Eastern Hemisphere tends to make the Aleutian High more quasi-barotropic, and such a condition is favorable to the downward wave-packet propagation to the east of the Aleutian High (SD_30EPFz and WD_30EPFz).

5) Stratospheric circulations after WN2AUT peak in SU_30EPFz WU_30EPFz are characterized by the clear WN2 amplification in the lower stratosphere. In particular, SU_30EPFz indicates the complete polar vortex splitting. On the other hand, WD_30EPFz and SD_30EPFz indicate the development of the Aleutian High in the lower stratosphere and the deepening the polar vortex.

Our results, in particular, shown in SU_30EPFz are consistent with those in the previous studies. It is noteworthy that the sole development of the upper tropospheric ridge around Alaska play a crucial role in the occurrence of the strong upward WN2 wave-packet propagation. On the other hand, our results shown in SD_30EPFz and WD_30EPFz are consistent with those in Harada & Hirooka (2017): The wave packet emanating from the ridge around North Europe tend to cause the development of the quasi-barotropic Aleutian High that prevents WN2 wave packets from propagating upward into the upper stratosphere.

We also examined roles of the La Niña-like condition in the tropical ocean influencing the quasi stationary Rossby wave wave-packet over the North Pacific. During La Niña winters, the large zonal wind deceleration and the formation of the sharp sub-tropical jet exit region in the North Pacific are statistically significant. It can be considered that such a condition in the region during La Niña winters is more favorable for the amplification of Rossby waves compared to that during El Niño winters. We further investigated normalized frequency of meridional component of WAFy at 250 hPa in the northern part of the sub-tropical jet exit region during ENSO winters. We found that, during La Niña winters, frequency of extremely northward and southward propagation of Rossby waves greatly increase compared to those during El Niño winters.

Moreover, we analyzed observational features of atmospheric fields during MSSW18 using 3D-flux-W formulated by Kinoshita & Sato (2013a, 2013b) as a new analysis tool, and we compared those features with those during previous WN2-type

MSSW events. MSSW18 was characterized by a clear polar-vortex split and the persistence of easterlies with clear double peaks. Nevertheless, the stratospheric temperature warming was relatively modest, which is different from that during MSSW09. Another feature of MSSW18 was extraordinary upward propagation of WN2 planetary waves from the upper troposphere, the peak of which was comparable to that during MSSW09. The upward propagation also had clear double peaks, thereby explaining those of the easterly winds. It is also noteworthy that zonal-wind deceleration due to several upward propagations of planetary waves prior to MSSW18 played an important role in the occurrence of the polar-vortex split during MSSW18.

We further investigated the details of the wave-packet propagation in the stratosphere during MSSW18. In the zonal-mean field, we found that EP flux convergence was confined to the lower stratosphere in the early stage of MSSW18 despite the fact that westerlies were predominant in the entire stratosphere of the Northern Hemisphere. According to 3D analyses using 3D-flux-W, the upward wave-packet propagation occurred simultaneously in both the Eastern and Western Hemispheres. In the Eastern Hemisphere, the wave packets converged strongly at the western edge of the Aleutian High and most of them did not propagate into the upper stratosphere, consistent with Harada & Hirooka (2017); this can be regarded as one reason for the modest temperature warming during MSSW18. By contrast, the wave packets in the Western Hemisphere propagated into the upper stratosphere despite the fact that easterlies were predominant there during the mature stage of MSSW18.

We also compared the longitudinal distributions of upward wave-packet propagation at each peak of the upward propagation during MSSW18 with those during the previous WN2-type MSSW events. We found that localized upward propagation of wave packets was common in the Western Hemisphere during all of the previous events and that wave packets emanated from the upper-tropospheric ridge around Alaska in all the previous events except for MSSW84.

Furthermore, we discussed plausible mechanisms for the suppression of upward wave-packet propagation during MSSW18. Comparing upward wave-packet propagation and vertical phase tilts of smaller-scale waves revealed that the regions and levels of wave-packet attenuation corresponded well with the area of weak eastward phase tilts or the quasi-barotropic condition of smaller-scale waves during MSSW18. On the contrary, during MSSW09, the westward phase tilts of smaller-scale waves were evident in the stratosphere. These results indicate the importance of smaller-scale waves in representing the distribution of upward wave-packet propagation.

As shown throughout our study, there were several interesting features during MSSW18, one being clear planetary-wave propagation despite the predominance of easterlies in the upper stratosphere. In particular, it would be difficult to understand the behavior of a localized wave-packet propagating in the stratosphere on the basis of any analyses in the zonal-mean field. Therefore, we introduce effective analyses based on 3D-flux-W. Using 3D-flux-W, we showed that wave-packet propagation to be localized even in the upper stratosphere. We conclude that 3D analysis is inevitable if we wish to

understand fully the dynamics of MSSW events.

Finally, note that we are yet to clarify the origin of smaller-scale waves in the stratosphere. One possibility is that they originate from the troposphere and propagate into the lower stratosphere; another is that they are generated internally by planetary-wave breaking and/or instability in the stratosphere (e.g., Matsuno & Hirota 1966; Phister 1979; Mukougawa et al. 2017). In future work, we intend to conduct further investigation focusing on smaller-scale waves in the stratosphere.

Acknowledgments

I deeply appreciate to Prof. Toshihiko Hirooka at the Department of Earth and Planetary at Kyushu University for his invaluable advices. I express deep thanks to Prof. Ryuichi Kawamura and Associate Prof. Yasunobu Miyoshi at the Department of Earth and Planetary at Kyushu University for their advices and suggestions. I am grateful to Dr. Hiroaki Naoe at Meteorological Research Institute, who gave me an opportunity for the study of the dynamics of the atmosphere and have encouraged me for scientific activities for a decade. I am grateful to Prof. Hisashi Nakamura at University of Tokyo, who originally developed and offered the calculation tool of the extended refractive index for stationary waves. Finally, I express my deepest gratitude to my family and colleagues for their support and encouragement.

References

Aiki, H., K. Takaya, & Greatbatch R. J. (2015). A divergence-form wave-induced pressure inherent in the extension of the Eliassen–Palm theory to a three-dimensional framework for all waves at all latitudes. *Journal of the Atmospheric Sciences*, **72**, 2822-2849. https://doi.org/10.1175/JAS-D-14-0172.1

Andrews, D. G., Holton, J. R., & Leovy, C. B. (1987). Middle atmosphere dynamics, (p. 489). Orland: *Academic Press*.

Andrews, D. G., & Mclntyre, M. E. (1976). Planetary waves in horizontal and vertical shear: The generalized Eliassen–Palm relation and the mean zonal acceleration. *Journal of the Atmospheric Sciences*, **33**(11), 2031–2048. https://doi.org/10.1175/1520-0469(1976)033<2031: PWIHAV>2.0.CO;2

Bancalá, S., Krüger, K., & Giorgetta, M. (2012). The preconditioning of major sudden stratospheric warmings. *Journal of Geophysical Research*, **117**, D04101. https://doi.org/10.1029/2011JD016769

Barriopedro, D., & Calvo, N. (2014). On the relationship between ENSO, stratospheric sudden warmings, and blocking. *Journal of Climate*, **27**(12), 4704–4720. https://doi.org/10.1175/JCLI-D-13-00770.1

Butler, A. H., & Polvani, L. M. (2011). El Niño, La Niña, and stratospheric sudden warmings: A reevaluation in light of the observational record. *Geophysical Research Letters*, **38**, L13807. https://doi.org/10.1029/2011GL048084

Butler, A. H., Seidel, D. J., Hardiman, S. C., Butchart, N., Birner, T., & Match, A. (2015).

Defining sudden stratospheric warmings. *Bulletin of the American Meteorological Society*, **96**(11), 1913–1928. https://doi.org/10.1175/BAMS-D-13-00173.1

Butler, A. H., Sjoberg, J., Seidel, D. J., & Rosenlof, K. H. (2017). A sudden stratospheric warming compendium. *Earth System Science Data*, **9**(1), 63–76. https://doi.org/10.5194/essd-9-63-2017

Calvo, N., Garcia, R. R., Randel, W. J., & Marsh, D. R. (2010). Dynamical mechanism for the increase in tropical upwelling in the lowermost tropical stratosphere during warm ENSO events. *Journal of the Atmospheric Sciences*, **67**(7), 2331–2340. https://doi.org/10.1175/ 2010JAS3433.1

Castanheira, J. M., & Barriopedro, D. (2010). Dynamical connection between tropospheric blockings and stratospheric polar vortex. *Geophysical Research Letters*, **37**, L13809. https://doi.org/10.1029/2010GL043819

Chandran, A., Collins, R. L., Garcia, R. R., Marsh, D. R., Harvey, V. L., Yue, J. & de la Torre, L. (2013). A climatology of elevated stratopause events in the whole atmosphere community climate model. *J. Geophys. Res.*, **118**, 1234–1246. https://doi.org/10.1002/jgrd.50123

Charlton, A. J., & Polvani, L. M. (2007). A new look at stratospheric sudden warmings. Part I: Climatology and modeling benchmarks. *Journal of Climate*, **20**(3), 449–469. https://doi.org/10.1175/JCLI3996.1

Colucci, S. J., & Kelleher, M. E. (2015). Diagnostic comparison of tropospheric blocking events with and without sudden stratospheric warming. *Journal of the Atmospheric*

Sciences, **72**(6), 2227–2240. https://doi.org/10.1175/JAS-D-14-0160.1

Davini, P., Cagnazzo, C., & Anstey, J. A. (2014). A blocking view of the stratosphere-troposphere coupling. *Journal of Geophysical Research: Atmospheres*, **119**(19), 11,100–11,115. https://doi.org/10.1002/2014JD021703

Duchon, C. E. (1979). Lanczos filtering in one and two dimensions. *Journal of Applied Meteorology*, **18**(8), 1016–1022. https://doi.org/10.1175/1520-0450(1979)018<1016:LFIOAT>2.0.CO;2

Finger, F. G., & Teweles, S. (1964). The mid-winter 1963 stratospheric warming and circulation change. *Journal of Applied Meteorology*, **3**(1), 1–15. https://doi.org/10.1175/1520-0450(1964)003<0001:TMWSWA>2.0.CO;2

Harada, Y., Goto, A., Hasegawa, H., Fujikawa, N., Naoe, H., & Hirooka, T. (2010). A major stratospheric sudden warming event in January 2009. *Journal of the Atmospheric Sciences*, **67**(6), 2052–2069. https://doi.org/10.1175/2009JAS3320.1

Harada, Y., & Hirooka, T. (2017). Extraordinary features of the planetary wave propagation during the boreal winter 2013/2014 and the zonal wave number two predominance. *Journal of Geophysical Research*, **122**, 11374–11387. https://doi.org/10.1002/2017JD027053

Harada, Y., K. Sato, T. Kinoshita, R. Yasui, T. Hirooka, and H. Naoe; under revision in *Journal of Geophysical Research*.

Hirooka, T., Kuki, T., & Hirota, I. (1988). An intercomparison of medium-scale waves in the Northern and Southern Hemispheres. *Journal of the Meteorological Society of*

Japan, **66**, 857–868. https://doi.org/10.2151/jmsj1965.66.6_857

Hitchman, M. H., & Huesmann, A. S. (2007). A seasonal climatology of Rossby wave breaking in the 320-2000-K layer. *Journal of the Atmospheric Sciences*, **64**, 1922–1940.

Holton, J. R. (1975). The dynamic meteorology of the stratosphere and mesosphere. *Meteorological Monographs*, **15**(37), American Meteorological Society.

Ishii, M., Shouji, A., Sugimoto, S., and Matsumoto, T. (2005). Objective analyses of sea-surface temperature and marine meteorological variables for the 20th century using ICOADS and the Kobe collection. *Int. J. Climatol.*, **25**, 865–879.

Kao, S.-K., Jenne, R. L., & Sagendorf, J. F. (1970). The kinetic energy of the large-scale atmospheric motion in the wavenumber-frequency space: II. Mid-troposphere of the Southern Hemisphere. *Journal of the Atmospheric Sciences*, **27**, 1008–1020. https://doi.org/10.1175/1520-0469(1970)027<1008:TKEOLS>2.0.CO;2

Karoly, D. J. (1983). Rossby-wave propagation in a barotropic atmosphere. *Dynamics of Atmospheres and Oceans*, **7**(2), 111–125. https://doi.org/10.1016/0377-0265(83)90013-1

Kinoshita, T., & Sato, K. (2013a). A formulation of three-dimensional residual mean flow applicable both to inertia–gravity waves and to Rossby Waves. *Journal of the Atmospheric Sciences*, **70**, 1577–1602. https://doi.org/10.1175/JAS-D-12-0137.1

Kinoshita, T., & Sato, K. (2013b). A formulation of unified three-dimensional wave activity flux of inertia–gravity waves and Rossby waves. *Journal of the Atmospheric Sciences*,

70, 1603–1615. https://doi.org/10.1175/JAS-D-12-0138.1

Kobayashi, S., Ota, Y., Harada, Y., Ebita, A., Moriya, M., Onoda, H., Onogi, K., Kamahori, Kobayashi, C., Endo, H., Miyaoka, K., & Takahashi, K. (2015). The JRA-55 reanalysis: General specifications and basic characteristics. *Journal of the Meteorological Society of Japan*, **93**(1), 5–48. https://doi.org/10.2151/jmsj.2015-001

Krüger, K., Naujokat, B., & Labitzke, K. (2005). The unusual midwinter warming in the Southern Hemisphere stratosphere 2002: A comparison to Northern Hemisphere phenomena. *Journal of the Atmospheric Sciences*, **62**(3), 603–613. https://doi.org/10.1175/JAS-3316.1

Labitzke, K. (1965). On the mutual relation between stratosphere and troposphere during periods of stratospheric warmings in winter. *Journal of Applied Meteorology*, **4**(1), 91–99. https://doi.org/10.1175/1520-0450(1965)004<0091:OTMRBS>2.0.CO;2

Labitzke, K. (1977). Interannual variability of the winter stratosphere in the Northern Hemisphere. *Monthly Weather Review*, **105**(6), 762–770. https://doi.org/10.1175/1520-0493(1977)105<0762:IVOTWS>2.0.CO;2

Labitzke, K. (1978). On the different behavior of the zonal harmonic height waves 1 and 2 during the winters 1970/71 and 1971/72. *Monthly Weather Review*, **106**(12), 1704–1713. https://doi.org/10.1175/1520-0493(1978)106<1704:OTDBOT>2.0.CO;2

Labitzke, K., & van Loon, H. (1999). The stratosphere (p. 179). *Berlin Heidelberg: Springer-Verlag*. https://doi.org/10.1007/978-3-642-58541-8

Martius, O., Polvani, L. M., & Davies, H. C. (2009). Blocking precursors to stratospheric

sudden warming events. *Geophysical Research Letters*, **36**, L14806. https://doi.org/10.1029/2009GL038776

Matsuno, T., & Hirota, I. (1966). On the dynamical stability of polar vortex in wintertime. *Journal of the Meteorological Society of Japan*, **44**, 122–128. https://doi.org/10.2151/jmsj1965.44.2_122

Miles, T., & Grose, W. L. (1986). Transient medium-scale wave activity in the summer stratosphere. *Bulletin of the American Meteorological Society*, **67**, 674–686. https://doi.org/10.1175/1520-0477(1986)067<0674:TMSWAI>2.0.CO;2

Mitchell, D. M., Gray, L. J., Anstey, J., Baldwin, M. P., & Charlton, A. J. (2013). The influence of stratospheric vortex displacements and splits on surface climate. *Journal of Climate*, **26**(8), 2668–2682. https://doi.org/10.1175/JCLI-D-12-00030.1

Mukougawa, H., Sakai, H., & Hirooka, T. (2005). High sensitivity to the initial condition for the prediction of stratospheric sudden warming. *Geophysical Research Letters*, **32**, L17806. https://doi.org/10.1029/2005GL022909

Mukougawa, H., Noguchi, S., Kuroda, Y., Mizuta, R. & Kodera, K. (2017). Dynamics and predictability of downward-propagating stratospheric planetary waves observed in March 2007. *Journal of the Atmospheric Sciences*, **74**, 3533-3550. https://doi.org/ 10.1175/JAS-D-16-0330.1

Naoe, H., Matsuda, Y., & Nakamura, H. (1997). Rossby wave propagation in idealized and realistic zonally varying flows. *Journal of the Meteorological Society of Japan*, **75**(3), 687–700.

Nishii, K., & Nakamura, H. (2004). Lower-stratospheric Rossby wave trains in the Southern Hemisphere: A case study for late winter of 1997. *Quarterly Journal of the Royal Meteorological Society*, **130**(596), 325–345. https://doi.org/10.1256/qj.02.156

Nishii, K., Nakamura, H., & Orsolini, Y. J. (2011). Geographical dependence observed in blocking high influence on the stratospheric variability through enhancement and suppression of upward planetary-wave propagation. *Journal of Climate*, **24**(24), 6408–6423. https://doi.org/10.1175/JCLI-D-10-05021.1

O'Neill, A., & Taylor, B. F. (1979). A study of the major stratospheric warming of 1976/77. *Quarterly Journal of the Royal Meteorological Society*, **105**(443), 71–92. https://doi.org/10.1002/qj.49710544306

Orsolini, Y. J., Urban, J., Murtagh, D. P., Lossow, S., & Limpasuvan, V. (2010). Descent from the polar mesosphere and anomalously high stratopause observed in 8 years of water vapor and temperature satellite observations by the Odin Sub-Millimeter Radiometer, *Journal of Geophysical Research*, **115**, D12305. https://doi.org/10.1029/2009JD013501

Pfister, L. (1979). A Theoretical Study of Three-Dimensional Barotropic Instability with Applications to the Upper Stratosphere. *Journal of the Atmospheric Sciences*, **36**, 908–920. https://doi.org/10.1175/1520-0469(1979)036<0908:ATSOTD>2.0.CO;2

Plumb, R. A. (1985). On the three dimensional propagation of stationary waves. *Journal of the Atmospheric Sciences*, **42**(3), 217–229. https://doi.org/10.1175/1520-0469(1985)042%3C0217:OTTDPO%3E2.0.CO;2

Quiroz, R. S. (1986). The association of stratospheric warmings with tropospheric blocking. *Journal of Geophysical Research*, **91**(D4), 5277–5285. https://doi.org/10.1029/JD091iD04p05277

Randel, W. J., & Stanford, J. L. (1985). An observational study of medium-scale wave dynamics in the Southern Hemisphere summer. Part I: Wave structure and energetics. *Journal of the Atmospheric Sciences*, **42**, 1172–1188. https://doi.org/10.1175/1520-0469(1985)042<1172:AOSOMS>2.0.CO;2

Sato, K., Yamada, K. & Hirota, I. (2000). Global characteristic of medium-scale waves observed in ECMWF operational data. *Mon. Weather Rev.*, **128**, 3808–3823. https://doi.org/10.1175/1520-0493(2001)129<3808:GCOMST>2.0.CO;2

Sato, K., Kinoshita, T., & Okamoto, K. (2013). A new method to estimate three-dimensional residual-mean circulation in the middle atmosphere and its application to gravity wave–resolving general circulation model data. *Journal of the Atmospheric Sciences*, **70**, 3750–3779. https://doi.org/10.1175/JAS-D-12-0352.1

Taguchi, M., & Hartmann, D. L. (2006). Increased occurrence of stratospheric sudden warmings during El Niño simulated by WACCM. *Journal of Climate*, **19**(3), 324–332. https://doi.org/10.1175/JCLI3655.1

Tomikawa, Y., & Sato, K. (2003). Trapped waves in the edge region of stratospheric polar vortices. *Journal of Geophysical Research*, **108**(D2), 4047. https://doi.org/10.1029/2002JD002579

WMO (1978). Abridged final report of the seventh session of the Commission for

Atmospheric Sciences. WMO Rep. 509, 113 pp.

Yu, B., & Zhang, X. (2015). A physical analysis of the severe 2013/2014 cold winter in North America. *Journal of Geophysical Research: Atmospheres*, **120**, 10,149–10,165. https://doi.org/10.1002/2015JD023116

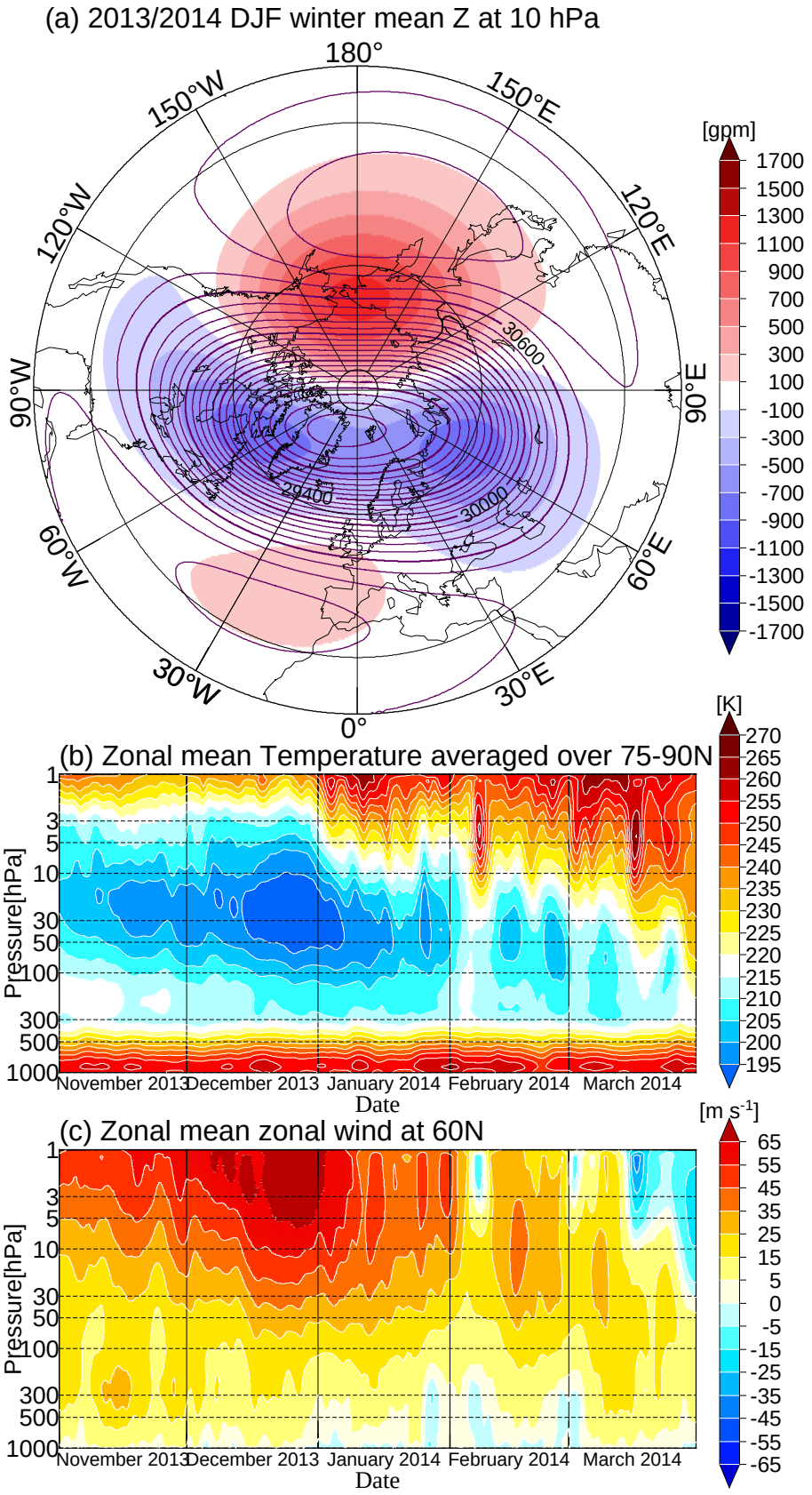

Figure 4-1. (a) 2013/2014 winter (DJF) mean 10-hPa geopotential heights (contours) and deviations from the zonal mean (shading) in the Northern Hemisphere. Time-pressure cross sections of (b) zonal-mean temperatures averaged 75°-90°N and (c) zonal-mean zonal wind at 60°N during the winter 2013/2014. For the units and the shading, see each tone bar.

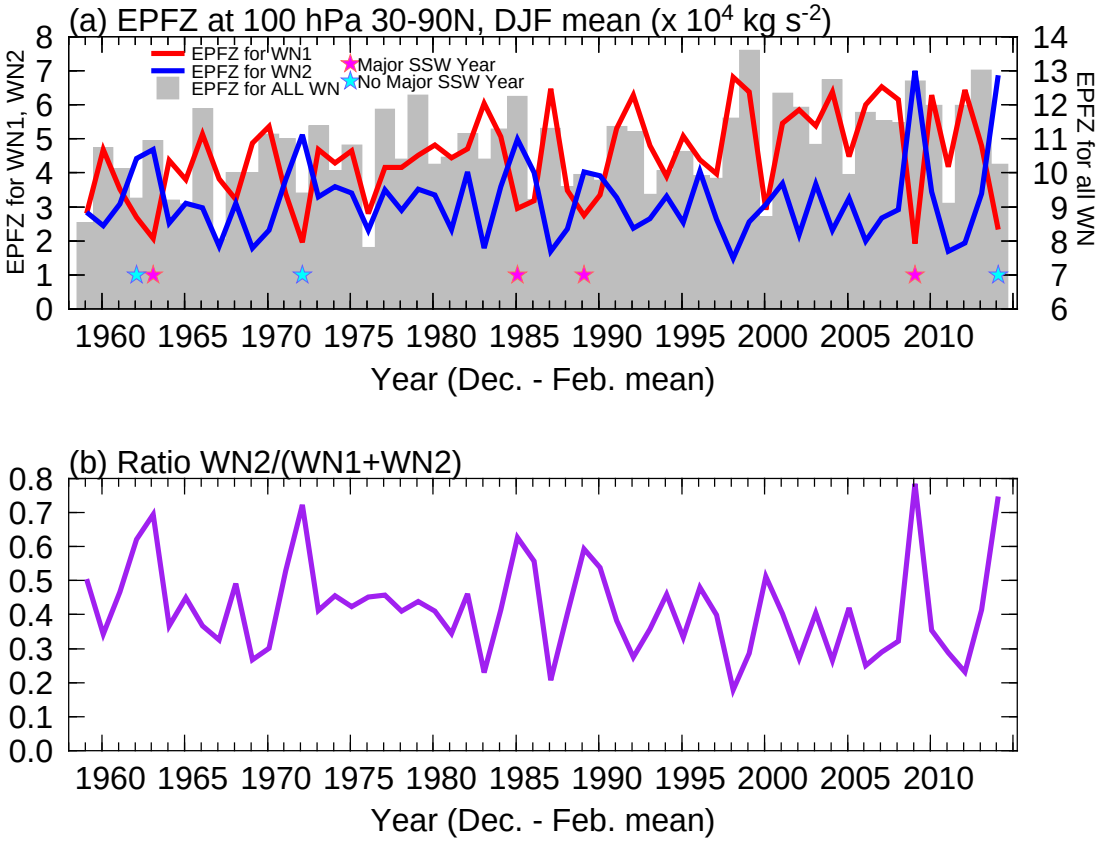

Figure 4-2. (a) Inter-annual variations in upward EP fluxes ($\times 10^4$ kg s^{-2}) at 100 hPa averaged over 30°-90°N in boreal winters (DJF) for WN1 (red line), WN2 (blue line), and all wavenumbers (gray bars) and (b) the ratio of WN2 to the sum of WN1 and WN2 (purple line). Stars in (a) indicate that ratios in (b) are 0.6 or more (for seven winters: 1961/1962, 1962/1963, 1971/1972, 1984/1985, 1988/1989, 2008/2009, and 2013/2014). Pink and light blue stars in (a) correspond to two cases: one is that a major SSW occurred during the winter and the other is that no major SSW occurred during the winter.

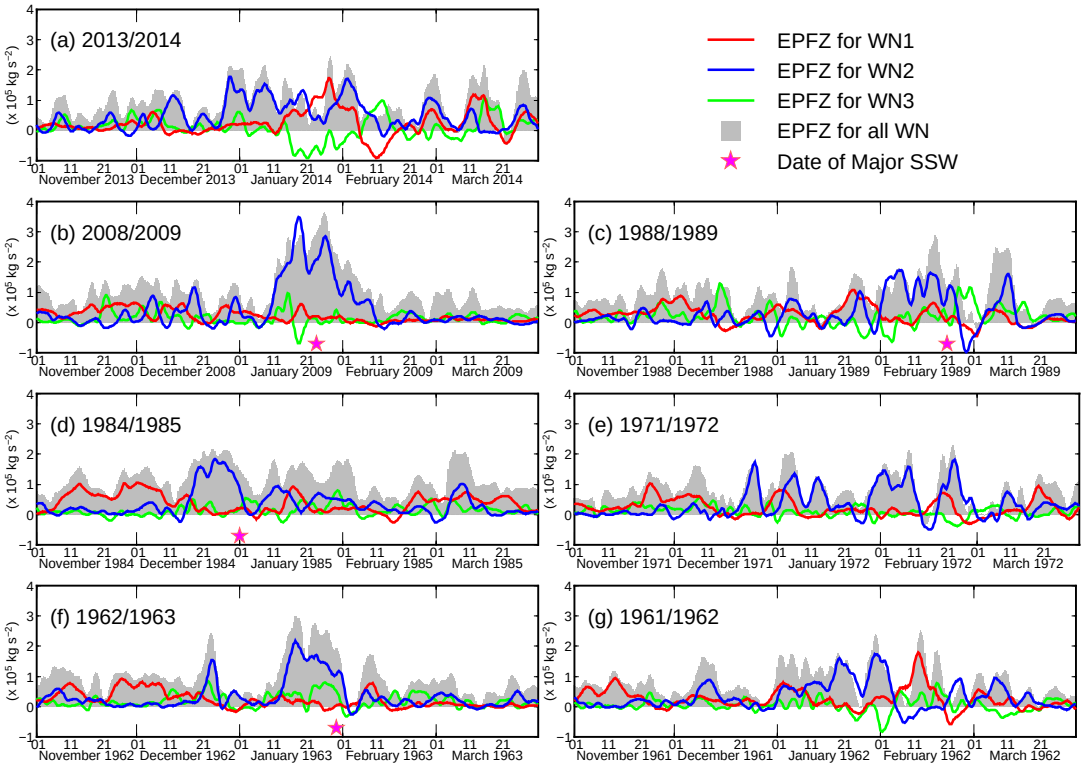

Figure 4−3. Time series of EPFz ($\times 10^5$ kg s^{-2}) averaged over 30°−90°N at 100 hPa in the winters of (a) 2013/2014, (b) 2008/2009, (c) 1988/1989, (d) 1984/1985, (e) 1971/1972, (f) 1962/1963, and (g) 1961/1962. EPFz of waves 1, 2, and 3 are denoted by red, blue, and light green lines, respectively. Gray shadings represents EPFz of all wavenumbers. Pink stars indicate the onset dates of major SSW.

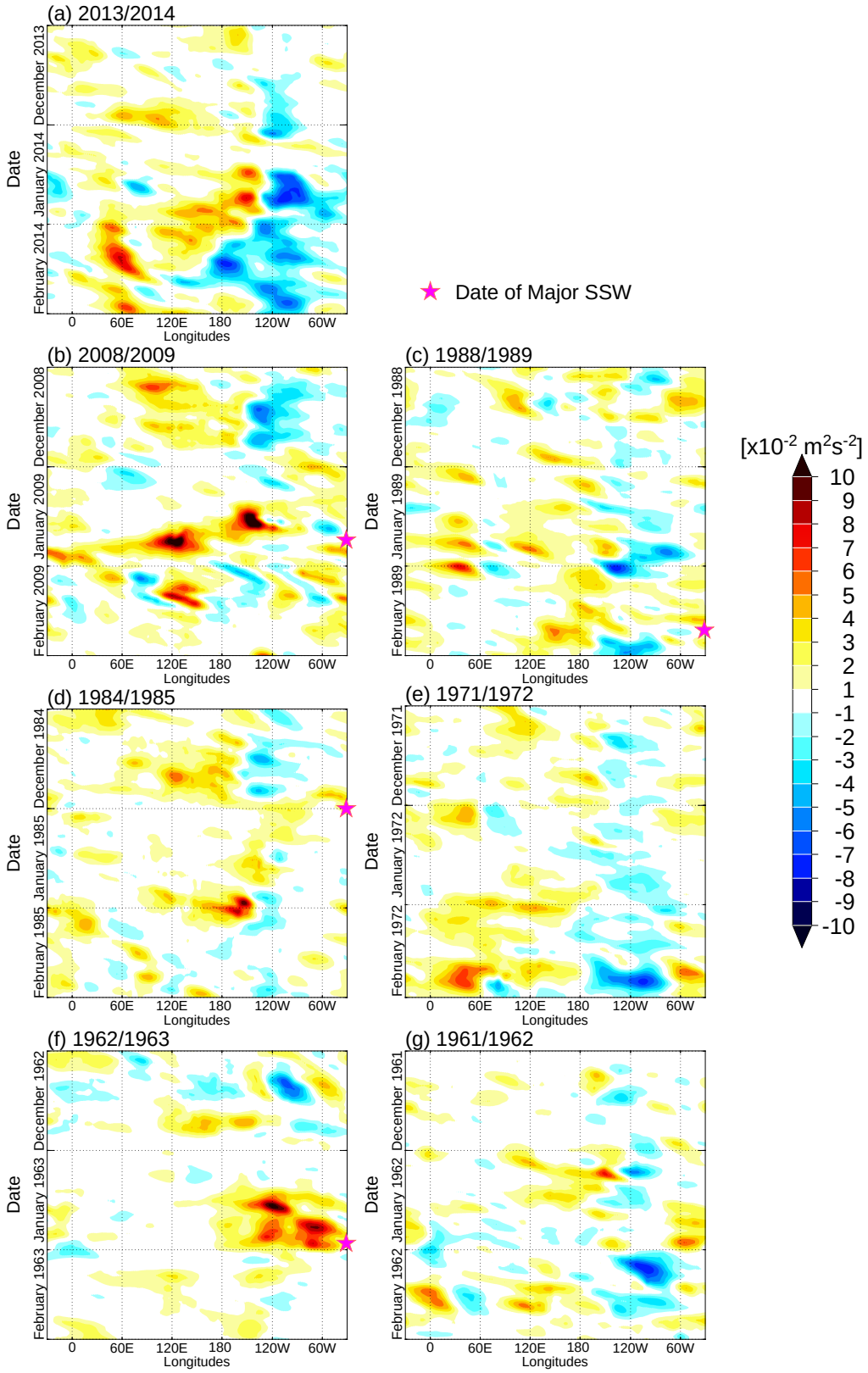

Figure 4-4. As in Figure 4-3, but for longitude-time cross sections of Plumb WAFz averaged over 30°-90°N at 100 hPa. For the units and the color shading, see the tone bar. Pink stars indicate the onset dates of major SSW.

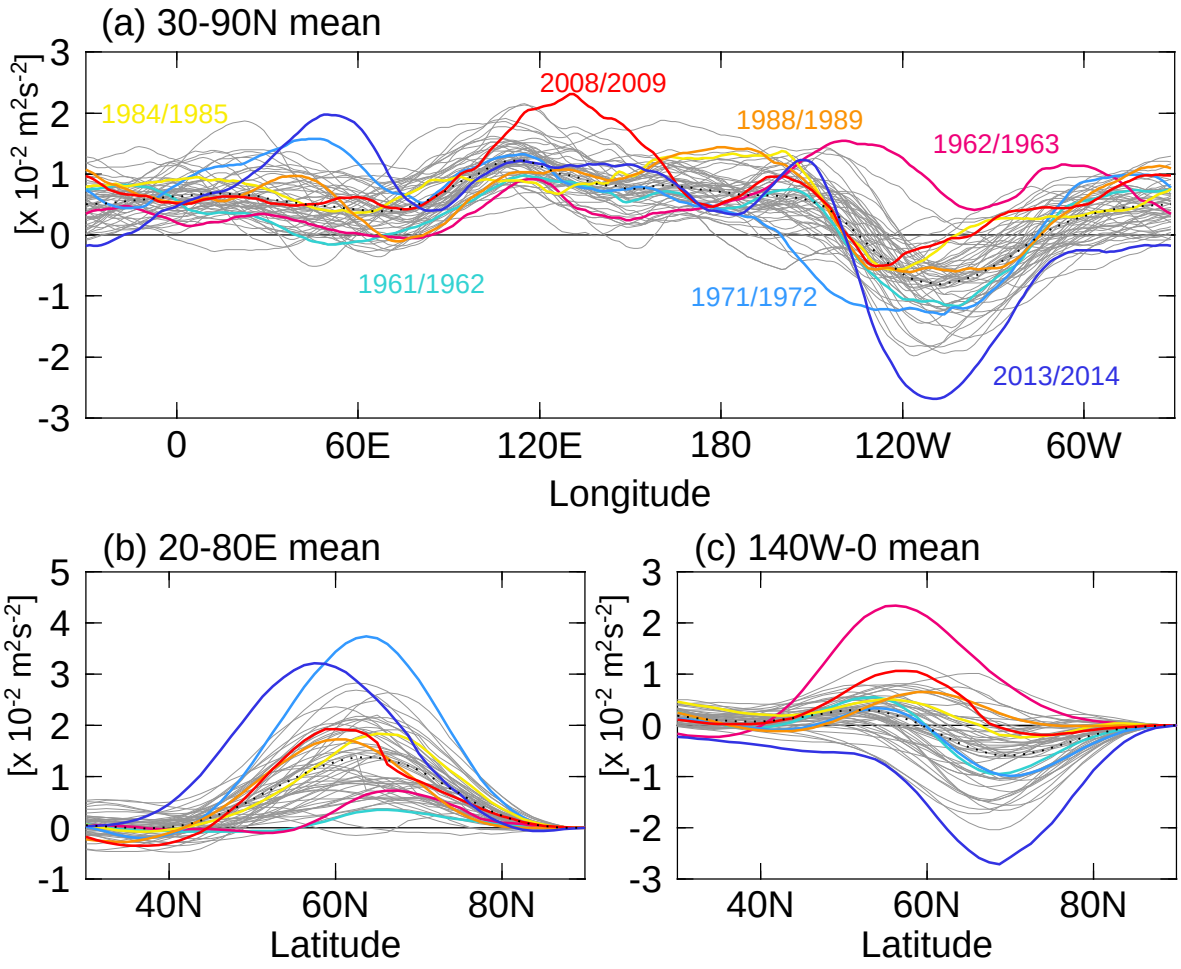

Figure 4-5. (a) Longitudinal distributions of winter-mean WAFz averaged over 30°-90°N at 100 hPa. (b), (c) Latitudinal distributions of winter-mean WAFz at 100 hPa averaged over 20°-80°E, 140W-0°, respectively. Thick blue, light blue, red, and orange lines represent the winters of 2013/2014, 1971/1972, 2008/2009, and 1962/1963, respectively (Warm and cold colors correspond to WN2_MSSW and WN2_noMSSW winters, respectively).

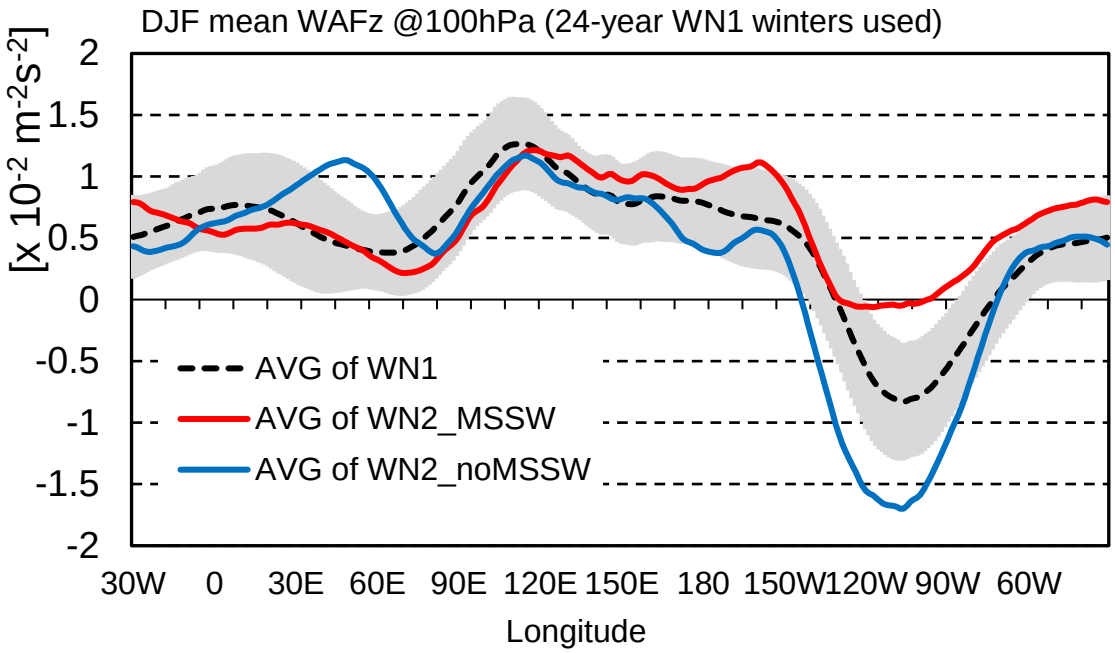

Figure 4-6. As in Figure 4-5a, but for the average of WN1 winters (black dotted line), WN2 winters with major SSWs (red line), and WN2 winters with no major SSW (blue line), respectively. Gray shading shows standard deviations ranges of WN1 winters. WN1 winters are selected base on the critical ratio of 0.6 of the WN1 contribution to the sum of WN1 and WN2.

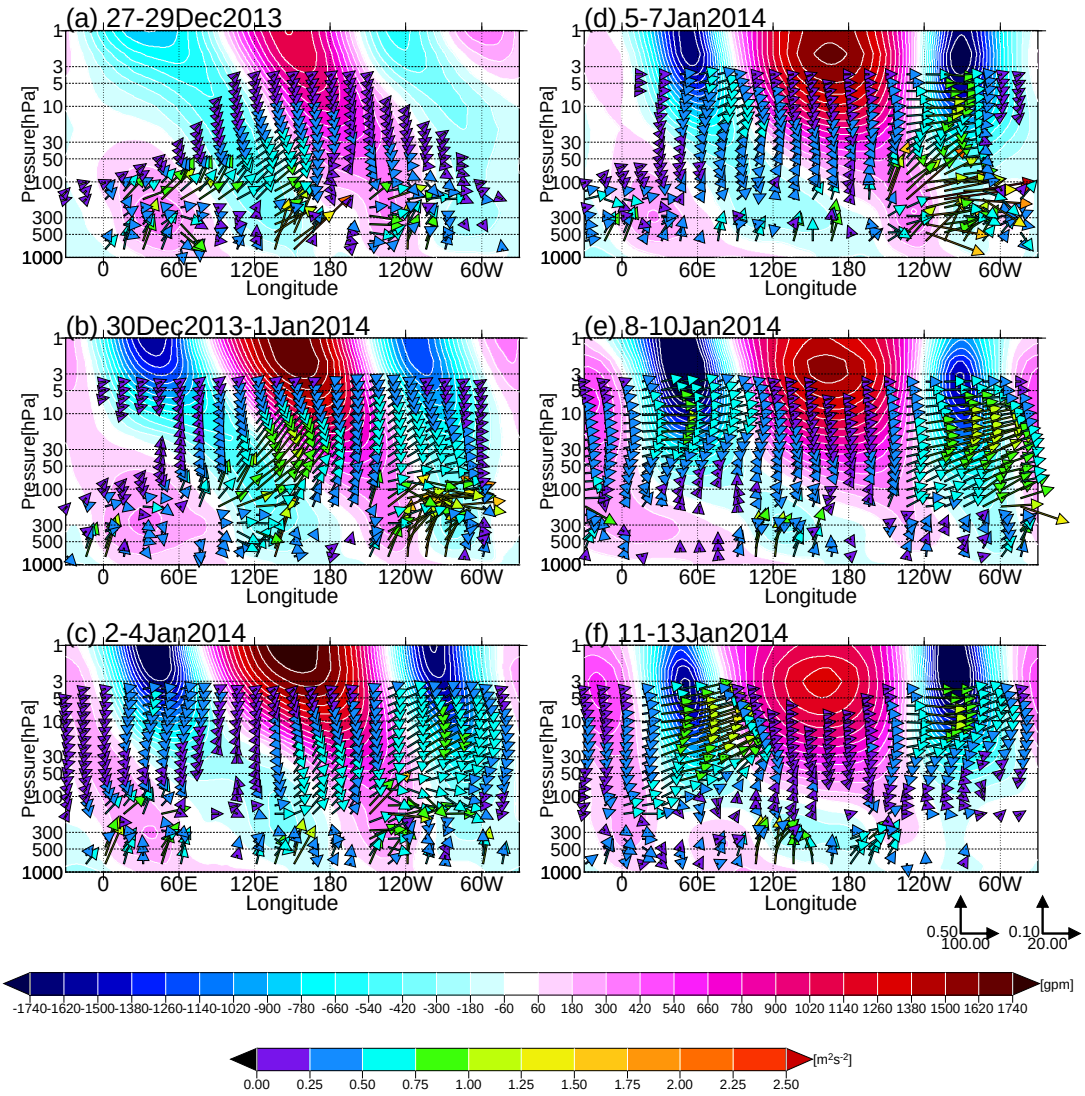

Figure 4-7. Longitude-height cross sections of geopotential height deviations from the zonal mean (shading) and WAFs (vectors) averaged over 45°-65°N for successive 3-day means. WAFs are in units of $m^2\ s^{-2}$. The vector scales at the lower right corner of the panels denote vectors below and above 70 hPa, respectively. The color scale for the vector (rightmost tone bar) corresponds to the amplitudes of the WAF in the figure space. For example, above 70 hPa, the amplitude of vector represents $\sqrt{(WAFx/20.00)^2+(WAFz/0.10)^2}$. For the shading, see the tone bar (the lowest one). Dates are (a) December 27-29, 2013; (b) December 30, 2013 -January 1, 2014; (c) January 2-4, 2014; (d) January 5-7, 2014; (e) January 8-10, 2014; and (f) January 11-13, 2014.

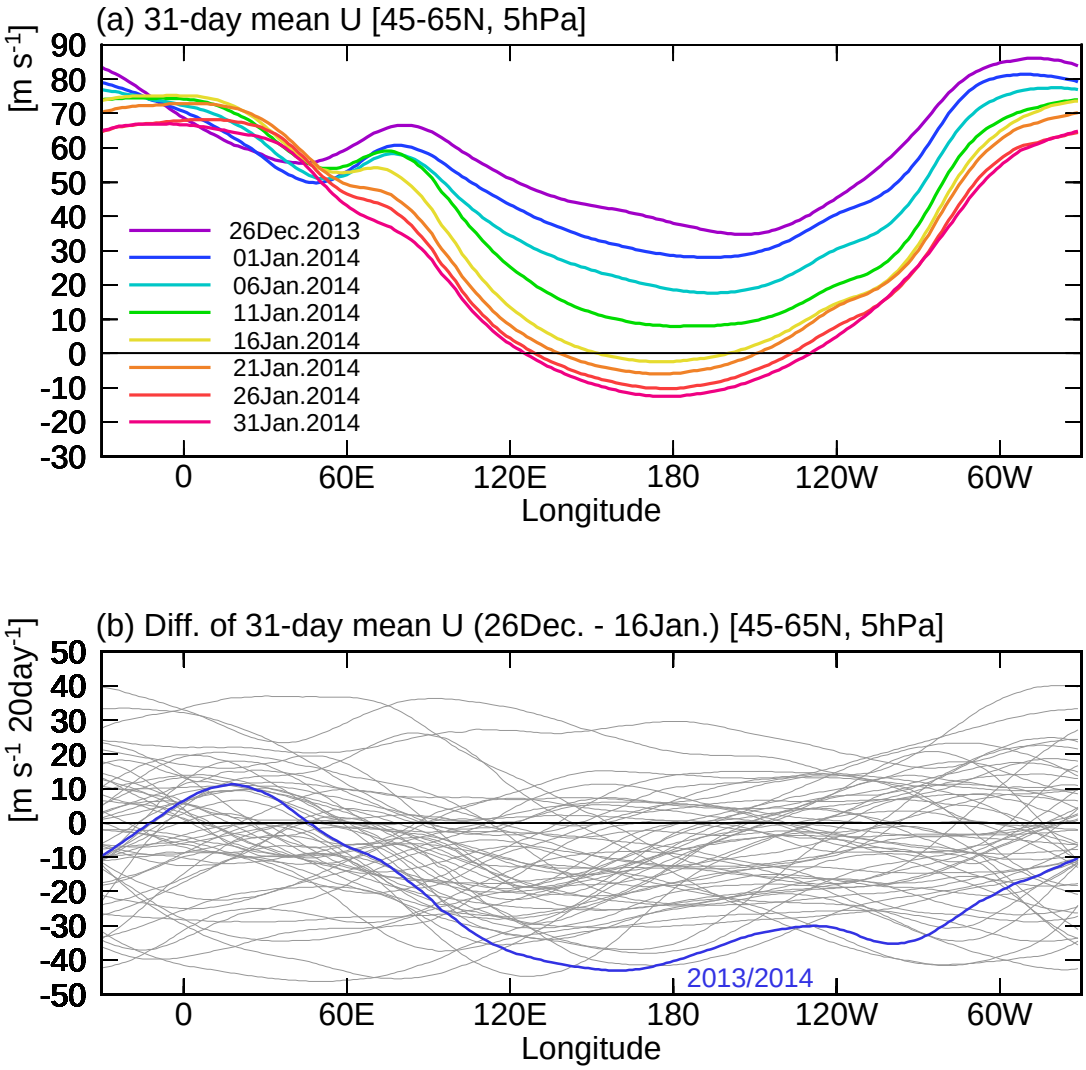

Figure 4-8. Longitudinal distribution of (a) 31-day-mean zonal winds (m s^{-1}) averaged over 45°-65°N at the 5 hPa level and (b) differences in 31-day-mean zonal winds averaged over 45°-65°N at the 5 hPa level between December 26 and January 16 for the winters since 1958/1959 (m s^{-1} 20-$days^{-1}$).

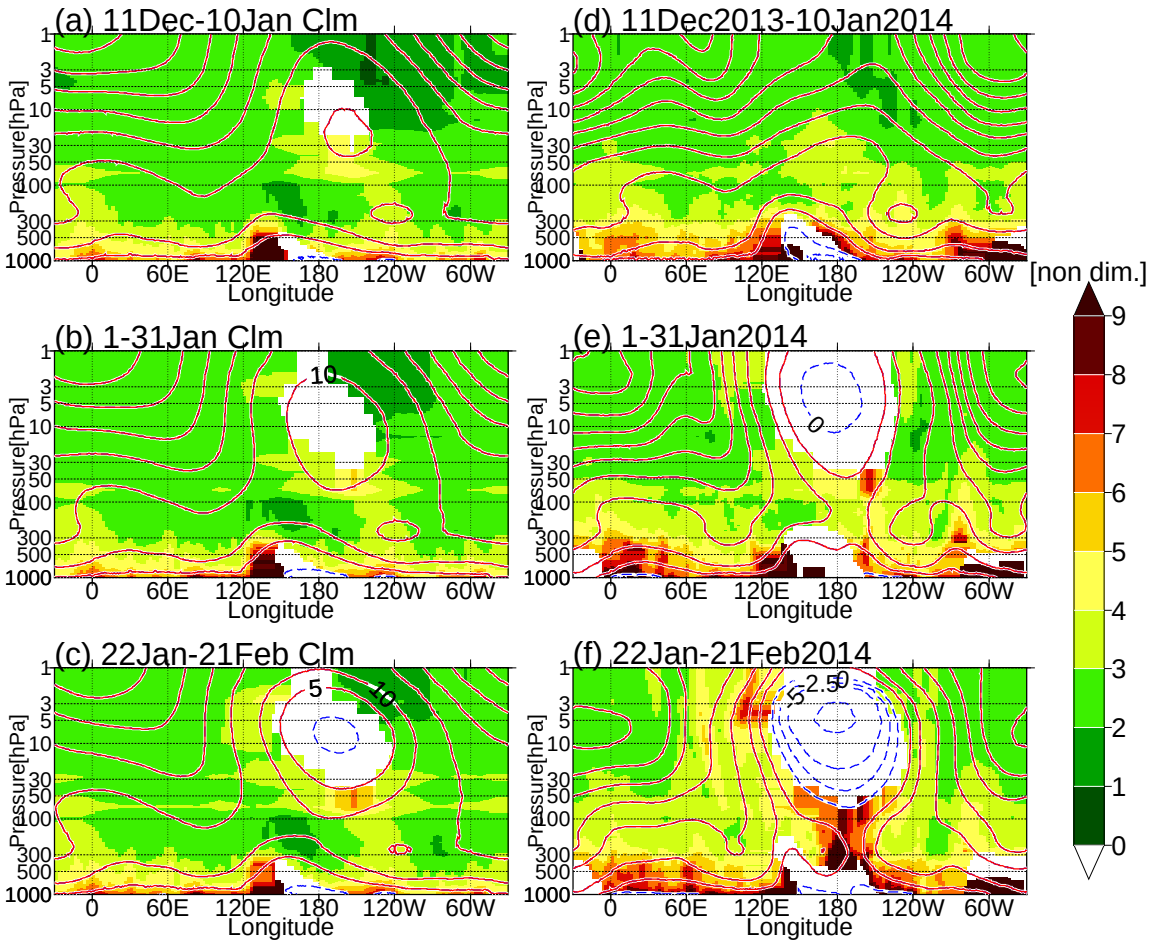

Figure 4-9. Longitude-height cross sections of (shading) Ks and (contour) zonal winds (m s^{-1}) averaged over 45°-65°N for successive 31-day-means. Left and right panels represent for the climatological mean field (1980/81-2009/2010) and for the winter 2013/2014, respectively. The white blank regions indicate that planetary waves are not able to propagate. The extended refractive index is shown as the equivalent zonal wavenumber for this latitude circle (non-dimensional value). For the shading, see the tone bar. For the contour, the red and blue-dashed lines represents westerly and easterly winds, respectively. Contour interval of the red line is 5 m s^{-1} for values below 10 m s^{-1} and is 10 m s^{-1} for values exceed 10 m s^{-1}. Contour interval of the blue line is 2.5 m s^{-1}.

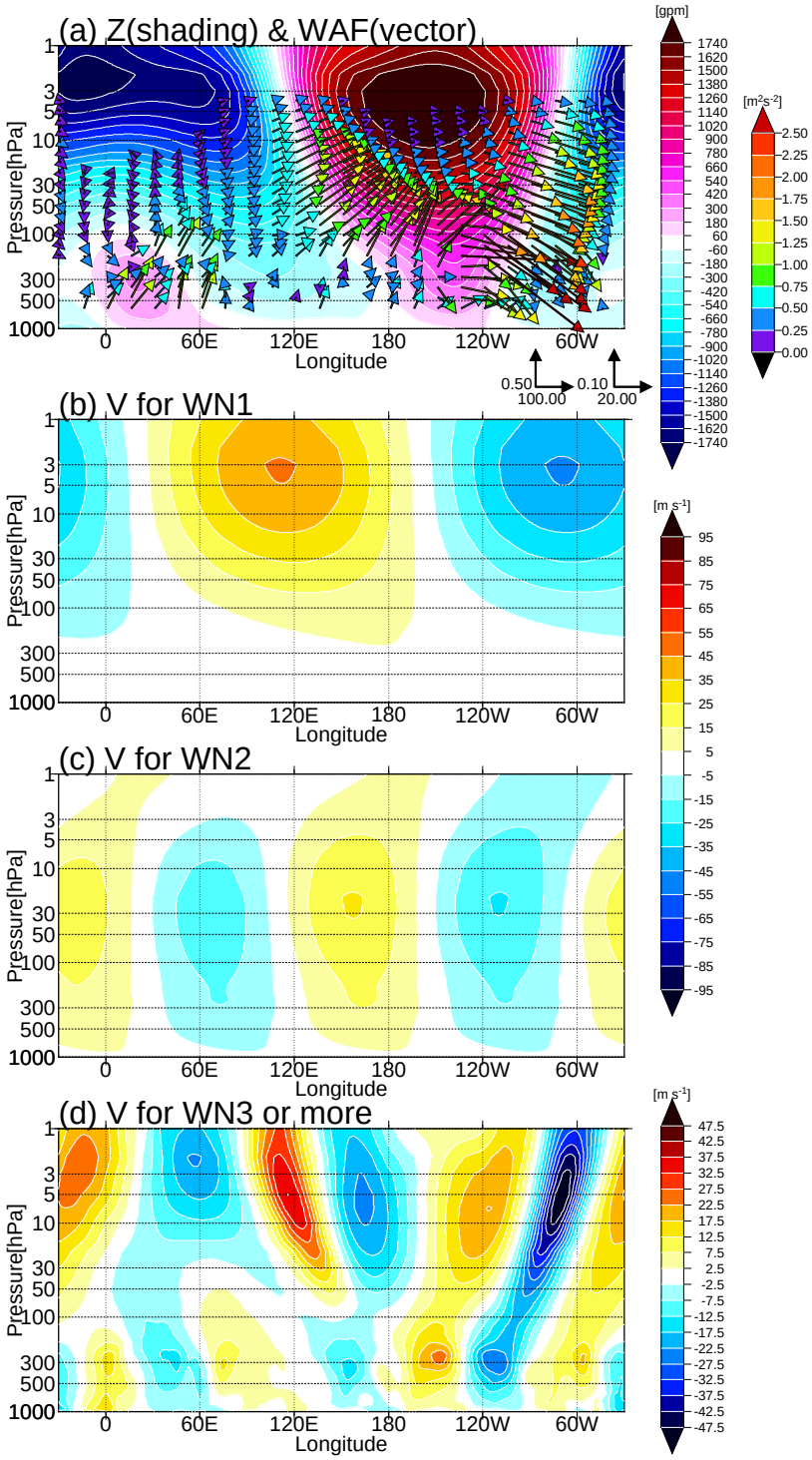

Figure 4-10. Longitude-height cross sections of (a) geopotential height deviations from the zonal mean (shadings) and Plumb wave activity fluxes (vectors), Lanczos filtered meridional wind for (b) zonal wave number one, (c) zonal wave number two, and (e) zonal wave number three or more averaged over 65°-69°N during January 23-25, 2014. Plumb wave activity flux vectors are in units of m^2s^{-2}. The vector scales at the lower right corner of the panels denote vectors below and above 70 hPa, respectively. The color scale for the vector (rightmost tone bar in (a)) corresponds to the amplitudes of the WAF in the figure space. For example, above 70 hPa, the amplitude of vector represents $\sqrt{(WAFx/20.00)^2+(WAFz/0.10)^2}$. For the units and the shading, see each tone bar.

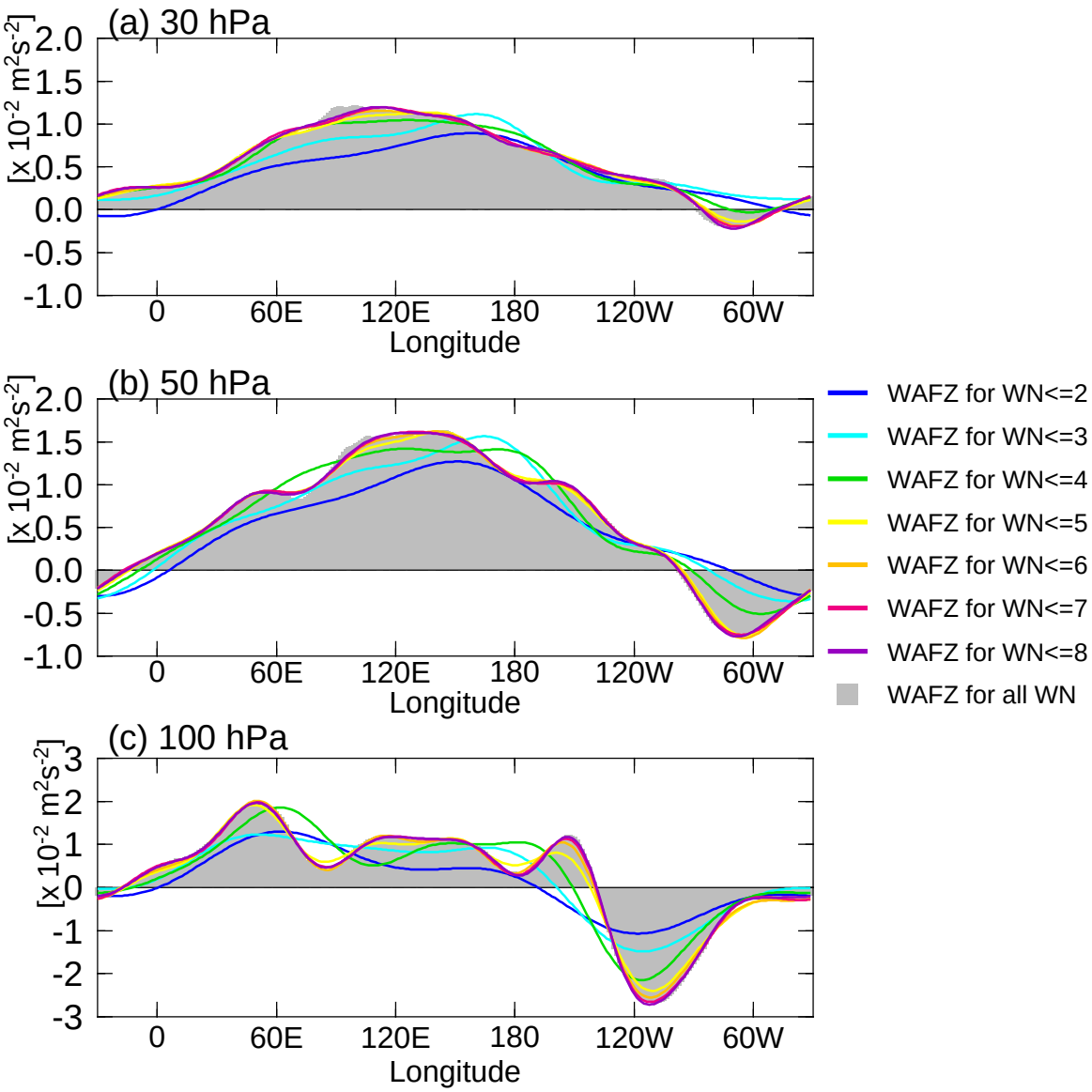

Figure 4-11. Longitudinal distribution of WAFz averaged over 30°-90°N for various zonal wave number ranges at (a) 30 hPa, (b) 50 hPa, and (c) 100 hPa. These are seasonal means of WAFz values calculated from the 3-day mean field during the winter 2013/2014. Shadings represent the WAFz for all wave numbers. WAFz values are in units of m^2s^{-2}.

Table 5-1

Lag Correlations Between daily 250VVAR and EPFz at 5, 10, 30, and 100 hPa levels

	Lag days of EPFz	0 day	+1 day	+2 days	+3 days	+4 days	+5 days
				5 hPa EPFz			
	All WN	0.09	0.10	0.10	0.11	0.10	0.09
250VVAR	WN1	0.09	0.12	0.13	0.15	0.15	0.15
	WN2	0.23	0.26	0.28	0.29	0.29	0.28
				10 hPa EPFz			
	All WN	0.10	0.11	0.12	0.13	0.13	0.11
250VVAR	WN1	0.09	0.12	0.14	0.16	0.16	0.16
	WN2	0.28	0.31	0.33	0.35	0.34	0.32
				30 hPa EPFz			
	All WN	0.12	0.13	0.14	0.15	0.14	0.13
250VVAR	WN1	0.12	0.15	0.17	0.18	0.18	0.17
	WN2	0.39	0.42	0.43	0.35	0.39	0.35
				100 hPa EPFz			
	All WN	0.19	0.21	0.21	0.19	0.16	0.13
250VVAR	WN1	0.20	0.22	0.22	0.21	0.19	0.17
	WN2	0.48	0.49	0.47	0.42	0.36	0.29

Table 5-2

Tropospheric WN2 Amplification Events[a] Identiflied in the JRA-55 Data Set

SU_30EPFz[b]

Number	Central Date	Start Date	End Date	Num. of Days
1	17 January 1963	22 December 1962	26 January 1963	12
2	20 December 1964	20 December 1964	21 December 1964	2
3	23 February 1972	20 February 1972	24 February 1972	5
4	21 February 1979	17 February 1979	22 February 1979	6
5	19 January 1982	16 January 1982	22 January 1982	7
6	23 December 1983	21 December 1983	23 December 1983	3
7	27 December 1984	22 December 1984	29 December 1984	8
8	13 February 1989	4 February 1989	20 February 1989	12
9	15 January 1996	14 January 1996	15 January 1996	2
10	15 January 2000	14 January 2000	15 January 2000	2
11	18 January 2009	14 January 2009	24 January 2009	11
12	09 December 2009	9 December 2009	12 December 2009	4
13	28 December 2013	27 December 2013	3 January 2014	6
14	01 January 2015	30 December 2014	3 January 2015	5
15	04 February 2018	4 February 2018	12 February 2018	9

WU_30EPFz[c]

Number	Central Date	Start Date	End Date	Num. of Days
1	03 February 1959	02 February 1959	10 February 1959	9
2	30 January 1963	30 January 1963	30 January 1963	1
3	18 February 1965	18 February 1965	18 February 1965	1
4	29 January 1972	29 January 1972	29 January 1972	1
5	05 January 1974	05 January 1974	08 January 1974	4
6	06 February 1975	06 February 1975	07 February 1975	2
7	09 January 1980	09 January 1980	10 January 1980	2
8	14 February 1986	12 February 1986	15 February 1986	3
9	24 January 1991	23 January 1991	26 January 1991	4
10	28 February 1991	28 February 1991	28 February 1991	1
11	26 December 1992	25 December 1992	26 December 1992	2
12	14 February 1994	14 February 1994	14 February 1994	1
13	05 December 2002	05 December 2002	05 December 2002	1
14	09 February 2003	08 February 2003	12 February 2003	5
15	16 December 2008	16 December 2008	18 December 2008	3

SD_30EPFz[d]

Number	Central Date	Start Date	End Date	Num. of Days
1	21 February 1965	21 February 1965	23 February 1965	3
2	13 December 1972	13 December 1972	13 December 1972	1
3	04 December 1977	03 December 1977	4 December 1977	2
4	06 January 1979	05 January 1979	6 January 1979	2
5	29 December 1982	29 December 1982	29 December 1982	1
6	21 February 1986	18 February 1986	23 February 1986	6
7	19 December 1990	19 December 1990	20 December 1990	2
8	20 February 1994	20 February 1994	23 February 1994	4
9	29 February 1996	29 February 1996	29 February 1996	1
10	15 December 2007	13 December 2007	15 December 2007	3
11	18 January 2008	18 January 2008	18 January 2008	1
12	24 December 2008	24 December 2008	24 December 2008	1
13	24 January 2010	22 January 2010	24 January 2010	3
14	08 February 2012	06 February 2012	9 February 2012	4
15	27 January 2014	23 January 2014	27 January 2014	5

WD_30EPFz[e]

Number	Central Date	Start Date	End Date	Num. of Days
1	13 February 1959	13 February 1959	16 February 1959	4
2	20 January 1961	20 January 1961	20 January 1961	1
3	18 December 1961	16 December 1961	20 December 1961	5
4	25 February 1962	25 February 1962	26 February 1962	2
5	20 February 1965	20 February 1965	20 February 1965	1
6	02 January 1974	02 January 1974	02 January 1974	1
7	28 February 1978	28 February 1978	28 February 1978	1
8	12 January 1980	12 January 1980	12 January 1980	1
9	17 February 1986	17 February 1986	17 February 1986	1
10	26 February 1991	26 February 1991	26 February 1991	1
11	13 February 1993	13 February 1993	14 February 1993	2
12	21 January 1995	21 January 1995	21 January 1995	1
13	31 December 1996	31 December 1996	31 December 1996	1
14	28 February 2011	28 February 2011	28 February 2011	1
15	04 February 2017	04 February 2017	06 February 2017	3

[a] Tropospheric WN2 amplification events are identified when normalized 250VVAR$_{_WN2}$ anomalies are more than 1 SD. If interval between two samples is 25 days or less, these are regarded as the same event. The central dates are the peak of tropospheric WN2 amplification during each event.

[b] SU_30EPFz events are extracted as the cases that normalized 30EPFz$_{_WN2}$ anomalies are more than 2.8 SD two days after the peak of tropospheric WN2 amplification.

[c] WU_30EPFz events are extracted as the cases that normalized 250VVAR$_{_WN2}$ anomalies are more than 2.5 SD and normalized 30EPFz$_{_WN2}$ anomalies (two days after the peak of tropospheric WN2 amplification) are 1.0 SD or less.

[d] SD_30EPFz enets are extracted as the cases that normalized 30EPFz$_{_WN2}$ anomalies are less than -0.87 SD two days after the peak of tropospheric WN2 amplification.

[e] WD_30EPFz events are extracted as the cases that normalized 250VVAR$_{_WN2}$ anomalies are more than 2.0 SD and normalized 30EPFz$_{_WN2}$ anomalies (two days after the peak of tropospheric WN2 amplification) are between -0.83 SD and -0.35 SD.

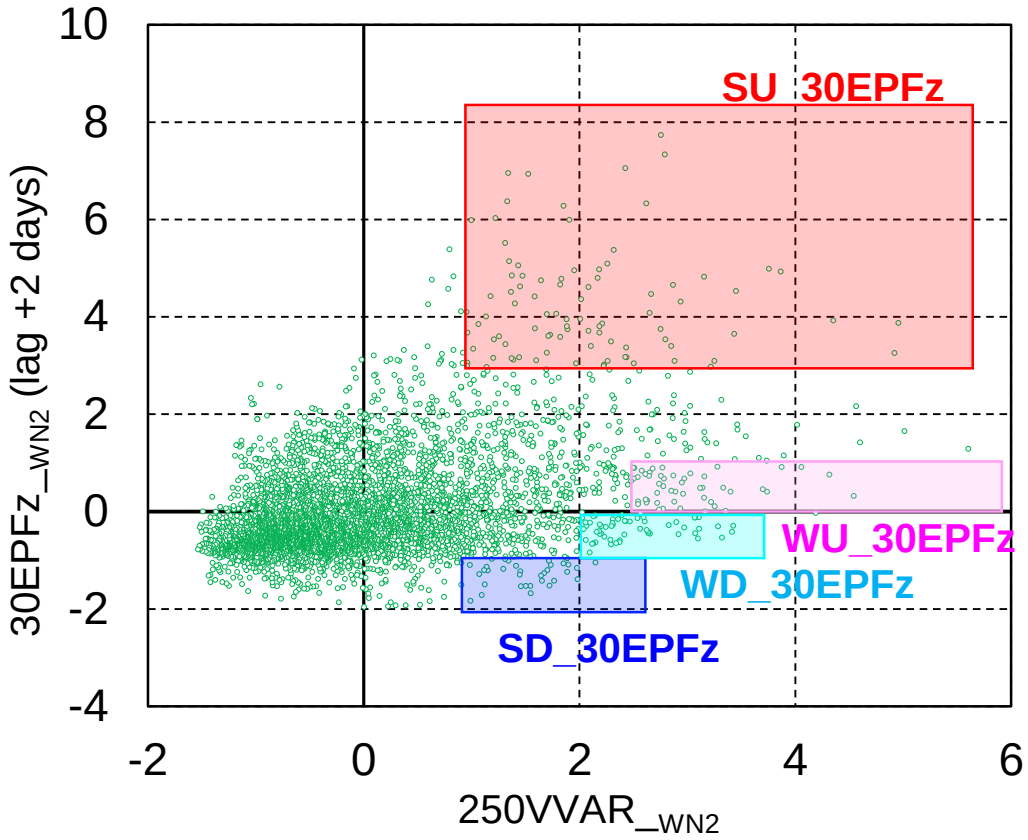

Figure 5-1. Scattered diagram between normalized 250VVAR_WN2 anomalies and normalized 30EPFz_WN2 anomalies two days after the WN2AUT peaks.

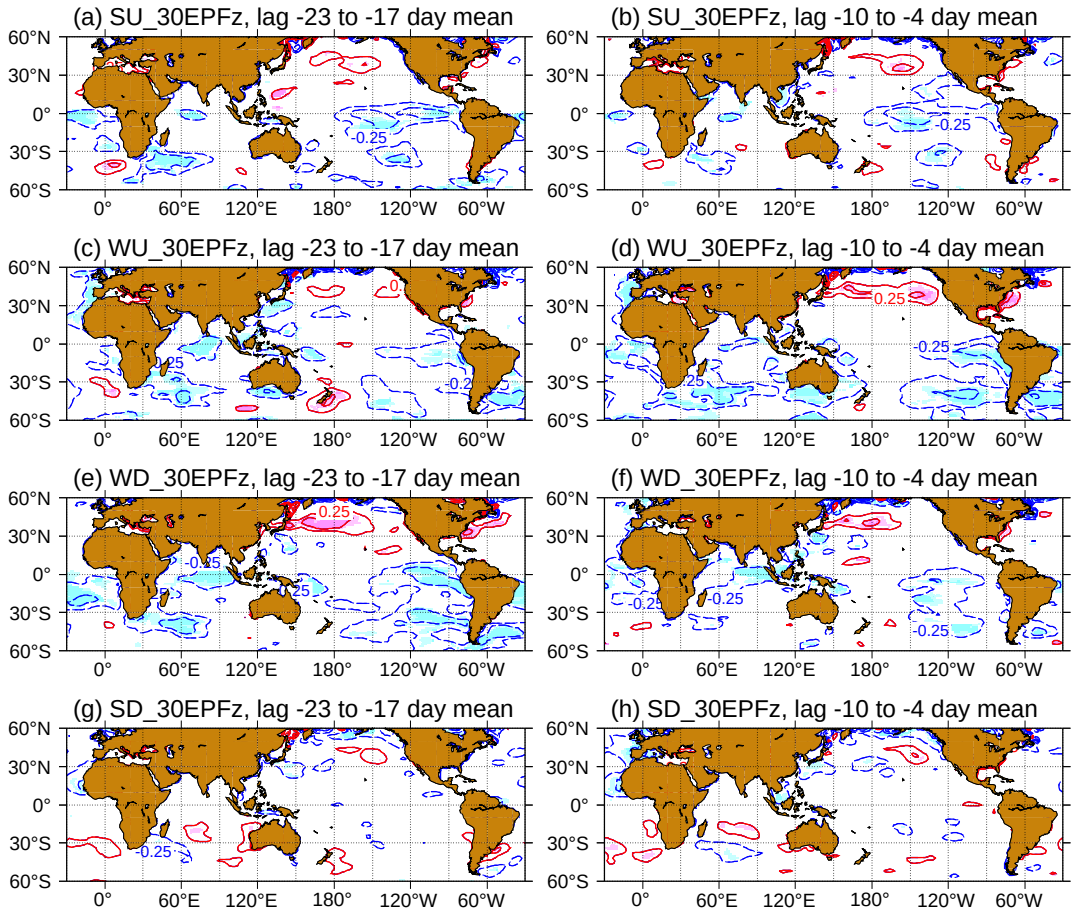

Figure 5-2. Lag composite maps of seven days mean SST anomalies (contours) before the WN2AUT peak among (a),(b) SU_30EPFz, (c),(d) WU_30EPFz, (e),(f) WD_30EPFz and (g),(h) SD_30EPFz. Left (Right) panels are for the period of 23-17 (10-4) day before the WN2AUT peak. Contour interval is 0.5 K. Light and dark Shadings show areas with statistical confidence above 90% and 95%, respectively.

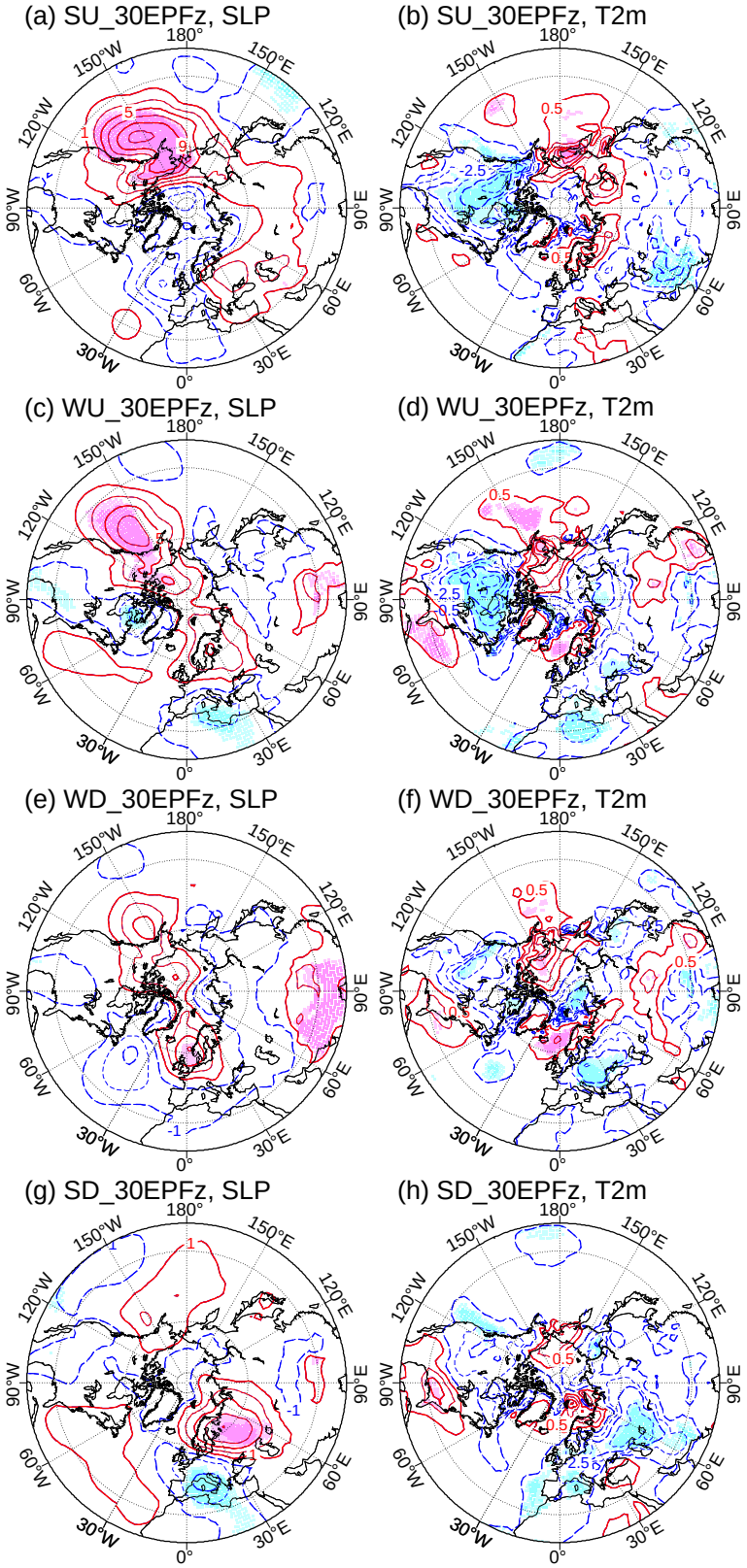

Figure 5-3. As in Figure 5-2 but left and right panels respectively show SLP anomalies (contours) from ten days to four days and 2-m temperature anomalies (contours) from seven days to one day before the WN2AUT peak during (a),(b) SU_30EPFz, (c),(d) WU_30EPFz, (e),(f) WD_30EPFz and (g),(h) SD_30EPFz. Contour intervals are 3 hPa for SLP and 1 K for 2-m temperature, respectively.

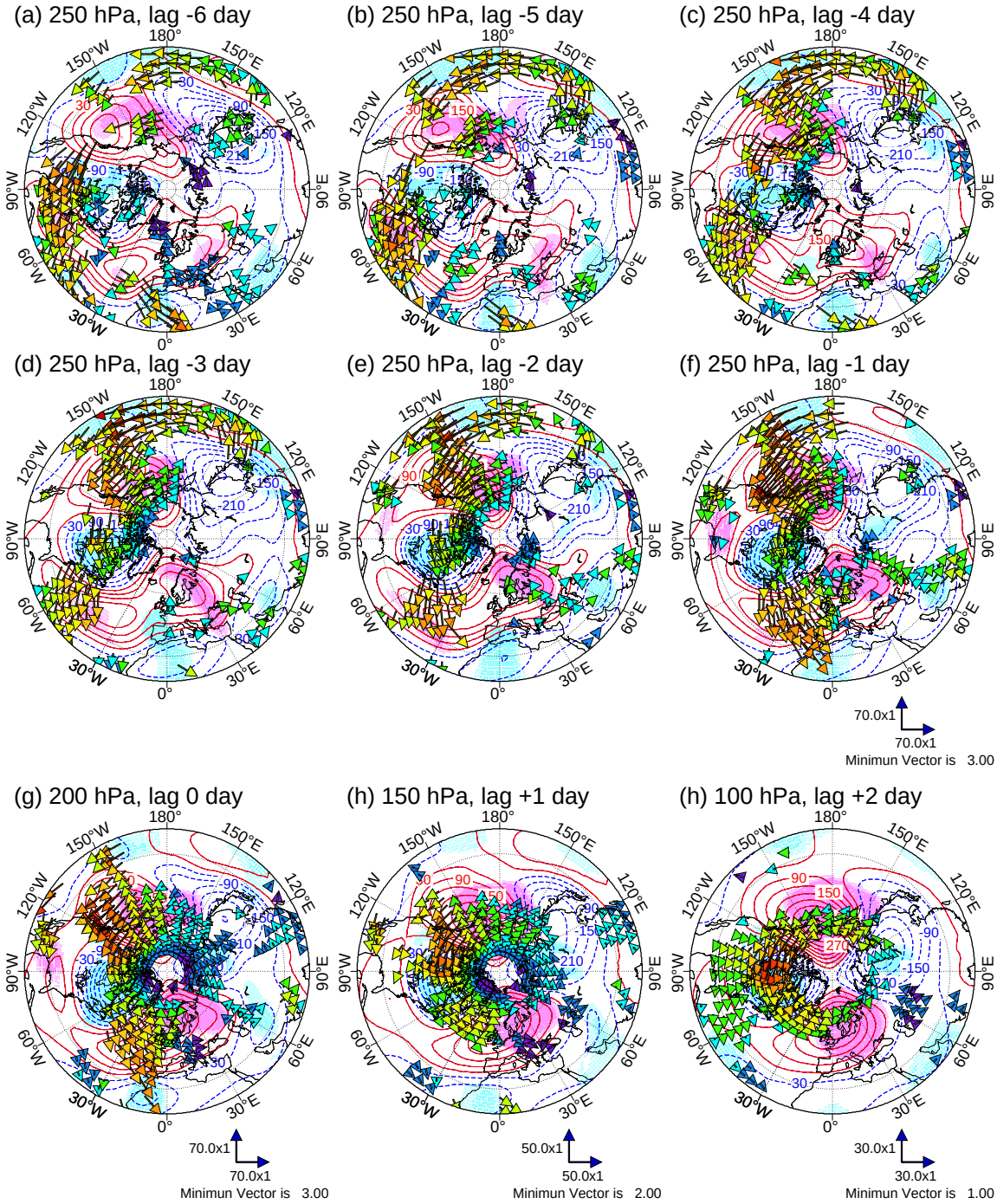

Figure 5-4. As in Figure 5-2 but Plumb's WAF (vectors) and geopotential height deviations from the zonal mean from six days before to two days after the WN2AUT peak during SU_30EPFz. Contour interval is 60 gpm. Only the WAF vectors that are statistically significant above 90% confidence level are plotted. Light and dark Shadings show areas with statistical confidence for geopotential height above 90% and 95%, respectively.

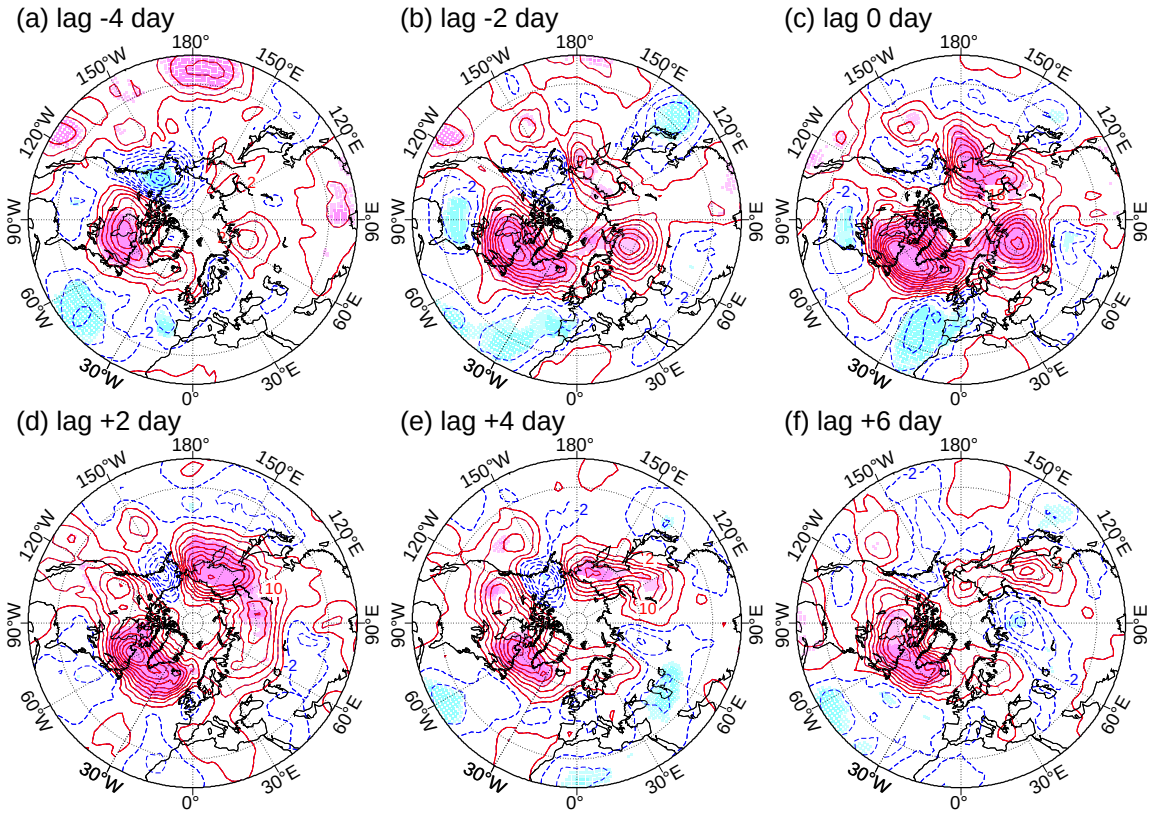

Figure 5-5. As in Figure 5-4 but Plumb's WAFz at 100 hPa from four days before to six days after the WN2AUT peak during SU_30EPFz. Contour interval is 4.0×10^{-2} m^2 s^{-2}. Light and dark Shadings show areas with statistical confidence for Plumb's WAFz above 90% and 95%, respectively.

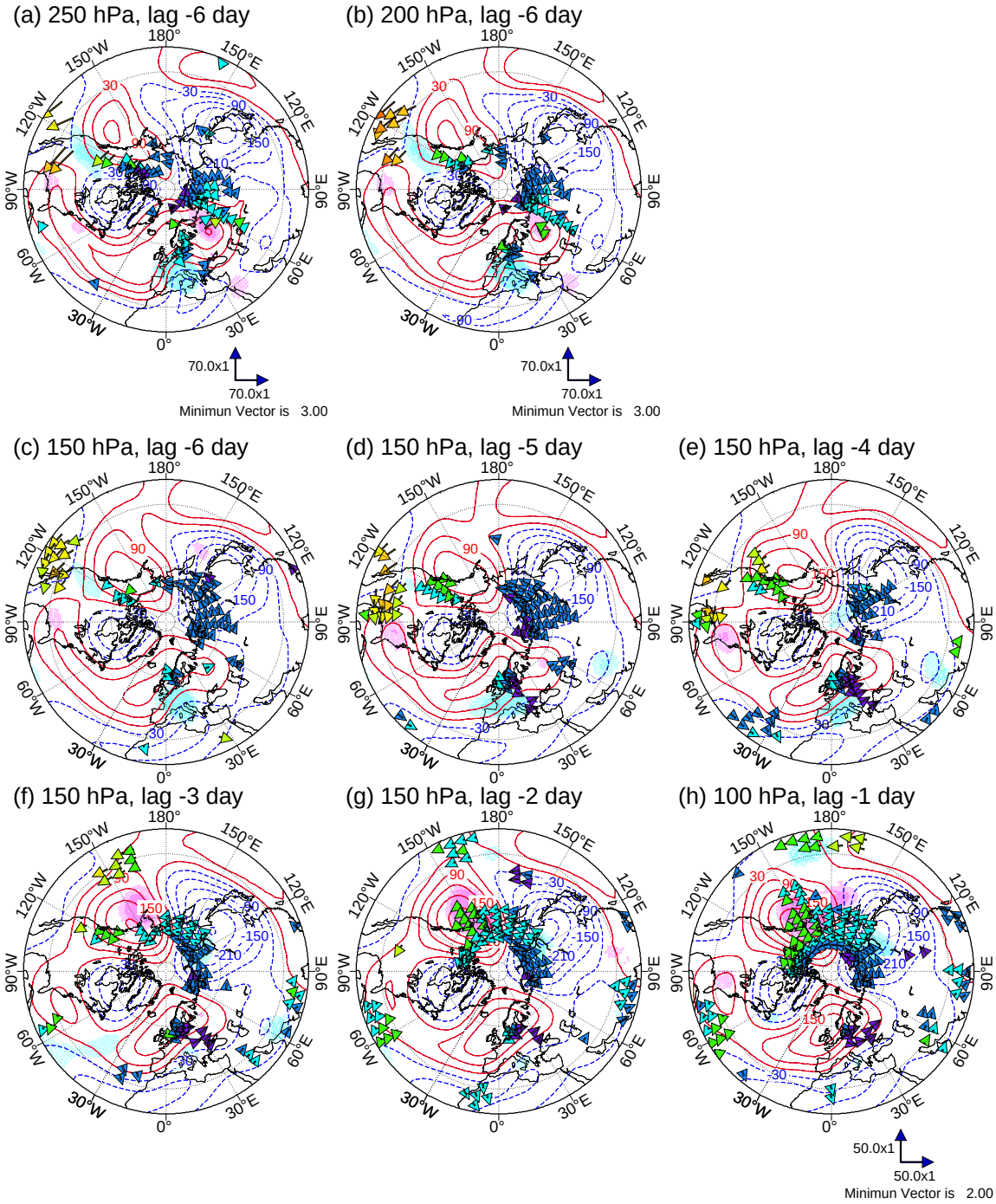

Figure 5-6. As in Figure 5-4 but from six days to one day before the WN2AUT peak during SD_30EPFz.

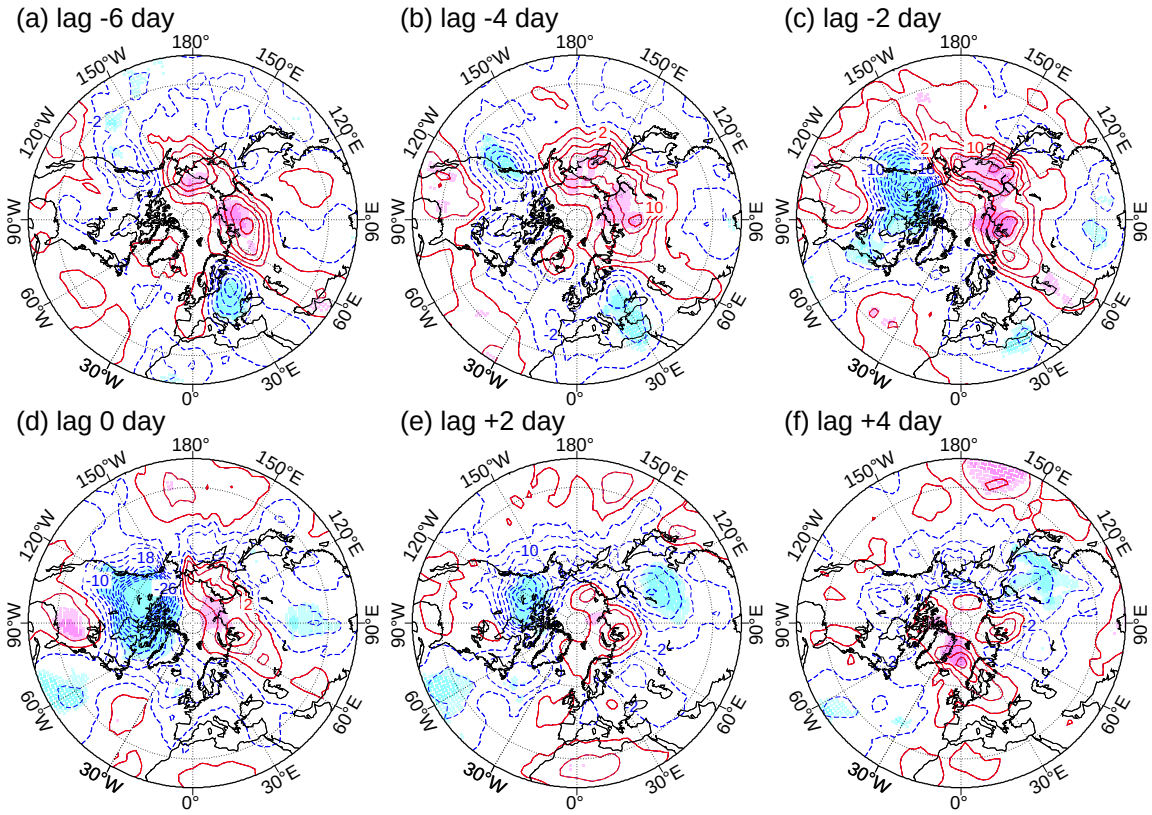

Figure 5-7. As in Figure 5-5 but from six days before to four days after the WN2AUT peak during SD_30EPFz.

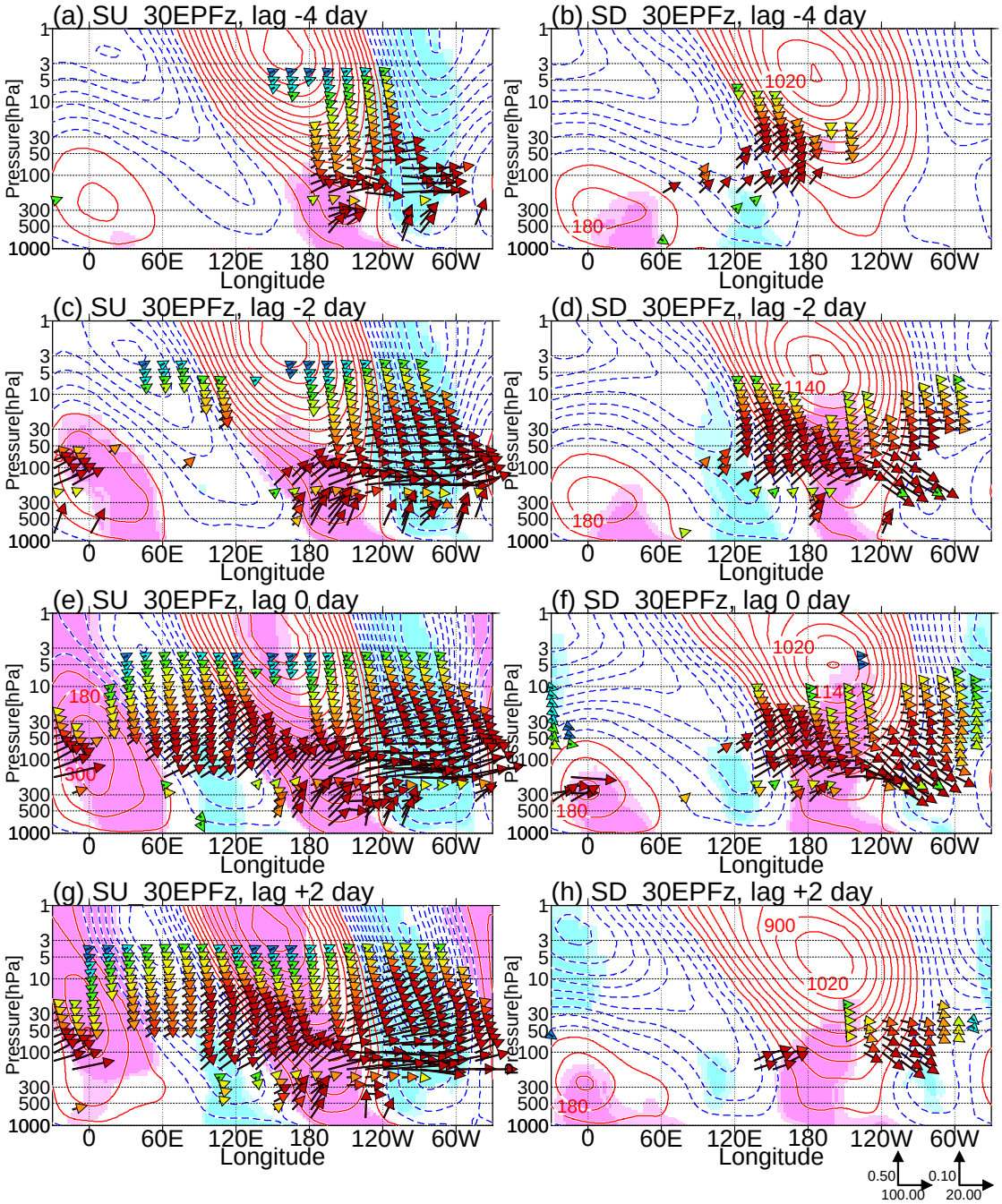

Figure 5-8. Lag composite longitude-pressure cross sections of geopotential height deviations from the zonal-mean (contours) and Plumb's WAF (vectors) averaged over 60°-64°N for successive three-day means from four days before to two days after the WN2AUT peak during SU_30EPFz (left panels) and SD_30EPFz (right panels). The contour interval is 120 gpm. Light and dark Shadings show areas with statistical confidence for geopotential height above 90% and 95%, respectively. The magnitude of Plumb's WAF is in units of $m^2\ s^{-2}$. The vector scales at the lower-right corner of the panels denote vectors below and above 70 hPa, respectively. For example, above 70 hPa, the magnitudes of the vectors are $\sqrt{(WAFx/20.00)^2+(WAFz/0.10)^2}$. Only the WAF vectors that are statistically significant above 90% confidence level are plotted.

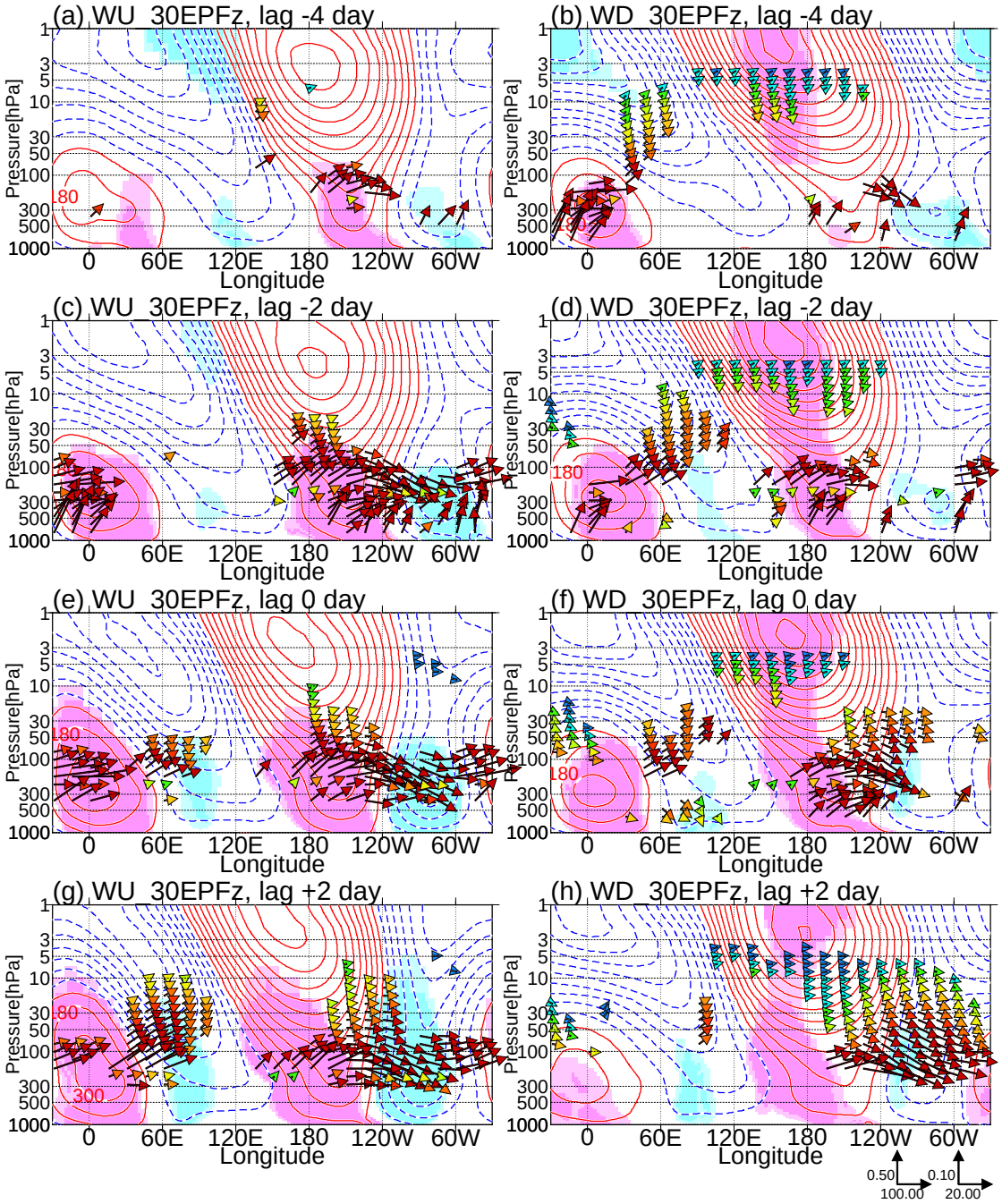

Figure 5-9. As in Figure 5-8 but during WU_30EPFz (left panels) and WD_30EPFz (right panels).

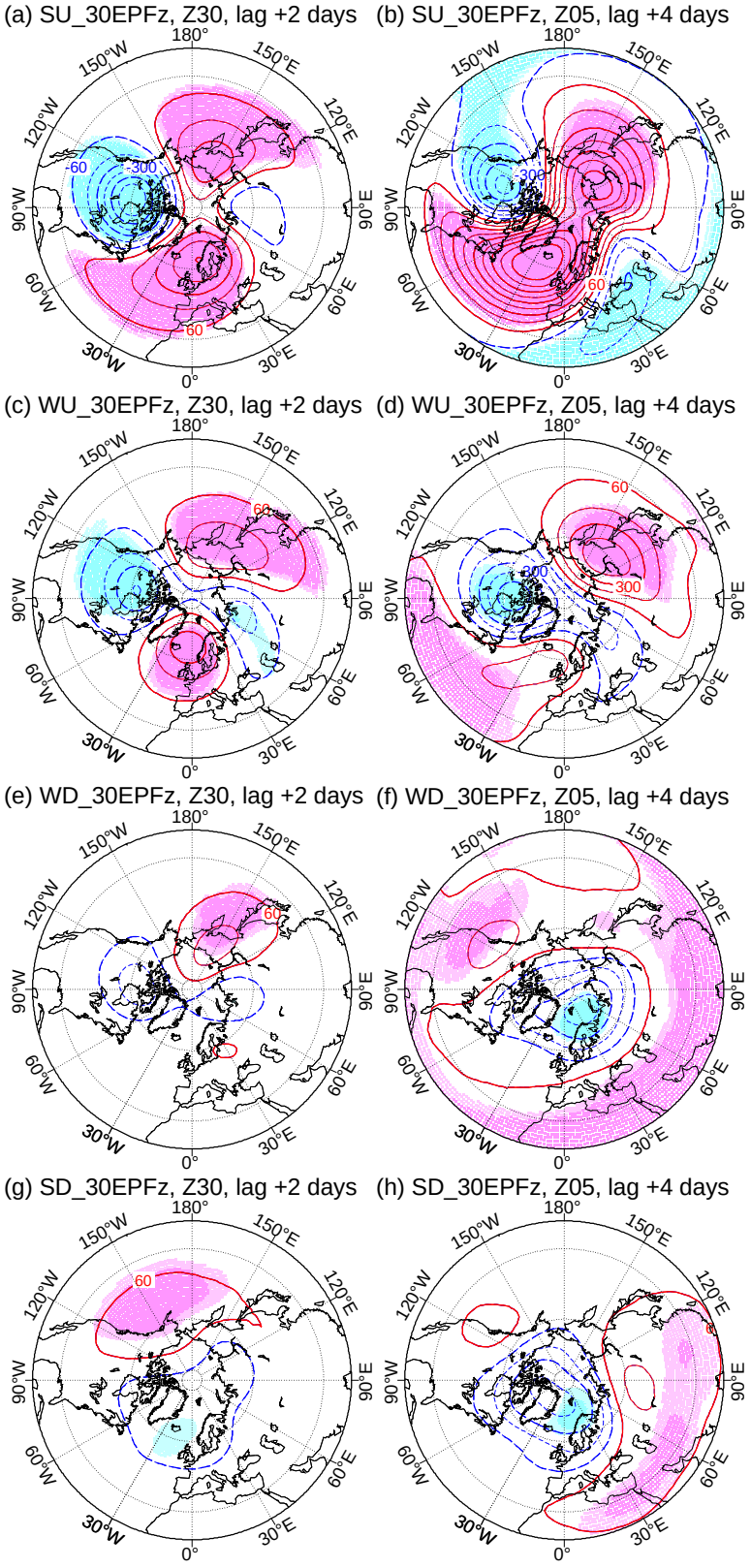

Figure 5-10. As in Figure 5-2 but left and right panels respectively show 30-hPa geopotential height anomalies (contours) two days later and 5-hPa geopotential anomalies (contours) four days later the WN2AUT peak (a),(b) SU_30EPFz, (c),(d) WU_30EPFz, (e),(f) WD_30EPFz and (g),(h) SD_30EPFz. Contour interval is 120 gpm.

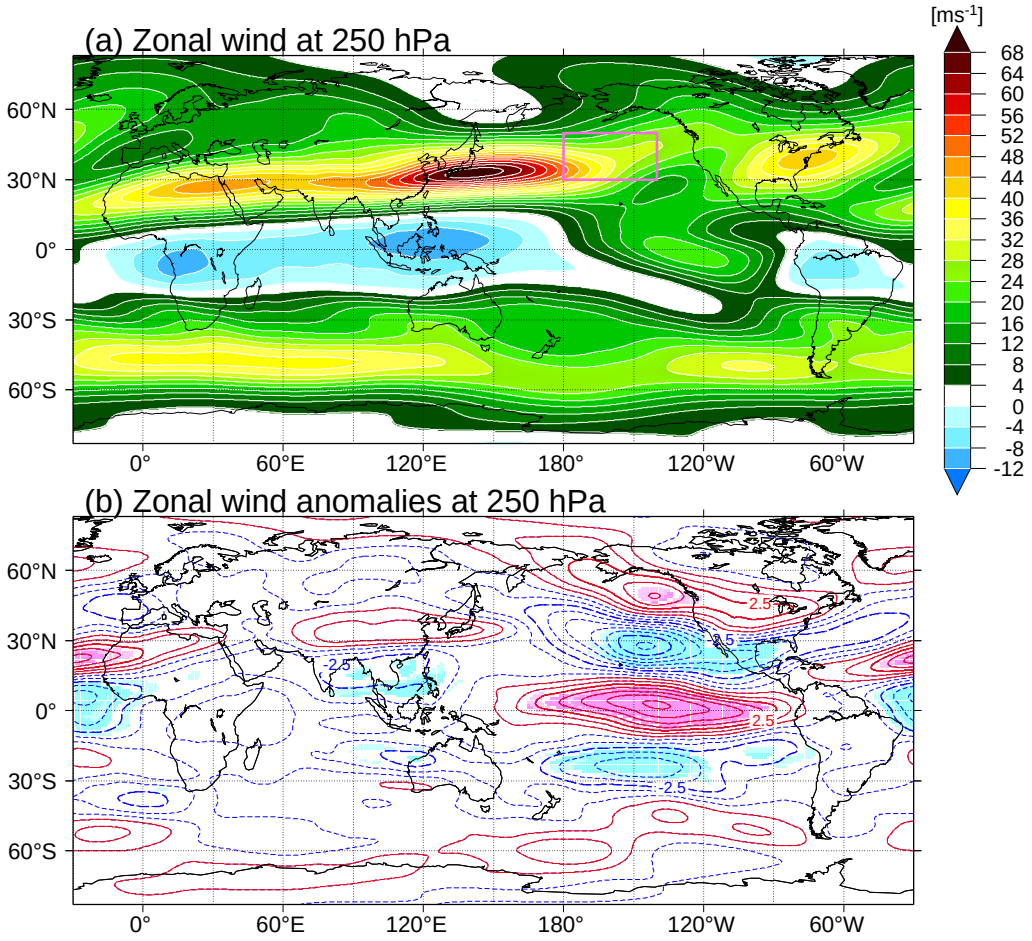

Figure 5-11. Composite maps of 31-day-mean zonal winds (upper panel) at 250 hPa and the anomalies (lower panel, contours) during La Niña winters (NINO.3 =< -0.5). Contour interval is 5 m s^{-1}. Light and dark Shadings show areas with statistical confidence above 90% and 95%, respectively.

(a) NINO.3 >= +0.5 and NINO.3 <= -0.5

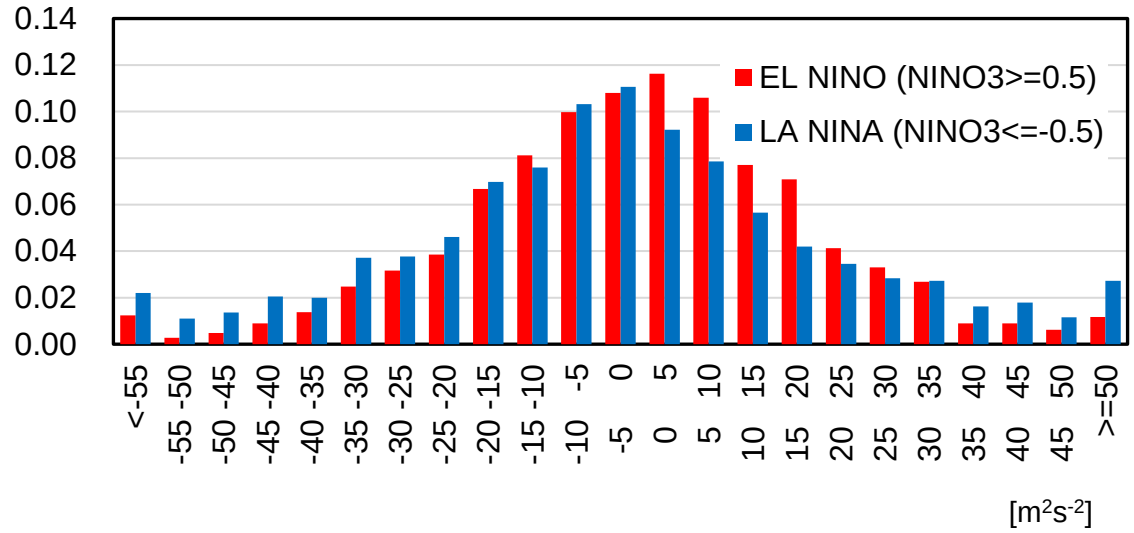

(b) NINO.3 >= +1.0 and NINO.3 <= -1.0

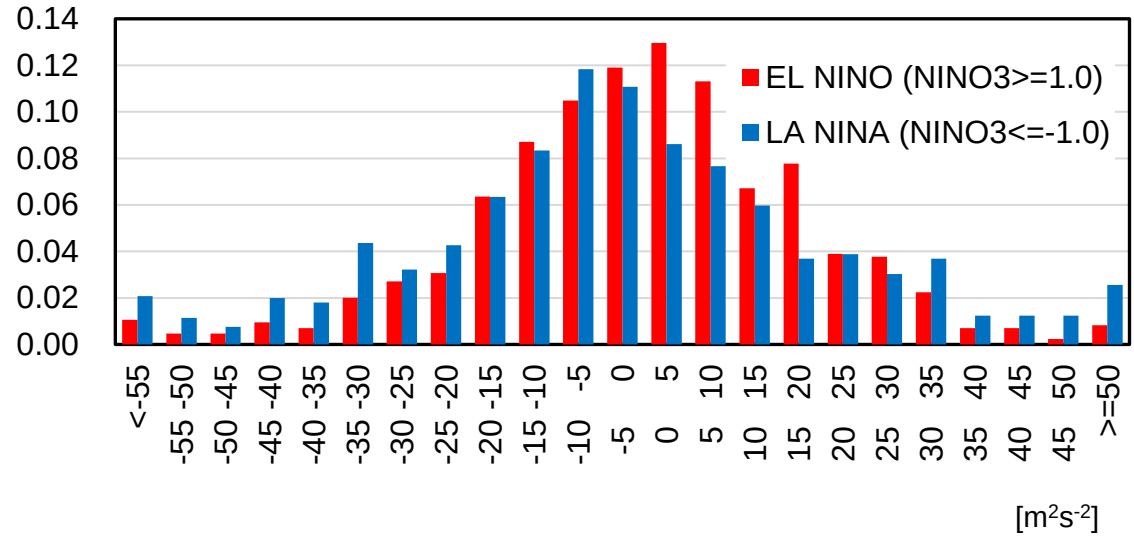

Figure 5-12 Normalized frequency of Plumb's WAFy at 250 hPa averaged over (30–50°N, 140° W–180)

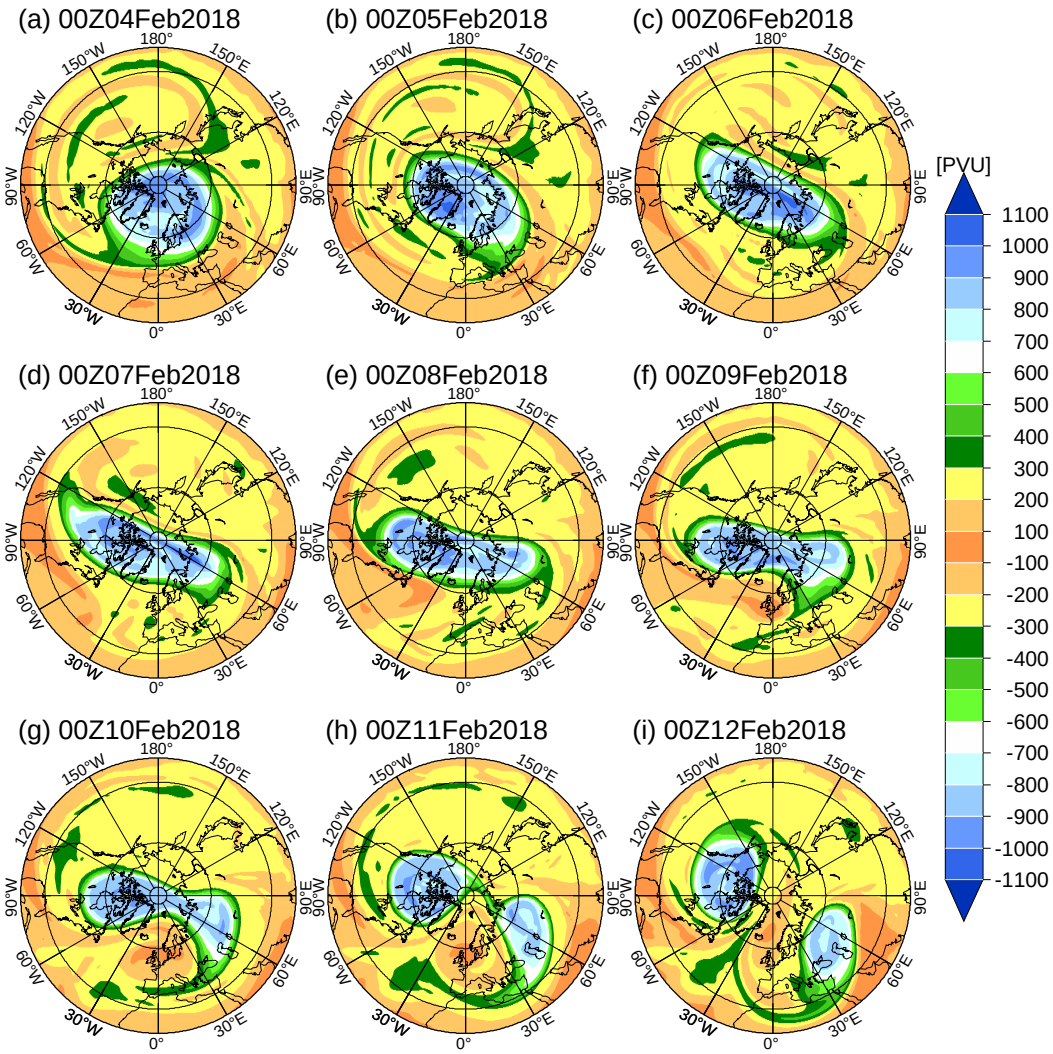

Figure 6-1. Field of isentropic potential vorticity map at 850 K from (a) 00Z 4 February 2018 to (i) 00Z 12 February 2018. Unit: PVU (1PVU = 10^{-6} m^2 s^{-1} K kg^{-1}).

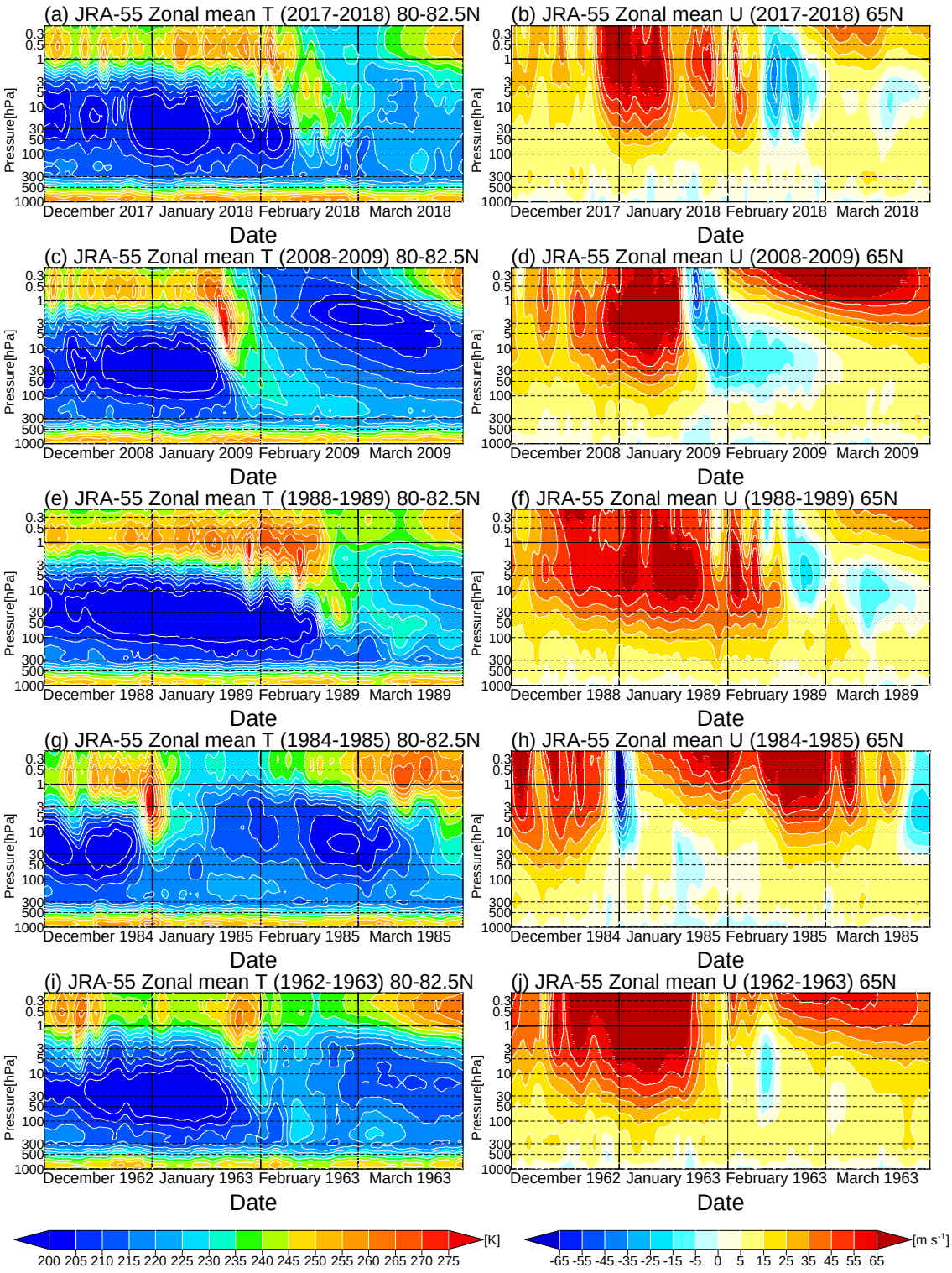

Figure 6-2. Time-pressure cross sections of (left) zonal-mean temperatures averaged over 80°-82.5°N and (right) zonal-mean zonal wind at 65°N during the winters of (a),(b) 2017/2018, (c),(d) 2008/2009, (e),(f) 1988/1989, (g),(h) 1984/1985, and (i),(j) 1962/1963. For the units and shading, see each tone bar.

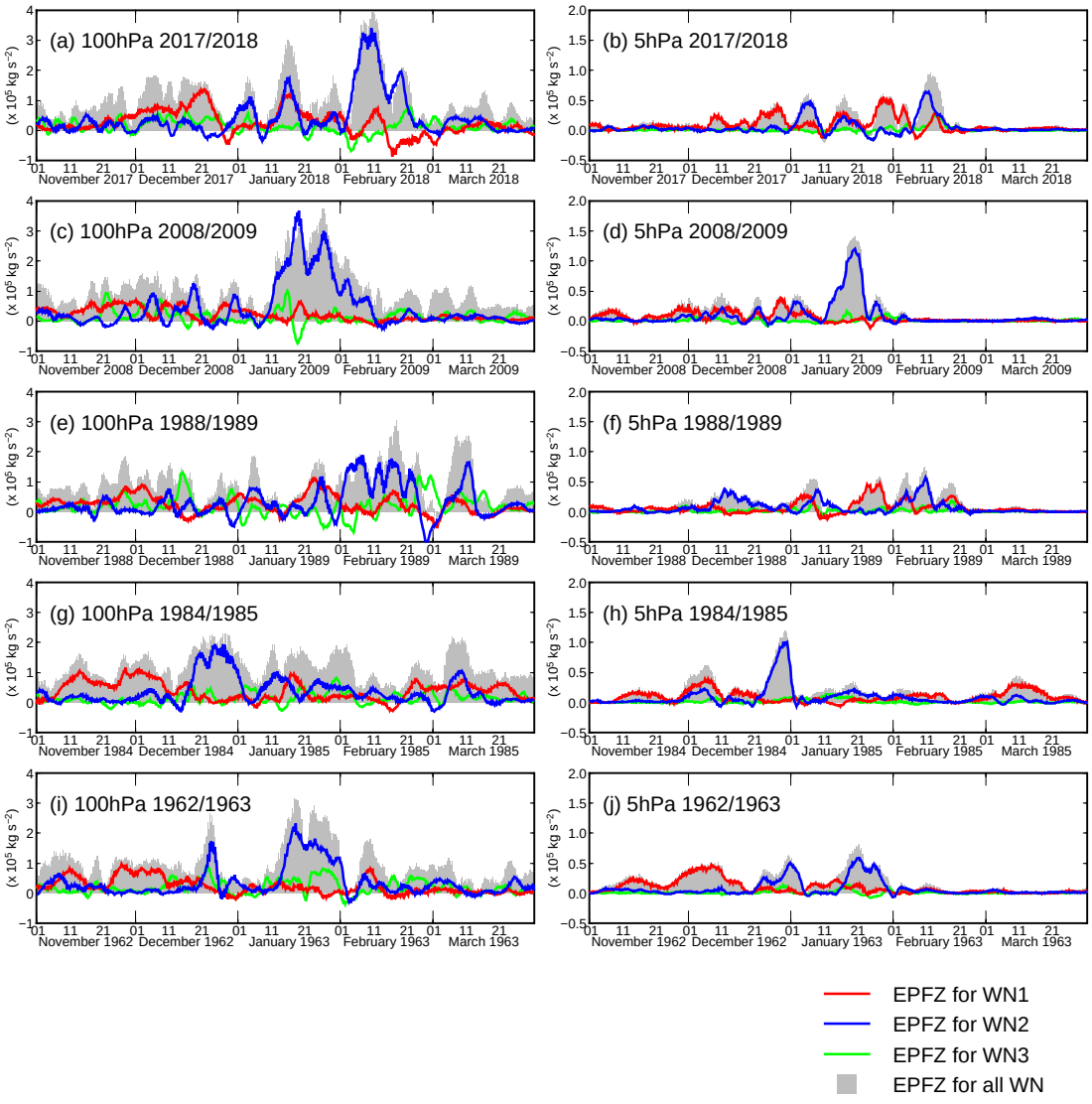

Figure 6−3. Time series of EPFz ($\times 10^5$ s^{-2}) averaged over 30°−90°N at (left) 100 hPa and (right) 5 hPa in the winters of (a),(b) 2017/2018, (c),(d) 2008/2009, (e),(f) 1988/1989, (g),(h) 1984/1985, and (i),(j) 1962/1963. EPFz of waves 1, 2, and 3 are denoted by red, blue, and light green lines, respectively. Gray shading represents the EPFz of all wavenumbers.

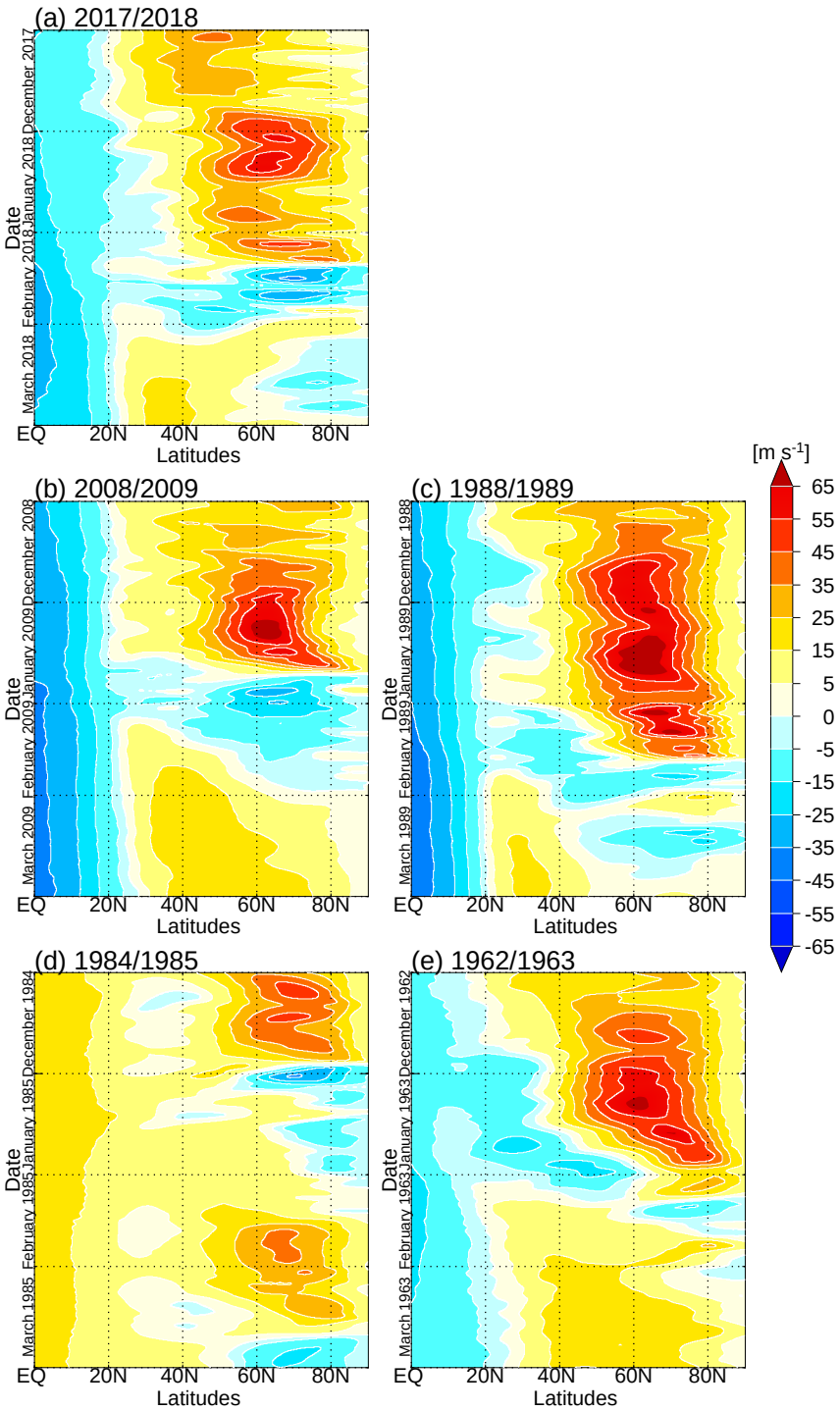

Figure 6-4. Latitude-time cross sections of zonal-mean zonal wind (m s^{-1}) at the 10-hPa pressure level for the winters of (a) 2017/2018, (b) 2008/2009, (c) 1988/1989, (d) 1984/1985, and (e) 1962/1963.

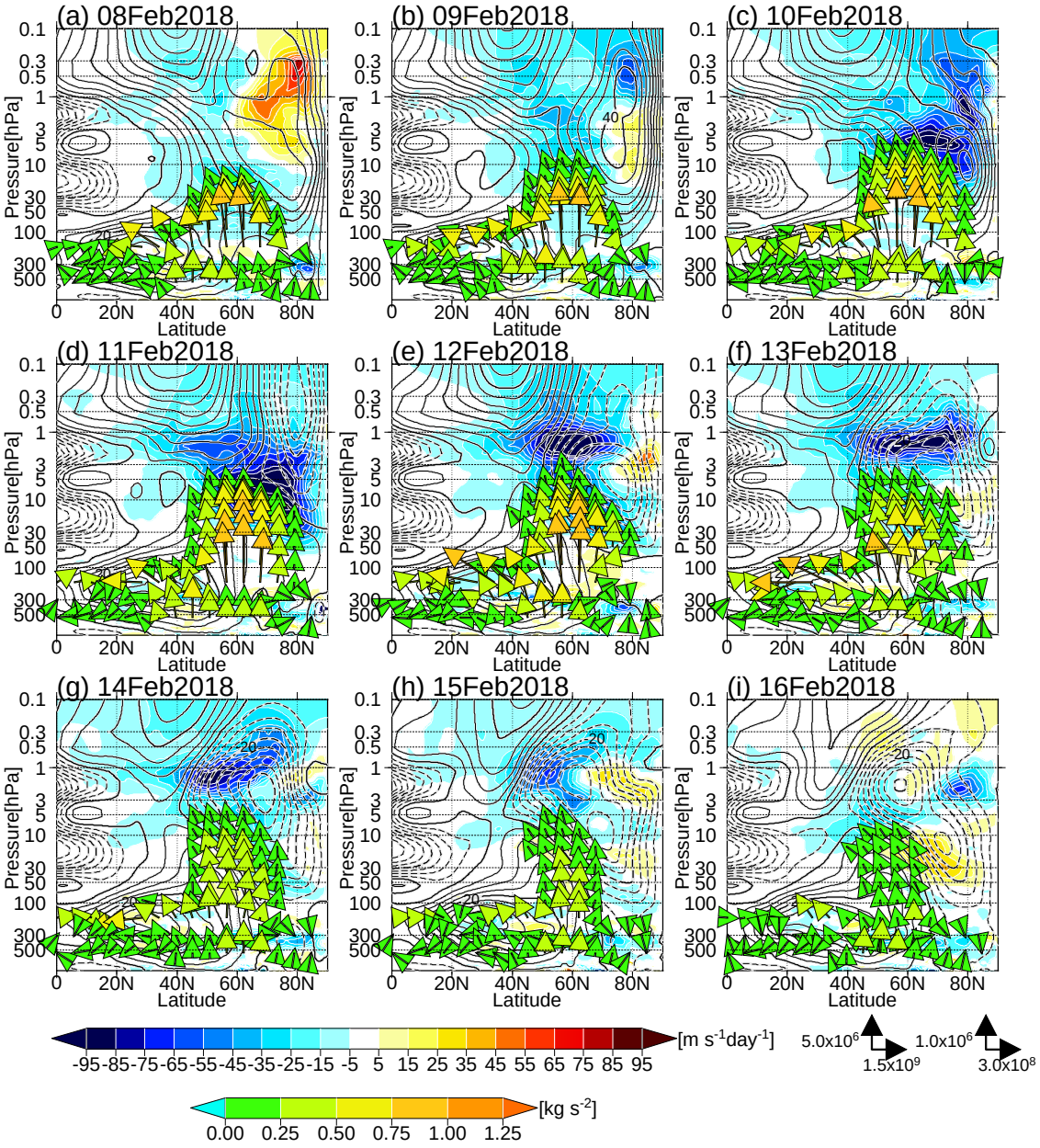

Figure 6-5. Meridional cross section of zonal mean zonal wind (contours), EP fluxes (vectors), and EP flux divergence (shadings) for daily means during 8-16 February 2018. The contour interval is 5 m s^{-1}, the EP flux vectors are in units of kg s^{-2} , and the vector scales at the lower-right corner of the panels denote vectors below and above 100 hPa. The color scale for the vectors (lower tone bar) corresponds to the magnitude of the EP flux in the figure space. For example, above 100 hPa, the magnitudes of the vectors are $\sqrt{(EPFy/3.0\times10^{8})^2+(EPFz/1.0\times10^{6})^2}$.

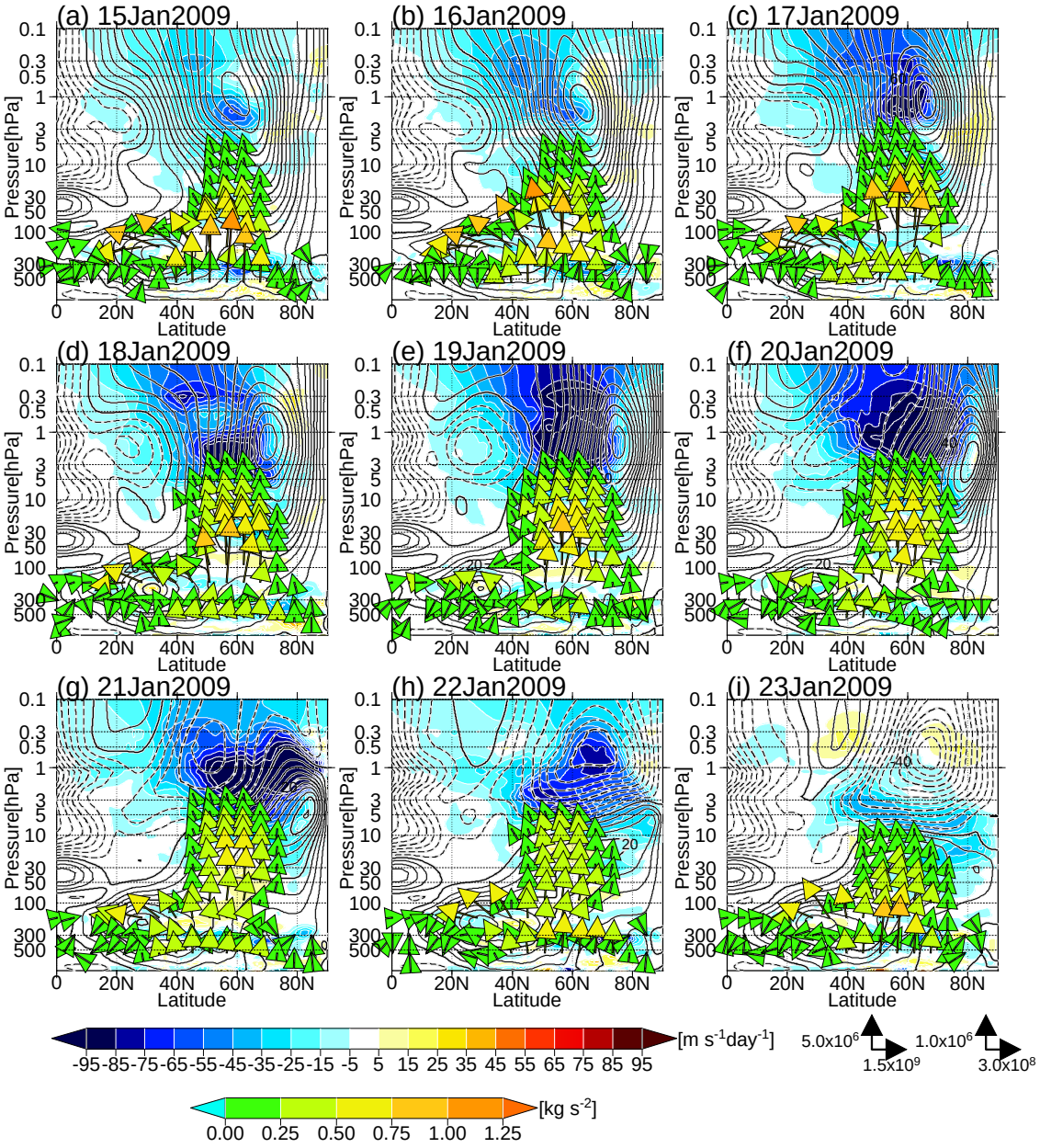

Figure 6-6. As in Figure 6-5 but for 15-23 January 2009.

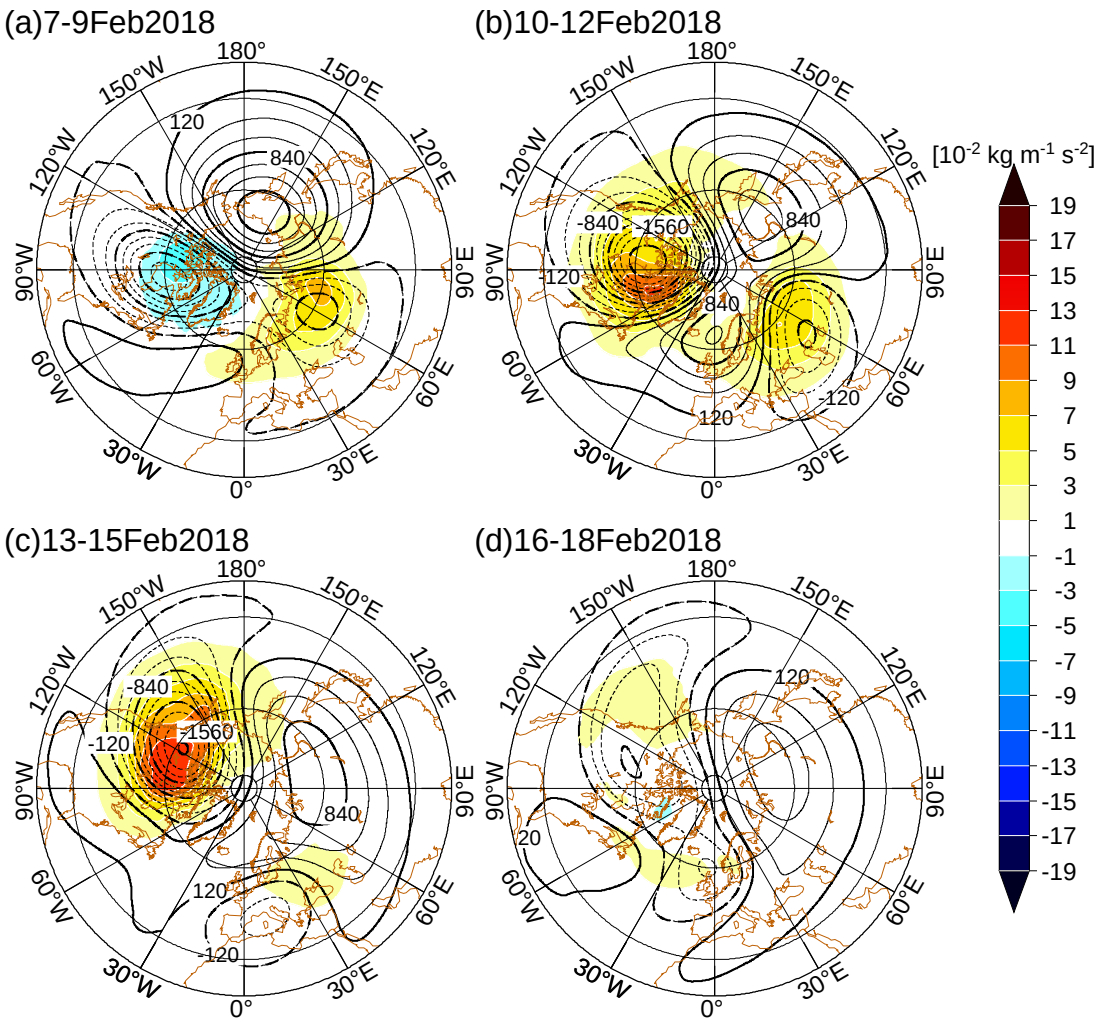

Figure 6-7. Horizontal distributions of vertical 3D-flux-W components (3D-flux-Wz, shadings) and geopotential height deviations from the zonal averages (contours) averaged over successive three days at 5 hPa for the period from early to mid-February 2018. For shadings, see the tone bar. The contour interval is 240 gpm. The dates are (a) 7-9, (b) 10-12, (c) 13-15, and (d) 16-18 February 2018.

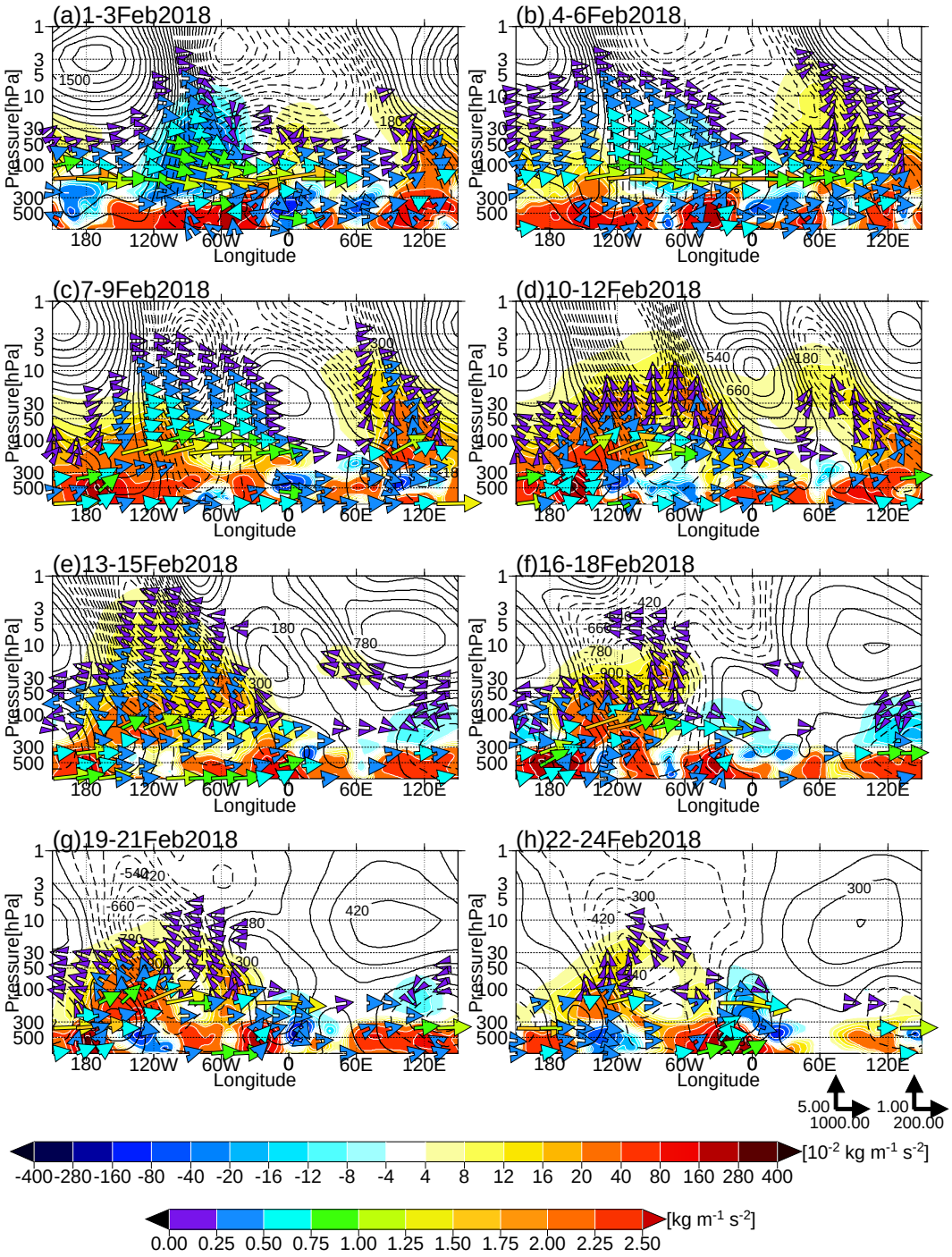

Figure 6-8. Longitude-height cross sections of geopotential height deviations from the zonal-mean (contours), 3D-Flux-Wz (shading) and 3D-Flux-W (vectors) averaged over 45°-75°N for successive three-day means. The contour interval is 120 gpm. The magnitude of 3D-Flux-W is in units of kg m^{-1} s^{-2}. For the shading, see the tone bar (the second one from the right). The vector scales at the lower-right corner of the panels denote vectors below and above 70 hPa, respectively. The color scale for the vector (lower tone bar) corresponds to the magnitude of 3D-Flux-W in the figure space. For example, above 70 hPa, the magnitudes of the vectors are $\sqrt{(\text{3D-Flux-Wx}/200.00)^2+(\text{3D-Flux-Wz}/1.0)^2}$. The dates are (a) 1-3, (b) 4-6, (c) 7-9, (d) 10-12, (e) 13-15, (f) 16-18, (g) 19-21, and (h) 22-24 February 2018.

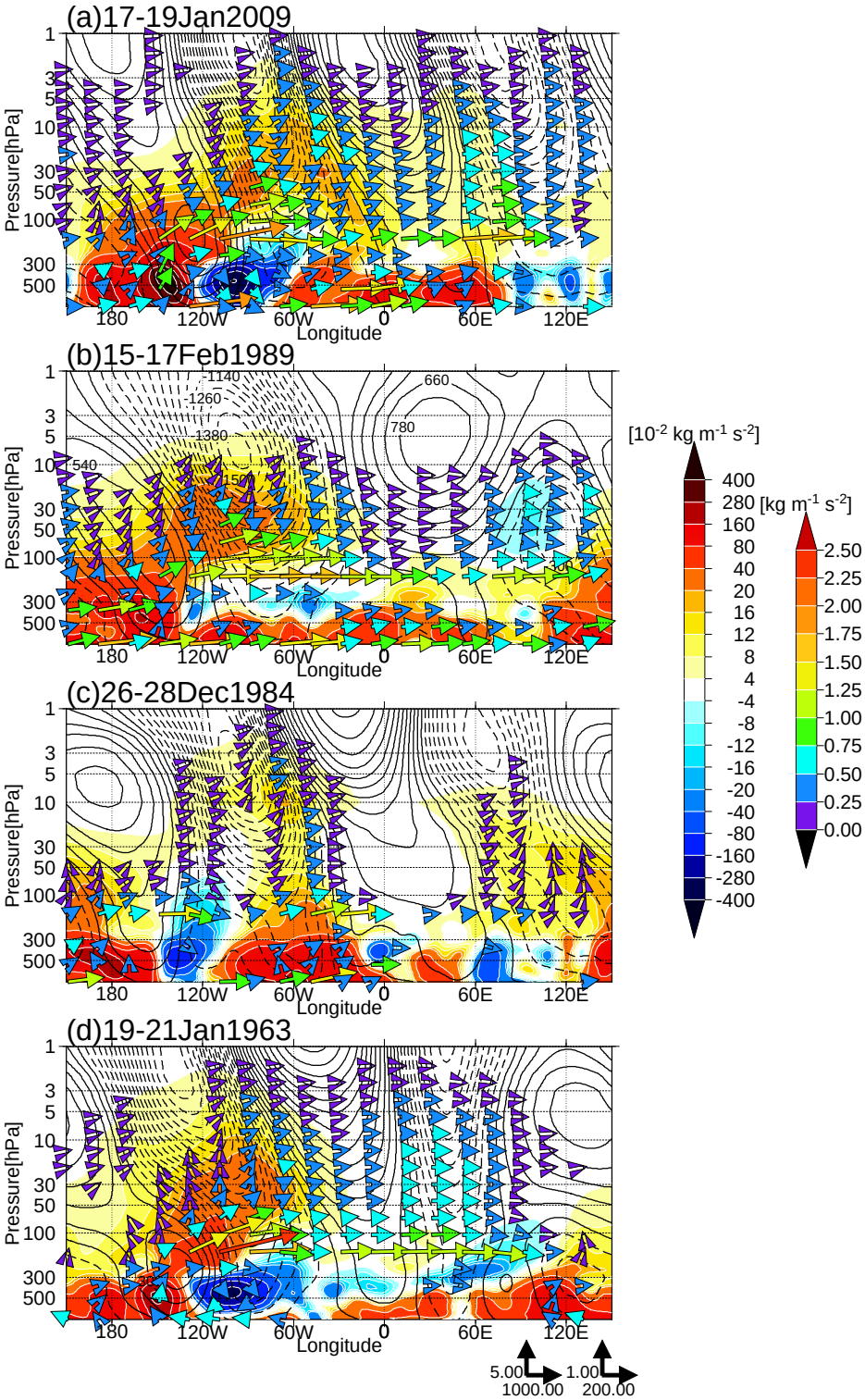

Figure 6-9. As in Figure 6-8 but for (a) 17-19 January 2009; (b) 15-17 February 1989; (c) 26-28 December 1984; (d) 19-21 January 1963.

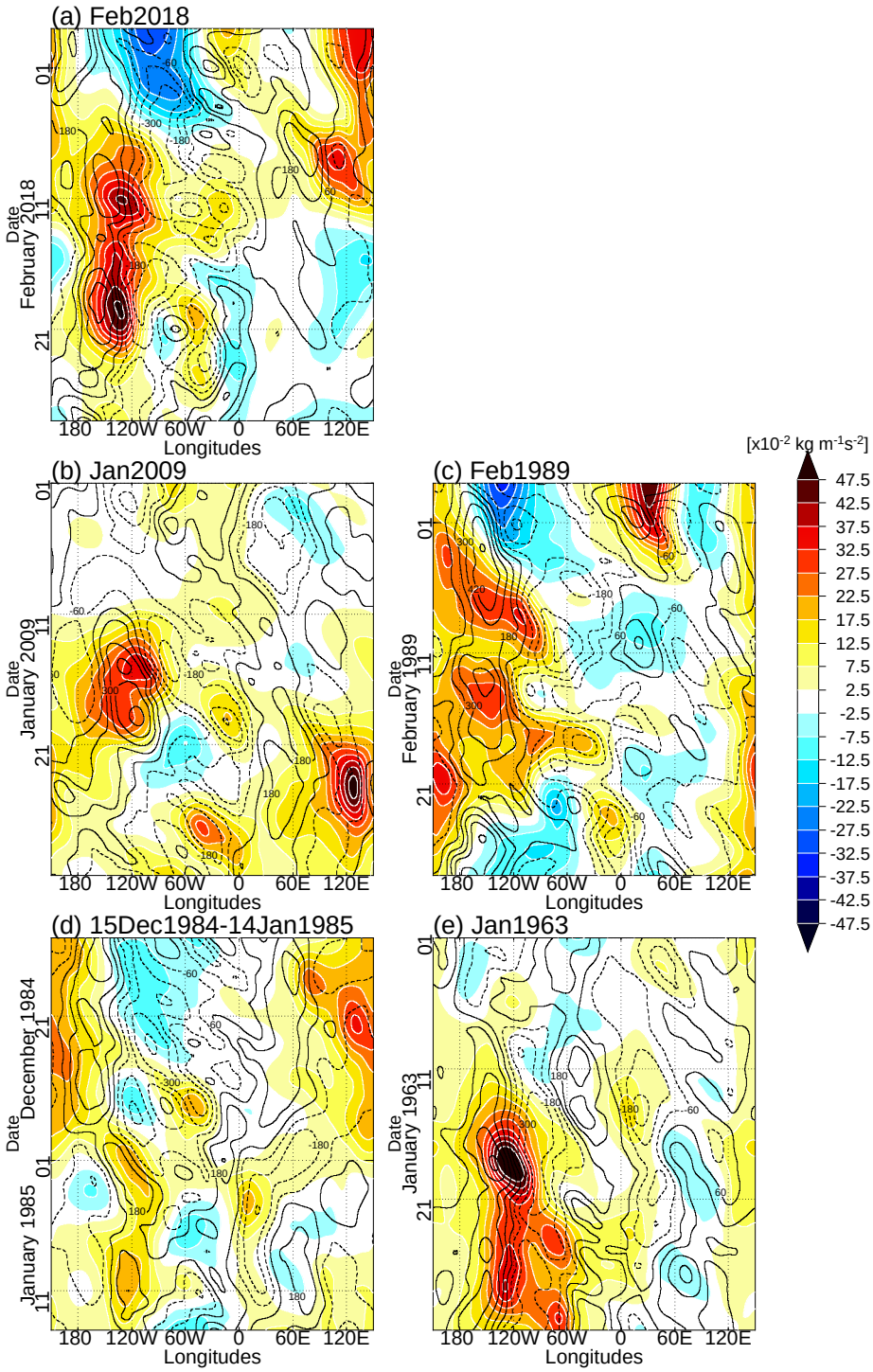

Figure 6-10. Longitude-time cross sections of 250-hPa geopotential height deviations from the climatological mean (contours) and 100-hPa 3D-Flux-Wz (shading) averaged over 45°-75°N during (a) February 2018, (b) January 2009, (c) February 1989, (d) from 15 December 1984 to 14 January 1985, and (e) January 1963. For the shading, see the tone bar.

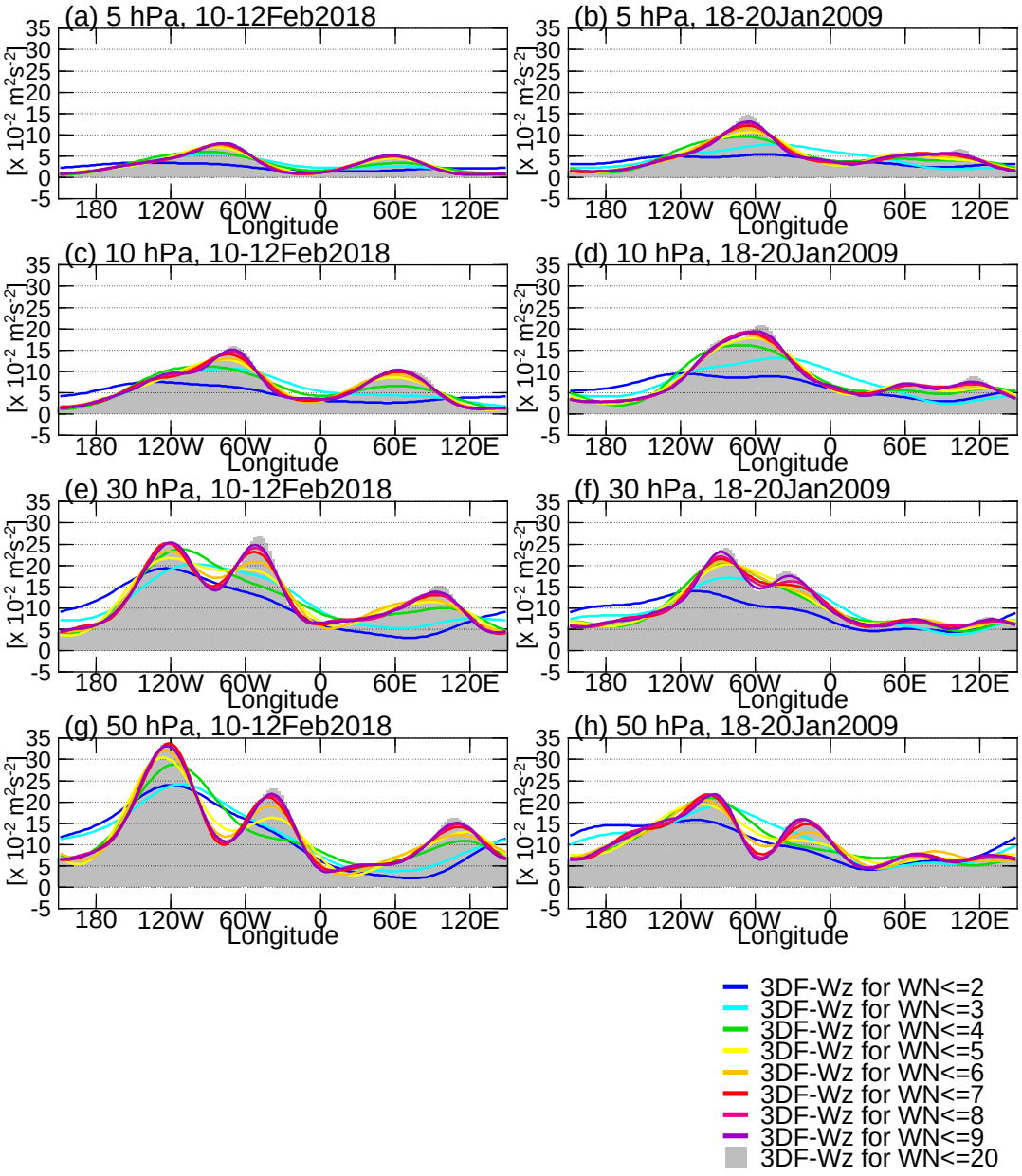

Figure 6-11. Longitudinal distributions of 3D-flux-Wz averaged over 45°-75°N for various zonal wavenumber ranges at (a),(b) 5 hPa, (c),(d) 10 hPa, (e),(f) 30 hPa, and (g),(h) 50 hPa. These are calculated from the three-day field for (left) 10-12 February 2018 and (right) 18-20 January 2009. Shadings represent 3D-flux-Wz for zonal wavenumbers of 20 or less.

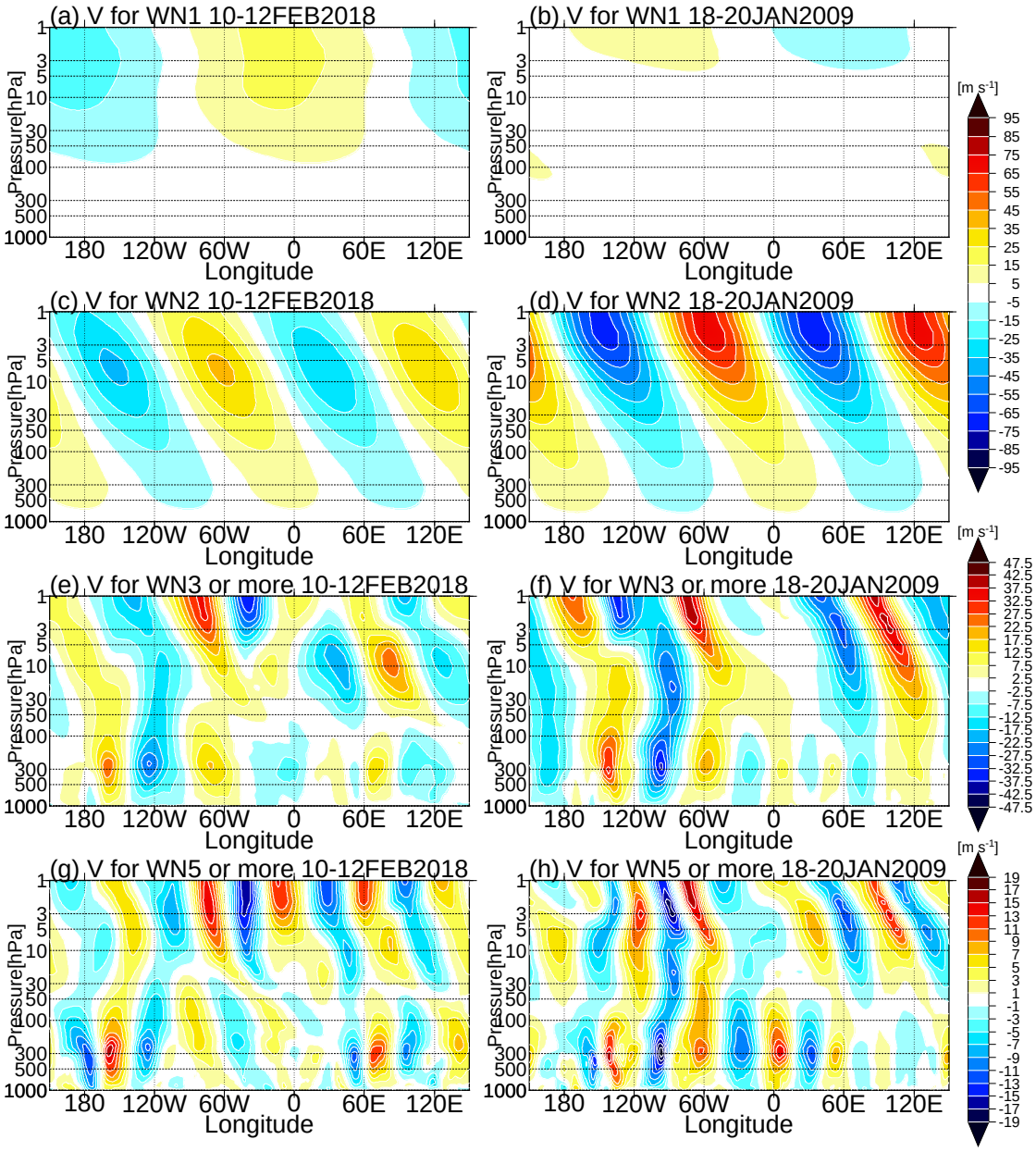

Figure 6-12. Longitude-height cross sections of Lanczos filtered meridional wind (m s^{-1}) for (a),(b) zonal wavenumber one, (c),(d) zonal wavenumber two, (e),(f) zonal wavenumber three or more, and (g),(h) zonal wavenumber five or more averaged over 45°-75°N during (left) 10-12 February 2018 and (right) 18-20 January 2009.